DESIGN AND DEVELOPMENT OF AN OMNI-DIRECTIONAL ROVER FOR EXPLORATION ON UNDULATING TERRAIN LOH WUH KEN 2005

DESIGN AND DEVELOPMENT OF AN OMNI-DIRECTIONAL ROVER FOR EXPLORATION ON UNDULATING TERRAIN

LOH WUH KEN

SCHOOL OF MECHANICAL & AEROSPACE ENGINEERING

NANYANG TECHNOLOGICAL UNIVERSITY

2005

Design and Development of An Omni-Directional Rover for Exploration on Undulating Terrain

Loh Wuh Ken

School of Mechanical & Aerospace Engineering

A thesis submitted to the Nanyang Technological University
in fulfillment of the requirement for the degree of
Master of Engineering

2005

ABSTRACT

This report describes the development of a new 6-wheel Omni-Directional Rover (ODR). The primary objective of the work was to develop locomotion and wheel mechanism for a rover that can navigate smoothly and omni-directionally on undulating terrain. With that, the robots have made their way into applications like farming, waste clean-up and exploration. All mobile robots use locomotion that generates traction, negotiates terrain and carries payload. Well-designed rover locomotion also stabilizes a robot's body, smoothes the motion of chassis, and accommodates the deployment and manipulation of work tools. Many rovers with robust locomotion design have been developed. However, rover locomotion design with omni-directional mobility has not been addressed extensively.

The *analytical analysis* and P_{max} test are used to determine the front fork configuration. The 2D simulation software, *Interactive Physics 2000*, is used to obtain the optimal configuration of locomotion. After that, the 3D model is setup to study the dynamic behaviors of the ODR. The 3D simulation software, *MSC. visualNastran 2003*, is used to captures the quantitative relationships among configuration parameters (e.g. wheel diameter, chassis articulation location), performance parameter (e.g. speed) and task parameter, (e.g. size of obstacles). Then, the ODR will be integrated with the motion controller. Two modes, PC mode and tele-operated mode, are developed. Therefore, with the development of the user interface software, the user can command this ODR move omni-directionally and illustrating the implementation and evaluation of the locomotion results put forth by this report.

Several recommendations for further research to enhance the performance of the ODR are suggested.

ACKNOWLEDGEMENTS

The project owes much to many people around me. I would like to take this opportunity to express my gratitude to my project supervisor, Associate Professor Low Kin Huat for exposing me to the wonderful world of mobile robotics. I also like to thanks him for his guidance and advice throughout this project. His words of encouragement and support are also greatly appreciated.

I would like to thank all the laboratory technicians in the Robotics Research Centre, Nayang Technological University for their kind assistance with the use of equipment and facilities. They are Mr. Lim Eng Cheng, Ms. Agnes Tan, Mr. You Kim San and Ms. Toh Yen Mei.

Mr. Ang Siau Eng, and Mr Ng Chin Chew, final year students, needed to be thanked for their hard work in testing the redesigned omni-directional wheel and data collection for 3D simulation.

I would like to express my appreciation to my colleagues Mr. Tee Tzey Wee, and Mr. Wang Heng for helping me conducting the experiments. In addition, special thanks are due to my mentor Mr. Leow Yong Peng, for his ideas, constant assistance, support, positive encouragement and experience shared throughout the present work.

Contents

List of Figures

List of Tables

Chapter 1

Introduction

In recent years, the development and research on mobile robots has become extremely active. For example, the 11th version of Honda's research, a developed humanoid robot *ASIMO* shown in Fig. 1.1 (a), was designed to walk with natural gait. It used Honda's i-walk technology to move smoothly, turning corners without pausing, and navigating stairs without a hitch. Other than the humanoid, the robot pets are developed and available in store world wide, as shown in Figs. 1.1 (b) and (c). The famous example is Sony's *AIBO*, an autonomous pet robot. It learns words, adapts itself to its environment, and develops a personality that's based on his interaction with humans. Another one is *Necoro*, developed by Omron, is an autonomous cat, who purrs and plays. The changes is due to the advancement of computer, actuator, battery and sensor technologies, which reduced the time and cost needed to build a robot significantly.

Within the mobile robot research and development environment, there are five categories of study fields, namely, locomotion, sensing, reasoning, communication, and manipulation [4].

- Locomotion means how the robot moves through its environment;
- Sensing deals with how robot measures its own parameters as well as its environment;

(a) (b) (c)

Figure 1.1: Examples of mobile robots. (a) Honda's ASIMO [1]; (b) Sony's AIBO [2]; (c) Omron's Necoro [3].

- Reasoning shows how the robot map the sensing measurements into actions;
- Communication focuses on how robot communicates with internal subsystems and with the external interfaces;
- Manipulation addresses the tasks of moving objects by various possible ways; it involved grasping, carrying, pushing, throwing and so on.

The scope of the present work will focus mainly on the locomotion studies where theories will be tested and verified by means of simulation and field tests.

1.1 Motivation

In general, robots have often been used built to support human activities in areas that human are not competent in. For instance, it can be used to move a heavy load to a desired destination. Robots could also be designed to navigate in environment hazardous or dangerous to human or on some terrains that cannot be reached by human. For example, a pyramid rover [5], designed by iRobot, as shown in Fig. 1.2 (a), was employed by National Geographic to solve a mystery that lies deep in the bowels of the 4,500-year-old Great Pyramid of

Giza. Mars Exploration Rover [6] shown in Fig. 1.2 (b), is developed to search for and characterize a wide range of rocks and soils that hold clues to past water activity on Mars. In almost all of these cases, an important feature that a robot must possess is *mobility*.

(a) (b)

Figure 1.2: Examples of mobile robots. (a) IRobot's pyramid rover [5]; (b)Nasa's Mars exploration rover [6].

Incorporating mobility into robots has always been the main focus of study when the robots started to invade the daily life of human beings. The most common forms of land locomotion are legged, wheeled, and tracked. Among the three systems, the wheeled locomotion is the most popular means for providing robot with mobility on flat terrain. It has been seen as a simple and foolproof choice although there may be no animals on the earth use wheels to move around. Legged locomotion generally have the best adaptive toward rough terrain while wheeled locomotion are more suitable for smooth terrain as they move faster on flat surface. However, legged robots are much difficult to control and design due to its' multiple degrees of freedom configuration and control problems, which will be further discussed in Section 1.2. Having almost the same capability as legged robot on terrain adaptability, tracked robot is less favorable than the previous two due to its poor efficiency. In conclusion, among the three systems, the wheeled locomotion has higher potential to see

wide applications due to it's simple in design, easy to fabricate, energy efficient, and offers a higher load carrying capability.

The robot needs sufficient mobility to traverse areas of interest, which has a better potential than other types of robots in replacing, or helping human beings in the manufacturing, service, and entertainment industries. It means the mobile robot must be able to navigate bumpy terrain, slopes, and ultimately be able to climb steps. However, almost all previous Wheeled Mobile Robots (WMRs), either holonomic or non-holonomic, are designed to move only on flat, even terrains due to its' low surmountable height constraint. Therefore, more research is needed to provide industry with a better platform for a great variety of applications.

In this project, the author aims to design a WMR with omni-directional mobility and rover-like climbing ability, also maintains good efficiency, operability and controllability as good as conventional WMRs. The constructed robot is expected to pass through the narrow road, avoid the obstacles, and climb up the steps between the roadway and sidewalk. The ability to climb staircase is less crucial because elevator is widely available in Singapore. However, the function to travel over the multiple-step is still very useful to extend the working range of the robot.

The focuses of this thesis are the kinematic and dynamic modeling of the robot, design and analysis of *Omni-Directional Rover* (ODRs) for application on undulating terrain. It also covers the transmission design, power management, motion control, and electromechanical integration. Upon completion of the ODR, it has to be able to navigate safely and smoothly on uneven terrain, move in omni-directions, and demonstrate it on few selected paths. The following sections shall discuss various types of rover locomotion and additional attributes to further enhance the mobility of the robotic locomotion.

1.2 Literature Survey

Producing mobile robots starts with the first building block - locomotion, since it provides mobility. Various types of mobile robot configurations have been proposed and studied to improve the motion capabilities of mobile robots[7, 8]. However, most of such robots are equipped with complicated mechanism due to the large inclination in usual step. This may hinder the running performance on the even terrain. In addition, with only information on how mobile robots create motions is insufficient. A concurrent understanding on the impacts of the terrain on robot motions is equally important. The typical failures a mobile robot can encounter due to terrain are,

- Clearance failures occur when some part of the robot chassis hits the ground.
- Vibration due to the irregularities of the terrain profile can cause damage to the equipment, and wear the robot itself.
- Stability failure where too steep slopes or too high speed over rough terrain, which can make the robot tip over.
- Traction failure caused by loss of friction or sinkage.

In order to avoid failure, some system analysis is needed to define its mission, capabilities, such as speed and stability, and the operating environment also included. The different alternatives should then be considered, as different types of locomotion systems have different characteristics, complexity, and cost. The objective of this survey is to look for optimum locomotion which provides maximum step climbing ability with high mobility on smooth terrain.

Among all proposals, legged robots are definitely one of the best adaptive locomotion to deal with this problem. However, its major drawback is inefficiency on flat ground due to sophisticated design. For example, the *insect-like*

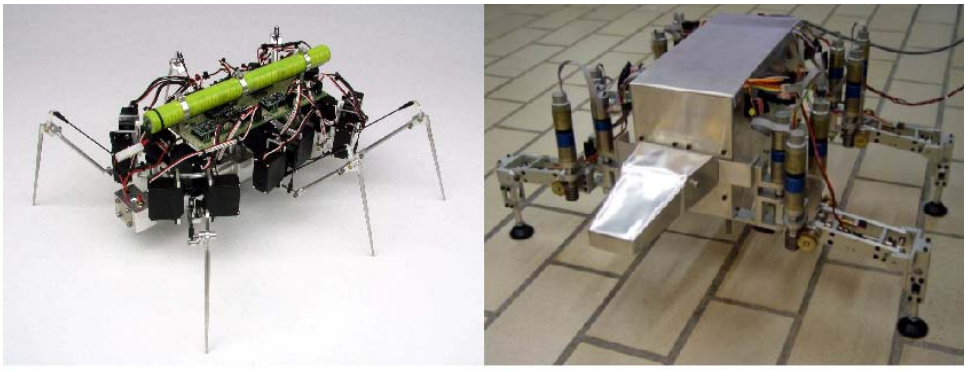

Figure 1.3: Examples of legged robots. (a) Omni-bot [9]; (b) Quadruped robot [10].

[9] or *reptile-like* [10] locomotion as shown in Fig. 1.3, which has multiple degrees of freedom configuration with adaptable walking gait to move on rough terrain.

Also, the other major problems for the locomotion are to integrate complicated sensors to "see" ahead and to coordinate foot placement on undulating terrain. To achieve "walking without falling, both robots adopt different gait patterns. *Insect-like* robot offers a static balance that ensures that the robot will not fall over easily. At any instance, a minimum of three legs must touch the ground, forming the stable tripod. The *reptile-like* robot, either moves one leg at a time, or employs some kind of dynamic balance when two of its legs are on the ground at any instance.

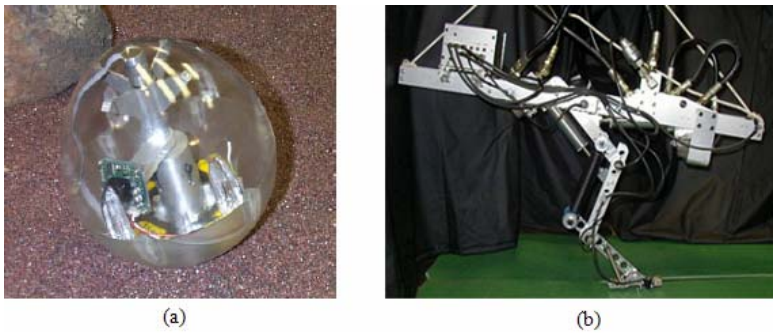

Figure 1.4: Examples of hopping robots. (a) Hopbot [11]; (b) Kenken [12].

Hopping is another possible solution [13, 14]. The advantage of such mechanism is less number of actuator required as compared with legged robot. Also, it is able to jump over high obstacle, due to its light weight, and compact size, as depicted in Fig. 1.4. The principal drawbacks are its unpredictable landing condition, and special mechanism is needed to adjust itself back to initial orientation for the next jump.

Figure 1.5: GMD snake-like robot [15].

Caterpillars, or snake-like robots [15] with simple control are able to demonstrates very good off-road abilities because of their good friction coefficient during motion. Its disadvantage is the friction losses between surface and the caterpillar when the robot is turning high. Also, it is not easy to construct snake-like robot, due to the possible large number of parts and the compact size of such configuration, as depicted in Fig. 1.5.

The last category of robot belongs to the wheeled mobile robots (WMRs). Carefully contrast wheeled with the other types of locomotion, the legged and snake-like robot required complicated mechanisms. The landing and recovery problems faced by hopping robot are still in development. On the basis of simplicity, efficiency, light weight, and ease of control, the wheeled locomotion was chosen. However the mobility of wheeled locomotion over rough terrain faces its limitation due to its surmountable height over obstacles that is not more than one third of the wheel diameter. In order to improve the surmountable height of the robot, a special mechanism is required. Hence, these raised the needs to produce a statistically stable locomotion mechanism that enables a robot to move freely in outdoor environment without affecting its high speed

performance on flat terrain.

1.3 Rover Locomotion

Various mechanisms were proposed to solve above mentioned problem. In general, two types of mechanisms, *active* locomotion and *passive* locomotion, are considered. *Active* locomotion required to have prior knowledge of ground condition, and to vary motion parameters in line with it. The *passive* locomotion, means the robot can adapt to terrain passively, the ground condition is not considered in trajectory planning.

1.3.1 Wheeled Rovers with Active Mechanism

Many robots with active mechanism are developed and prototyped. The robots with additional actuated degrees of freedom combined with *walking wheel* are mainly focused. The mechanism allows the robot to precisely and actively adjust the location of center of gravity of robot. As a result, such a robot is said to have better mobility in the outdoor environment than other types of mobile robots. However, the active locomotion normally requires extended resources and complex mechanism.

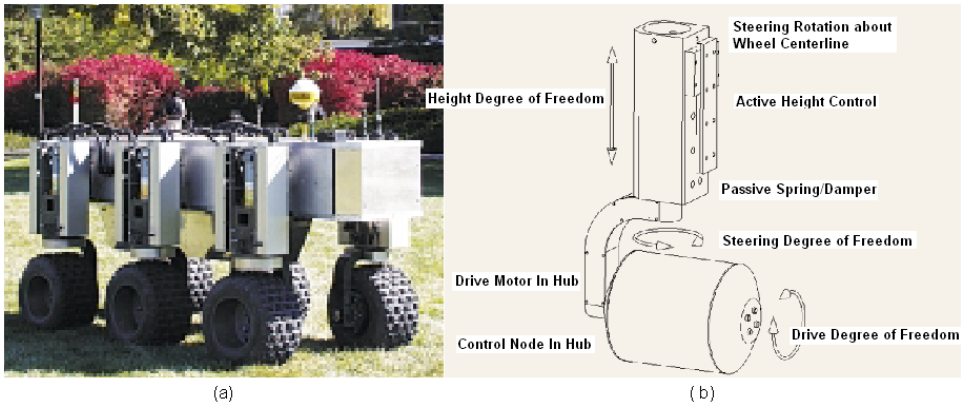

Figure 1.6: The USU's T2 ODV autonomous mobile robot [18]. (a) The robot on site; (b) The USU smart wheel.

The Nomad robot [16], Octopus robot [17], and the six-wheeled omni-directional autonomous mobile robot [18] represent the above active configurations. The six-wheeled omni-directional autonomous mobile robot developed by Utah State University (USU) requires six additional actuators for each walking wheel, as depicted in Fig. 1.5. The *active height control* improves the mobility of the robot by actively lift the wheel to overcome the obstacle. Also, additional sensors are needed to measure the height of the obstacle.

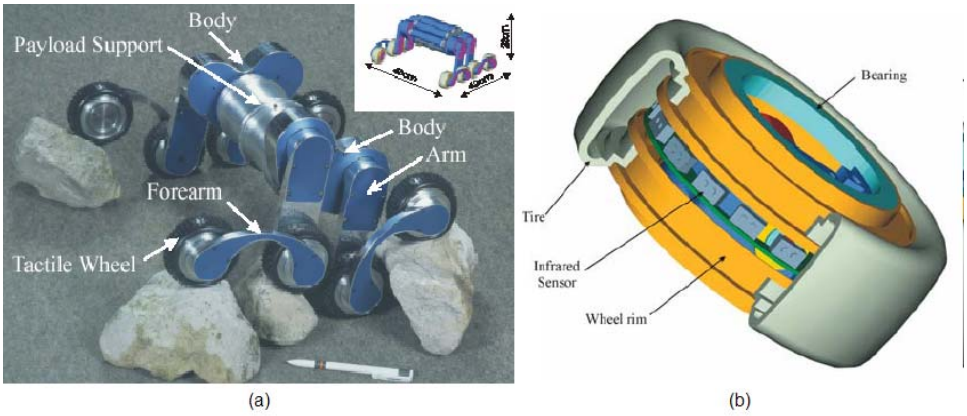

Figure 1.7: The EPFL's Octopus robot [17]. (a) The robot on site; (b) Tactile wheel and infrared sensors.

The Octopus robot [17] shown in Fig. 1.7, was developed by EPFL Autonomous Systems Laboratory using tactile wheels to detect the terrain profile. It was done by mounting series of infrared sensors on the circumference of each wheel. The sensor measures the tire deformation caused by the ground contact forces.

Nomad designed by Field Robotic Center of the Carnegie Mellon University (CMU), employed the unique transforming chassis design, as shown in Fig. 1.8 (b). It consists four steerable wheels and the steering angles of the wheels on each side are linked with a 4 bar mechanism and a lead screw. In order to distribute the normal forces on the wheels, NOMAD has two floating side frames called bogies. Each bogie is a structure that supports and deploys two wheels (left right). By allowing the side frames to pivot on a central axle, the

wheels can conform uneven terrain and maintain even ground pressure.

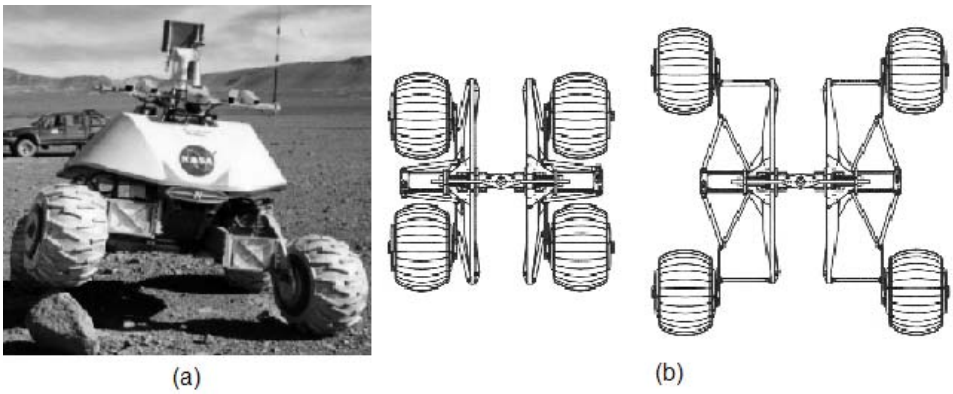

Figure 1.8: (a) CMU's Nomad [16]; (b) Nomad's transforming chassis in stowed (left) and deployed (right) positions. [19]

1.3.2 Wheeled Rovers with Passive Mechanism

High cross-country ability and maneuverability are the major requirements for mobile robots intended for operation on natural terrain. Many leg-wheel platforms have been developed for a variety of uneven terrain exploration. The Rocky 8 robot [20], Shrimp robot [21], Micro 5 [22], robot are all trying to combining the adaptability of legs with the efficiency of the wheels. The special mechanism allows the robot passively adapts to the terrain, means no active intervention is needed to handle the terrain.

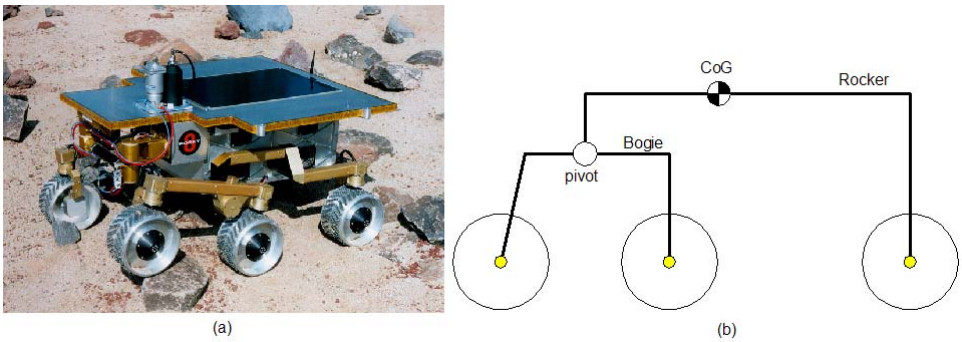

Figure 1.9: The NASA's Rocker 8 [20]. (a) The robot on site; (b) Schematic of the Rocker-Bogie Suspension.

The Rocky 8, designed by NASA, can go over an obstacle 1.5 times the

wheel diameter, which is 30 cm for the 20 cm wheels. It has a passive suspension system called *Rocker-Bogie Suspension*, which works well at low velocity. NASAs currently favored design, as shown in Fig. 1.9, consists of two rocker arms, one end of the main rocker arm is connected to the pivot of secondary rocker, also named as bogie, and the other end has a wheel attached. There are 6 wheels, 3 on a side of robot. The wheels are evenly spaced about twice the wheel diameter apart. The front and back wheels are steerable.

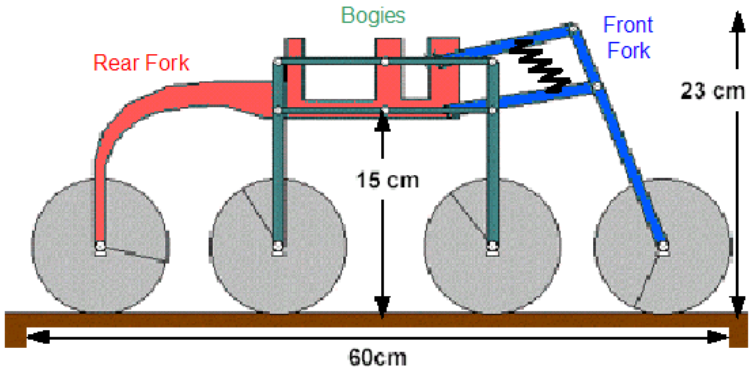

Figure 1.10: EPFL's Shrimp Robot [21].

The Shrimp robot, designed by Swiss Federal Institute of Technology Lausanne (EPFL), arranged the wheels in a rhombus, that is 1 front wheel, two pairs of middle wheels, then 1 trailing wheel, as shown in Fig. 1.10. The two middle wheels on each side are connected with links, four-bar configuration, and the front wheel has a 4 link suspension with a spring. The four bar mechanism, or called bogie, can freely rotate around central pivots. And, the steering is done by front and rear wheel. The unique design ensures that the instantaneous center of rotation is always situated under the wheel axis. The robot, measuring only about 60 cm in length and 20 cm in height, is able to passively overcome obstacles of up to 2 times its wheel diameter, which is 20 cm for the 10 cm wheels [21].

Micro 5, the rover developed in 2002 [22], is measured about 53 cm in breadth, 55 cm in length, and 25 cm in height, with wheel diameter is 10 cm.

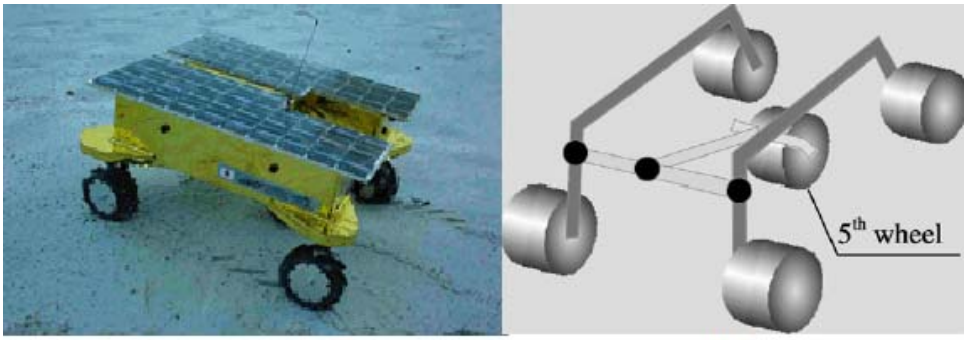

Figure 1.11: The Micro 5 [22]. (a) The robot on site; (b) Mechanism of PEGASUS system.

It has a passive suspension system called "PEntad Grade Assist SUSpesion" (PEGASUS). It consists of conventional four wheel arrangement and a fifth supported wheel connected by the link, as shown in Fig. 1.11 (b). The link and the body are connected with a passive rotary joint. The robot is able to overcome step 1.5 times the wheel diameter, and the climbable slope is about 40^o.

1.3.3 Remarks

Most of the rovers discussed so far are designed only to move forward and backward. The changing of the robot orientation is done by varying the angular velocities of left and right drive motors (differential steering), likes Micro 5, or install a steerable drive wheel, likes Rocker 8. The wheels are controlled by two motors, one for locomotion and one for steering. In the usual arrangement, the wheels are linked together using gears, rollers, chains, or pulleys. However, the limitation of this design is the mobile robot has to keep changing wheels orientation, which causes time delay, while tracking a discontinuous trajectory likes zigzag path. The next sections of the literature review shall discuss the concept of implementing an all directional wheels structure, otherwise known as the Omni Directional Mobility, to remedy the above mentioned movement

restriction.

1.4 The Wheel Mechanisms for Omni-Directional Mobility

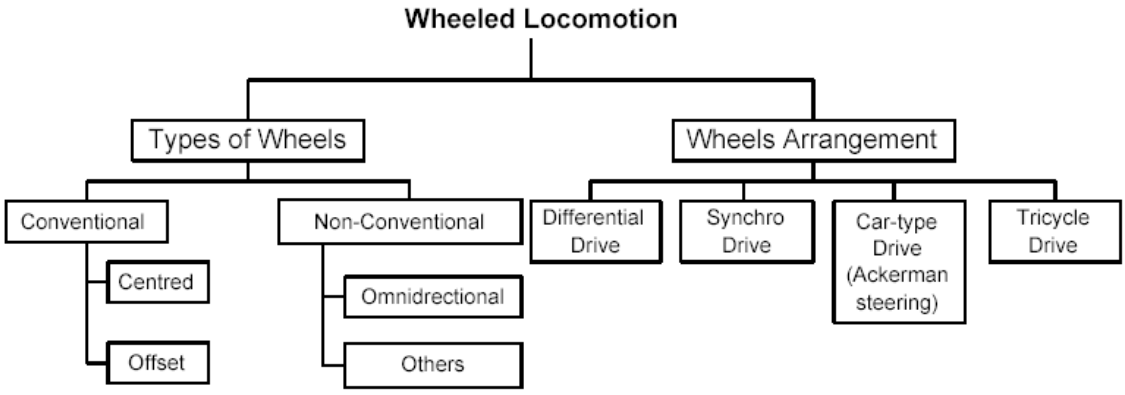

Figure 1.12: Block diagram of wheeled locomotion.

Under the umbrella of wheeled locomotion, as shown in Fig. 1.12, many types of wheels are available [23, 24]. Commercially available, there are two types of conventional wheels, namely, *centre* and *offset* wheels. And, WMRs built with conventional wheel can be classified into four main types of wheel arrangements, based on the way they are driven and steered. They are *differential* drives, *synchronous* drives, *tricycle* drives and *car-like* drives. General conventional WMRs cannot move sideways, as a result mobile robots with such wheels are capable only for two degree-of-freedom (DOF) motions. Consider, for example, a simple operation such as side parking required many forward and backward motions for car-like driving WMRs. As a result, the WMRs required an unnecessarily large space when move along a complicated path. To cope with this problem, various omni-directional drives have been proposed. The author will discussed the four different wheel mechanisms, which will provide mobility of three, namely, *conventional wheel* mechanism, *orthogonal*

wheel mechanism, *universal wheel* mechanism, and *ball wheel* mechanism.

1.4.1 Omni-Directional Mobility with Conventional Wheel Mechanism

The manoeuvrability of conventional WMRs is limited because they cannot move sideways without preliminary manoeuvring [31]. Various mechanisms have been investigated and developed to have better motion capabilities. One potential solution is to install an independent steering and driving mechanism in each wheel. The design that uses three centred wheels with above mechanism has been reported [25]. These design may be termed as omni-directional as the robot is capable of continuously changing its orientation. However, with this design, the robot cannot follows a trajectory with discontinuous heading without delay. For example, the robot is tasked to track a 90 degree trajectory, it needs to stop at the turning point, and turn its wheels 90 degrees as a preliminary action.

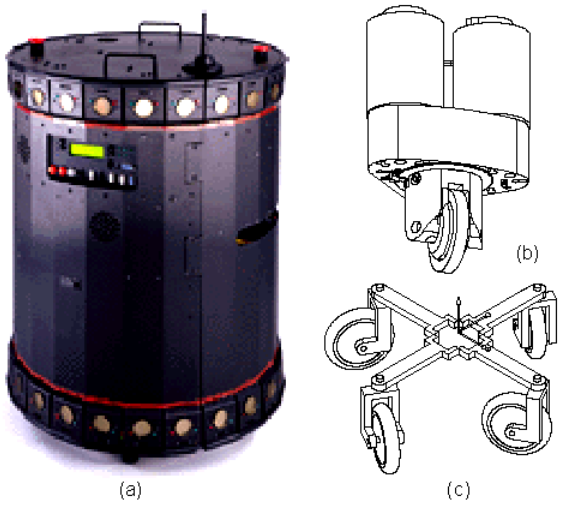

Figure 1.13: (a) Nomad XR4000 [28]; (b) Nomad's powered caster module; (c)Nomad's base.

WMRs with offset steered wheels have been discussed in [26, 27, 28, 29]. For instance, Nomad XR4000 [28], is a mobile robot composed of a main body and

four *offset orientable* wheels with independently powered steering and rotation axes, as depicted in Fig 1.13. However, the system experienced possible drift, when varying its wheels orientation without rolling . Also, these system need redundant actuators to avoid singular steering link configuration [30].

1.4.2 Omni-Directional Mobility with Orthogonal-Wheel Mechanism

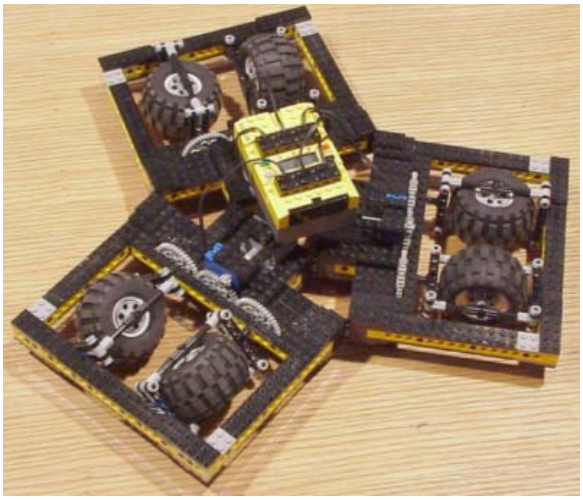

Figure 1.14: Killoughs platform.

Orthogonal-Wheel Mechanism [31] consists of two spheres of equal diameter which have been sliced to resemble wire round tire wheels. The spheres are assembled at 90 degrees from each other as shown in Fig 1.14. The arrangement provides normal traction in the given direction while free wheeling in the other perpendicular direction. However, the configuration may leads to significant odometry error and potential source of vibration, since one of the spheres can temporarily lose contact with the ground on rough terrain. In addition, the wheel assembly is bulky when compared to other types of wheel mechanisms.

1.4.3 Omni-Directional Mobility with Univesal Wheel Mechanism

Another means to achieve perfect mobility is to use omni-directional wheel (ODW), also known as *Mecanum* wheel or Univesal wheel. Mecanum wheels were originally patented in the early 1970s by Swedish inventor Bengt Erland Ilon [32]. A comprehensive discussion on the variants of the ODWs can be found in the literature [33, 34]. Numerous attempts have been made to practically implement Ilons idea. However, these attempts have typically focused on 3 , arranged in a $\triangle$ manner [35, 36], as shown in Fig. 1.15 (a), or 4-wheel, as shown in Fig. 1.15 (b) and (c), arranged in rectangular manner [37, 38].

Omni-directional wheels are not steered, as the wheel is direct coupling with the motor mounted on chassis. A series of passive elliptical rollers are mounted at a α degree angle to the wheel plane of rotation. When a wheel is rotated, the resulting motion tends to move the wheel at a α degree angle to its plane of rotation. By the individual motion created by each wheel, the mobile robot can move in any desired direction.

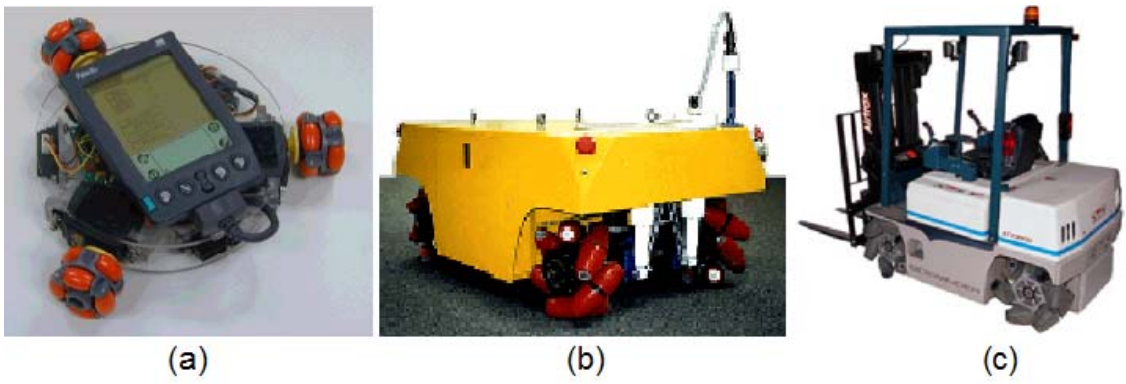

Figure 1.15: Examples of OWMR with omni-directional wheel mechanism. (a) Palm Pilot Robot [39]; (b) US NAVY's ODV [40]; (c) Airtrax's Omni-direXtional forklift [41].

Recent developments in the Omni-directional Wheeled Mobile Robots (OWMRs), which incorporated alternate types of ODW, have been reported [39, 40, 41].

WMRs manoeuvrability is improved from the ability to have independent control of mobile robot motion in the longitudinal, lateral, and rotational directions without the singular characteristics of a conventional wheel. This capability reduces the space and time required for mobile robot movement, which is a significant advantage in all applications, especially in space constrained or obstacle intensive environments. However, the drawbacks of such design are limited load capacity and vertical vibration. In addition, the ODW is more complex than a conventional wheel and more difficult to fabricate. With exception of ODW, the design and fabrication of OWMRs is straightforward. This type of OWMR is currently commercially available as shown as Fig. 1.15. The Palm Pilot Robot Kit [39] is an easy to build, fully autonomous robot controlled by a Palm hand-held computer designed by the Carnegie Mellon Robotics Institude for educational purposes. On the other hand, the U.S. Navy has developed a unique, highly manuverable vehicle based on the similar technology [40]. The vehicle is capable of transporting 5,000 pounds onboard Navy ships. The Omni-direXtional Forklift designed by Airtrax [41] is the next generation forklift with omni-directional mobility. It is excel in applications requiring tight maneuvering, where turns are not possible and finite control is a must.

1.4.4 Omni-Directional Mobility with Ball Wheel Mechanism

The three wheel mechanisms discussed earlier does not possesses three degree of freedom without slipping characteristic. There are either single, or two degree freedom wheel. The ball wheel mechanism presented in [42] has all degrees of freedom of rotation of the ball, with no singularities. However, the regular maintenance is required as the dirt and friction will hinder the performance of such robot on smooth terrain. Also, it is hard to install the ball wheel to

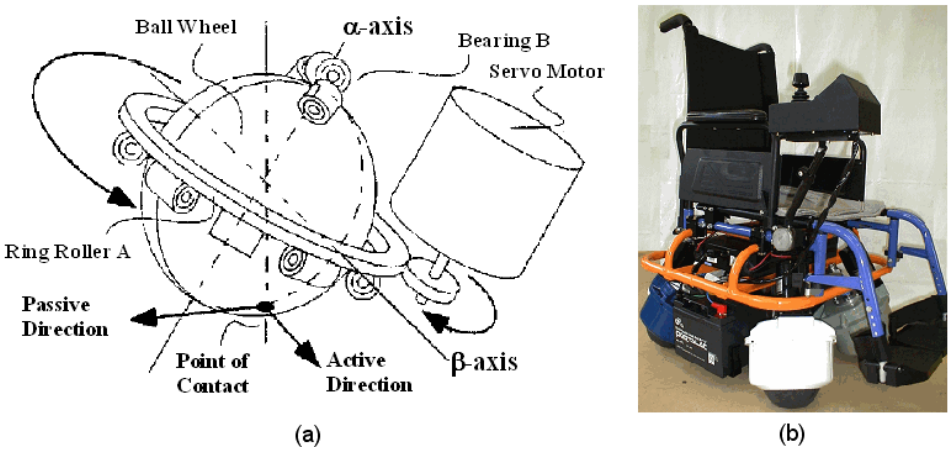

Figure 1.16: (a) Ball wheel unit [42]; (b) Wheelchair with *ball wheel* mechanism [44].

the robot chassis, while still allowing the ball to roll freely in any direction. Analyses of this type of WMRs have been documented [27, 42, 43], and the mechanism is currently commercially available as the base of wheelchair [44], as shown in Fig. 1.16.

1.4.5 Remarks

Note that, WMRs with omni-directional drive have a mobility of three, can be further distinguished as *holonomic* and *non-holonomic* system. Angeles, J. [45] defined that the system has at least one non-integrable generalized-velocity constraint is called *non-holonomic*. It means the system is called *holonomic*, only if all constraints of the system, linear in the generalized velocities, are integrable. The simplified version is, a robot is *nonholonomic* if it can not move to change its pose instantaneously in all available directions. Furthermore, *Holonomic* system can move instantaneously to any direction from an arbitrary configuration [46]. In short, the WMRs possessing three degrees of freedom without singularity, without regards to the rigid bodies which make up the actual mechanism, can be referred as *holonomic* mobile system.

1.5 Summary

There are several different factors that need to be considered when it comes to choosing right locomotion for the mobile robot. According to Everett [4], the main design issue effect the selection of appropriate locomotion are, *maneuverability*, *controllability*, *climbing ability*, *stability*, *efficiency*, *maintenance*, and *navigational considerations*. The present work aims to design and develop a wheeled mobile robot with high mobility not only on flat terrain but also on undulating terrain. One of the similar projects is the omni-directional step climbing robot designed by [47] as depicted in Fig. 1.17. The vehicle combines seven ODWs and a passive rocker-bogie suspension system. However, the maximum height of the step that the vehicle able to overcome is 100 mm step [47], which is smaller than its wheel diameter 132 mm. After surveying

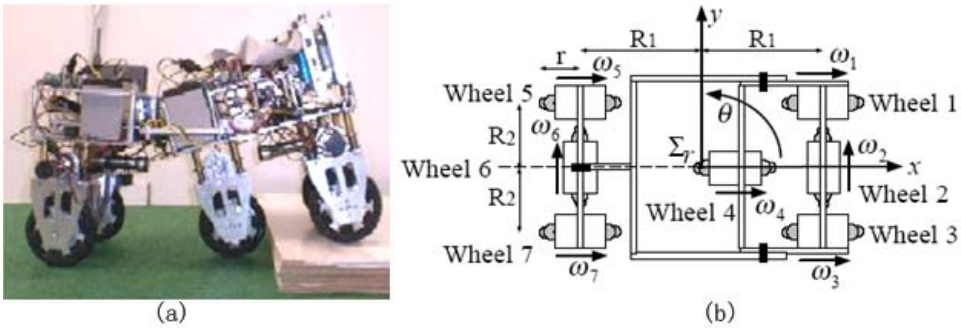

Figure 1.17: (a) The omni-directional step climbing robot [47]; (b) The vehicle wheel arrangement.

on the available options, it would be ideal to combine the omni-directional mobility of ODW and the Shrimp robot mechanism, which provides the best step climbing capability, two times its wheel diameter. Also, Shrimp robot is the only robot with tested stair climbing abilities. In addition, the author only considers that the improvement of step climbing ability in fixed direction since it is easier to design, and the robot can always re-position itself to desired direction.

1.6 Contribution of Research Work

The main contributions achieved in this work listed below:

1. The composite kinematic model for 6-wheel ODR with omnidirectional wheel is derived.
2. Two redesigned omni-directional wheels, namely *double wheel* mechanism, and *Mecanum* wheel mechanism, are fabricated and tested.
3. A working prototype of WMR with three omni-directional wheels.
4. The motion of ODR is studied.
5. The ODR geometry constraints for stair climbing is determined.
6. The feedback control system is setup.
7. The conceptual and detailed design of a ODR with six omni-directional wheels is developed.
8. A working prototype of ODR with six omni-directional wheels is developed and tested.

1.7 Overview of Report

This report is organized into 8 chapters. In Chapter 1, an overview of the potential applications for mobile robot, and the works completed by past researchers has been reviewed. Chapter 2 will shows the kinematics and dynamics analysis of ODR. Chapters 3 and 4 present the 2D and 3D simulation of ODR and preliminary motion analysis of ODR. Chapter 5 will outline the design goals and constraints. The detailed design of ODR and redesigned ODWs will also be discussed. The detailed design of ODR and redesigned ODWs will also be discussed. In Chapter 6, the experimental setup used in our tests will

be described in detail. This covers the feedback control system, velocity profile planning, and tele-operation system. Chapter 7 will then show the results obtained during ride testing. Finally, Chapter 8 provides the overall evaluation and recommendations for future works.

Chapter 2

Kinematics and Dynamic Analysis of ODRs

In this chapter the kinematics and dynamics of the omni-directional rover (ODR) is considered. To simplify the task, the author will only discuss the kinematics of the omni-directional wheeled platform, followed by the kinematic and dynamic analysis of the ODR locomotion. An understanding of the kinematics of the six-ODWs platform is fundamental to designing a planning and control system. The results of the kinematics and dynamics of the locomotion are essential to compute required driving torque.

2.1 Kinematics of a Rover with Six Omni Directional Wheels

The following procedures developed by [23, 24] were carried out in order to determine the kinematics of the six-wheel omni-directional rover (ODR). In its simplest form, an ODR consists a *platform* sub-system that is supported by n wheel sub-systems. These sub-systems may be of the same type or a combination of various types. Thus, an ODR can be decomposed into the platform sub-system and the wheel sub-systems, as shown in Fig. 2.1. The wheel Jacobian matrix will be used to relate the motion of each wheel to the motion of the robot and, subsequently combining the individual wheel

equations to obtain composite kinematic equation of motion for robots. The advantage of this approach is that different wheel sub-systems can be modelled separately to create templates to be used latter which is applicable to our case. Two wheel sub-systems, namely *double wheel* and *helix wheel*, shall be derived separately and subsequently assembled with platform sub-system to form the overall ODR model.

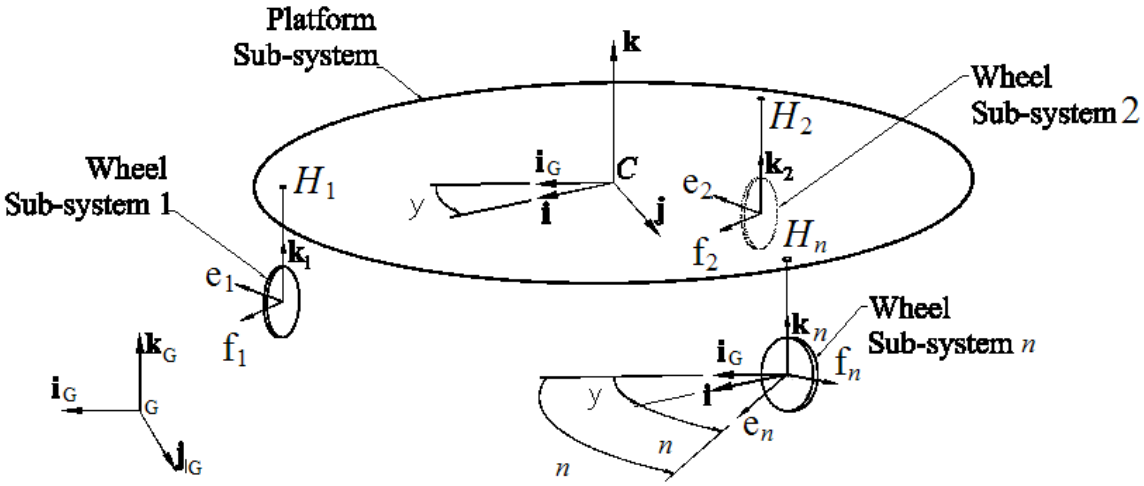

Figure 2.1: Sub-systems of a WMR.

2.1.1 General Considerations

In this analysis, we assume that the ODR is a mechanical system which is composed of rigid bodies connected by ideal joints, and operating on a regular horizontal surface, free of obstacles; and the translational friction at the point of contact between the wheel (modelled as a thin disk) and ground is large enough to prevent slippage. It means no side slip and rolling slip occur and wheel center consistent with the ODR turning.

In addition, a single, fixed, continuous contact point between each wheel and the terrain is assumed. It means only one roller at a time is in contact with the floor. In the case of ODR, the plane of the wheel does not vary

such that the motion algorithms and task descriptions can be described in term of homogeneous coordinates. In order to simplify our analysis, the sub-systems coordination is mapped to platform coordination through rotational transformation. The analysis starts from general platform kinematics and wheel kinematics.

2.1.2 Sub-System Models - Platform Kinematics

The geometry architecture of 3-DOF ODR, as shown in Fig. 2.2, is considered for analysis purposes. The platform is modelled as a hexagonal slab, which moves on a horizontal plane. Its pose can be described by an orientation and two position variables, and can be represented as $[\psi \quad \mathbf{c}^T]^T$. The ODR consists of 6 ODWs and a platform, which consists of three sections, namely front fork (wheel 6), bogies (wheels 1, 2, 4, 5), and rear fork (wheel 3). Also, the front and rear wheels are *double wheel* and all bogies wheel are *helix wheel*. The configuration is set to maintain the omni-directional mobility while maintaining the stability of ODR in forward motion.

In Fig. 2.2, ψ is the angle of the platform orientation with respect to the fixed reference frame G, and $\mathbf{c}$ is the two dimensional position vector of the platform centre, which is taken as the *operation point* C [48]. Therefore, the necessary number of generalised coordinates q required to describe the configuration of the platform is three. We can thus call q, the degrees of freedom [49]. Moreover, the fixed reference frame G, which in dynamics is usually inertia, is selected so that the ODR moves on the XY plane, while $\mathbf{i}_G$, $\mathbf{j}_G$ and $\mathbf{k}$ are unit vectors, where $\mathbf{k}$ points upward in the vertical direction. Next, we define a body-frame, whose orientation is fixed with respect to the platform, its associated unit vectors, $\mathbf{i}$, $\mathbf{j}$ and $\mathbf{k}$, being shown in Figs. 2.1 and 2.2. Furthermore, the body-frame rotates with respect to the reference frame G about a vertical axis with an angular velocity $\dot{\psi}$. The velocity of point C in

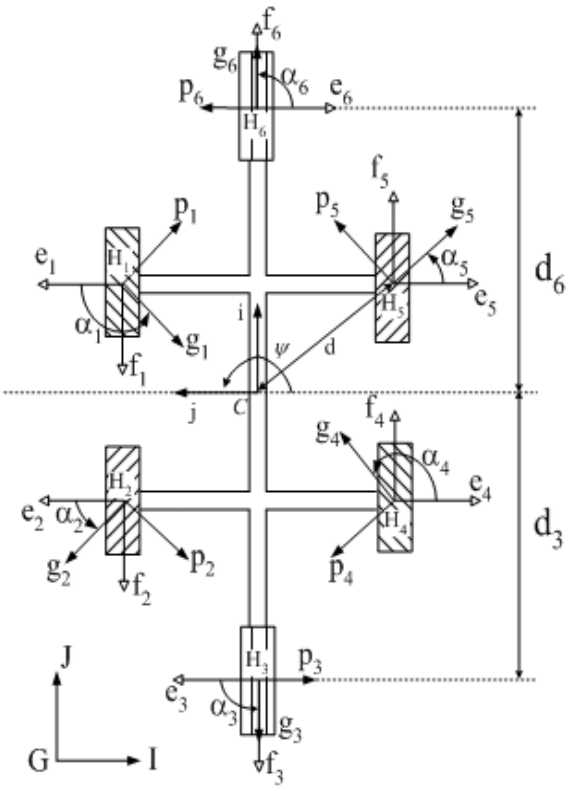

$$\alpha_1 = 135°, \alpha_2 = 45°, \alpha_3 = 90°, \alpha_4 = 135°, \alpha_5 = 45°, \alpha_6 = 90°$$
$$\lambda_1 = 45°, \lambda_2 = 135°, \lambda_3 = 180°, \lambda_4 = 225°, \lambda_5 = 315°, \lambda_6 = 0°$$

Figure 2.2: Notation for the analysis of platform

body-attached frame is the given by

$$\dot{\mathbf{c}} = \dot{x}\mathbf{i} + \dot{y}\mathbf{j} = \mathbf{R}_\psi \dot{\mathbf{c}}_G \tag{2.1}$$

,where $\mathbf{R}_\psi$ is the 2×2 rotation matrix in the plane, given by

$$\mathbf{R}_\psi \equiv \begin{bmatrix} \cos\psi & \sin\psi \\ -\sin\psi & \cos\psi \end{bmatrix} \tag{2.2}$$

Note that the velocity of point C in fixed reference frame is

$$\dot{\mathbf{c}}_G = \dot{X}\mathbf{i}_G + \dot{Y}\mathbf{j}_G \tag{2.3}$$

Next, the absolute velocity of an arbitrary point H_n, is

$$\dot{\mathbf{h}}_n = \dot{\mathbf{c}} + \dot{\psi}\mathbf{E}\mathbf{d}_n \tag{2.4}$$

where

$$\mathbf{E} \equiv \begin{bmatrix} 0 & -1 \\ 1 & 0 \end{bmatrix} \tag{2.5}$$

is a 2×2 skew symmetric matrix [48] associated to rotating vectors in the plane through an angle of 90° counter-clockwise, while $\mathbf{d}_n$ is the two dimensional vector directed from C to H_n (n=1 to 6), where n is the wheel number as shown in Fig. 2.2.

The *planar twist* of the platform, denoted by $\mathbf{t}$, is defined as

$$\mathbf{t} = [\dot{\psi} \quad \dot{\mathbf{c}}^T]^T \tag{2.6}$$

This vector has three components, one for rotation, $\dot{\psi}$, and two for the translation, grouped in the two-dimensional vector $\dot{\mathbf{c}}$. Equation (2.4) can be rearranged as

$$[\dot{\mathbf{h}}_n] = [\mathbf{1} \qquad \mathbf{E}\mathbf{d}_n] \begin{bmatrix} \dot{\mathbf{c}} \\ \dot{\psi} \end{bmatrix} \tag{2.7}$$

where $\mathbf{1}$ is the 2×2 identity matrix, thereby completing the intended kinematic analysis of the platform sub-system considered. Furthermore, since the plane of the wheel does not vary, it is more convenient to express the unit vector $\mathbf{g}_n$ of the wheel coordinates in the body-attached frame such that,

$$[\mathbf{g}_\mathrm{n}] = \begin{bmatrix} \cos(90°\mathrm{m} + \alpha_\mathrm{n}) \\ \sin(90°\mathrm{m} + \alpha_\mathrm{n}) \end{bmatrix} \tag{2.8}$$

,where m = 1, for n = 1 .. 3, and m = -1, for n =4 .. 6.

2.1.3 Sub-System Models - Wheel Kinematics

The wheel kinematics discussed in this section start with the defining the coordinates as shown in Fig. 2.3. The wheel coordinate, $\mathbf{e}_n$, $\mathbf{f}_n$, and $\mathbf{k}_n$ are attached to the centre of the n^{th} wheel, where $\mathbf{e}_n$ is the axis of rolling, and $\mathbf{f}_n$ is normal to $\mathbf{e}_n$ and parallel to even terrain. The orientation of the unit vector $\mathbf{k}_n$ is always same as $\mathbf{K}$, which is common for all wheels unit vectors point upward in the vertical direction.

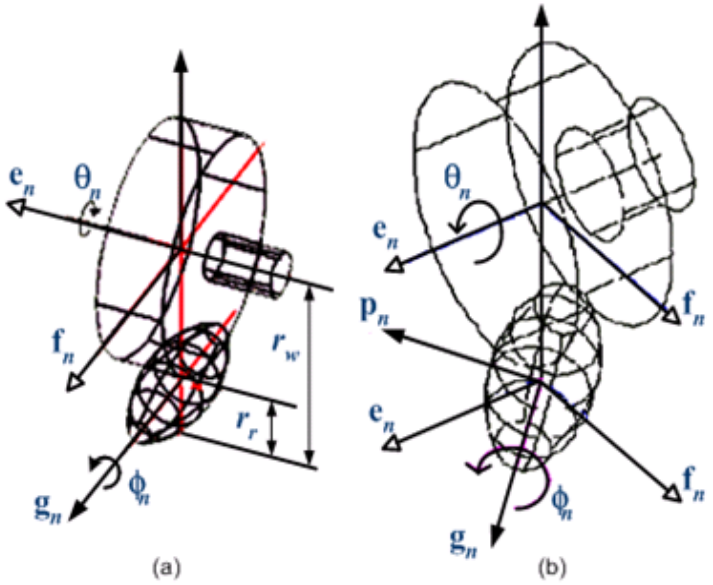

Figure 2.3: Notation for an omni-directional wheel: (a)Double Wheel;(b)Helix Wheel.

The roller coordinate, $\mathbf{g}_n$, and $\mathbf{p}_n$ are attached to the centre of the n^{th} roller, where $\mathbf{g}_n$ is the axis of rolling, and $\mathbf{p}_n$ is normal to $\mathbf{g}_n$ and parallel to wheel coordinate. The α_n refers to the angle between the vector $\mathbf{f}_n$ and $\mathbf{g}_n$. The rolling angle of the n^{th} wheel is denoted by θ_n and the radius of the wheel is denoted by r_w, which is the distance from the point H_n to the point of contact between roller and ground. Furthermore, the rolling angle and the radius of the passive roller are denoted by ϕ_n and r_r, respectively. The velocity of point

H_n can be determined from the spinning of the wheels and rollers, such that

$$\dot{\mathbf{h}}_n = -r_w\dot{\theta}_n\mathbf{f}_n + r_r\dot{\phi}_n\mathbf{p}_n \tag{2.9}$$

where $\dot{\mathbf{h}}_n$ is the two dimensional velocity of the centre of wheel.

2.1.4 Kinematic Modelling of 6-Wheel OWMR

By equating the eq. 2.7 with eq. 2.9 we obtain the relationship between the velocity of the platform and the velocity of the wheel, namely,

$$\dot{\mathbf{c}} + \mathbf{E}\mathbf{d}_n\dot{\psi} = -r_w\dot{\theta}_n\mathbf{f}_n + r_r\dot{\phi}_n\mathbf{p}_n \tag{2.10}$$

Only $\dot{\theta}_n$ can be controlled through the actuator of the n^{th} wheel, while $\dot{\phi}_n$ accommodates itself to allow for pure rolling of the roller with respect to the ground. Since all these rollers are unactuated, the values of $\dot{\phi}_n$ are not controllable therefore not required in our analysis. To eliminate $\dot{\phi}_n$, we take the inner product of eq. 2.10 and $\mathbf{g}_n$, which is normal to $\mathbf{p}_n$,thereby deriving

$$\mathbf{g}_n^T\dot{\mathbf{c}} + \mathbf{g}_n^T\mathbf{E}\mathbf{d}_n\dot{\psi} = -r_w\dot{\theta}_n\mathbf{g}_n^T\mathbf{f}_n, \quad n = 1, ..., 6 \tag{2.11}$$

or, since $\mathbf{g}_n^T\mathbf{f}_n = \sin\alpha_n$,

$$\mathbf{g}_n^T\dot{\mathbf{c}} + \mathbf{g}_n^T\mathbf{E}\mathbf{d}_n\dot{\psi} = -r_w\dot{\theta}_i\sin\alpha_n, \quad n = 1, ..., 6 \tag{2.12}$$

The desired relations between wheel rates and platform twist can be obtained by rearranged and rewritten the eq. 2.12 in matrix form.

$$\mathbf{J}\dot{\theta} = \mathbf{K}\mathbf{t} \tag{2.13}$$

where the 6 x 6 Jacobian $\mathbf{J}$, the 6 x 3 Jacobian $\mathbf{K}$ and $\mathbf{t}$, the twist of the platform, are defined as

$$\mathbf{J} \equiv diag(-r_w \sin\alpha_1, ..., -r_w \sin\alpha_6), \quad \mathbf{K} \equiv \begin{bmatrix} \mathbf{g}_1^T\mathbf{E}\mathbf{d}_1 & \mathbf{g}_1^T \\ \vdots & \vdots \\ \mathbf{g}_6^T\mathbf{E}\mathbf{d}_6 & \mathbf{g}_6^T \end{bmatrix}, \quad \mathbf{t} \equiv \begin{bmatrix} \dot{\psi} \\ \dot{\mathbf{c}} \end{bmatrix} \tag{2.14}$$

2.1.5 Inverse Kinematics

The purpose of inverse kinematics is to obtain the individual wheel velocities, which will accomplish desired motion. In this 3-DOF ODR, the desired motion is determined by given body velocities and turning rate or so called triplet, $[\psi \quad \mathbf{c}^T]^T$. The wheel velocities $\dot{\theta}_n$ are determined from eq. 2.13. Firstly, the inverse of Jacobian matrix $\mathbf{J}$ is determined,

$$\mathbf{J}^{-1} = \mathtt{diag}(-\frac{1}{r_w \sin\alpha_1}, ..., \frac{1}{-r_w \sin\alpha_6}). \tag{2.15}$$

Once the inverse matrix is derived, the inverse kinematic equations are determined by multiplying it to both side of eq. 2.13.

$$\dot{\theta}_n = -\frac{1}{r_w} \begin{bmatrix} d & -1 & -1 \\ d & -1 & 1 \\ d_3 & -1 & 0 \\ d & 1 & 1 \\ d & 1 & -1 \\ d_6 & 1 & 0 \end{bmatrix} \begin{bmatrix} \dot{\psi} \\ \dot{x} \\ \dot{y} \end{bmatrix} \tag{2.16}$$

2.1.6 Kinematics Analysis of the Locomotion

Kinematics analysis is necessary as it provided a concise mathematical formulation to describe the position, velocity, and acceleration of the linkages.

Two methods, *graphical* techniques, and *analytical solution* technique, are commonly used to analyze linkages. The accuracy of the results obtained by graphical technique depends on the precision of the scale of the drawing. In our case, where the repetitive and extensive analyses are required, the second method is preferable as it can be programmed on a workstation.

In this section, the equations used to construct analysis for step climbing are developed in detail. For step climbing, the ODR's motion separated to four different cases as shown in Figs. 2.4, 2.5, 2.6, and 2.7. For the purpose of developing an analytical model, the geometric mechanisms can be formulated using *position loop equation, velocity loop equation, and acceleration loop equations* [50].

Case 1: Front wheel climbing step

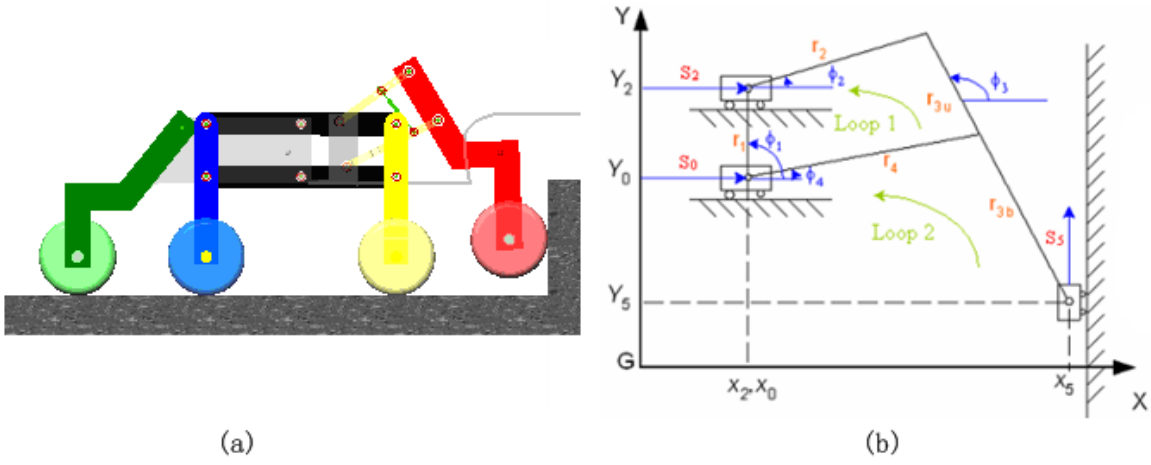

Figure 2.4: Case 1. (a) Front wheel is lifting. (b) Kinematic skeleton of the simplified front fork mechanism.

In Case 1, the rear wheel, wheels 1, and 2 are moving in constant velocity. The only moving part is front fork, where the front wheel is moving up vertically. As a result, the bogies and rear fork can be replaced by two sliders. The front fork is modeled as a six-bar linkage, where the mechanism is fully determined by specifying three variables, which is vertical displacement, S_5, and horizon-

tal displacements, S_0 and S_2. Fig. 2.4b shows the kinematic skeleton of the simplified model. By combining three displacement inputs, the fork mechanism will lift the slider up vertically. The links lengths r_2, r_4, r_{3u}, and r_{3b} are derived in Chapter 3. Also, all input slider starting locations, (X_0, Y_0), (X_2, Y_2), and (X_5, Y_5) are known. In order to simplify the analysis, S_0 and S_2 are equal, and the ϕ_1 is fixed.

Three position loop equations are determined by summing displacement around each of two loops. With two vector loops, four scalar position loop equations are obtained, as shown here:

1. Loop 1

$$f_1 = x_0 + S_0 + r_4 \cos\phi_4 - x_2 - S_2 - r_2 \cos\phi_2 + r_{3u} \cos\phi_3 = 0 \quad (2.17)$$

$$f_2 = Y_0 + r_4 \sin\phi_4 - Y_2 - r_2 \sin\phi_2 + r_{3u} \sin\phi_3 = 0 \quad (2.18)$$

2. Loop 2

$$f_3 = x_0 + S_0 + r_4 \cos\phi_4 - r_{3b} \cos\phi_3 - x_5 = 0 \quad (2.19)$$

$$f_4 = Y_0 + r_4 \sin\phi_4 = Y_5 + r_{3b} \sin\phi_3 + S_5 \quad (2.20)$$

Eq. (2.20) substitutes into eq. (2.18), therefore

$$f_5 = Y_5 + r_3 \sin\phi_3 + S_5 - Y_2 - r_2 \sin\phi_2 = 0 \quad (2.21)$$

There are three simultaneous, non linear equations in three unknowns ϕ_2, ϕ_3, and ϕ_4. For this system of equations, the vector of secondary kinematic unknowns is

$$\{s\} = \left\{ \begin{array}{ccc} \phi_2 & \phi_3 & \phi_4 \end{array} \right\}^T$$

Once a position loop equations are formulated, the next step is to determine the velocities of all links and points of interest in the ODR. The computed

results can be used to determine link's accelerations which are needed for the dynamic force calculation. When the position equations, f_1, f_3, and f_5, are differentiated with respect to time, the velocity loop equations are obtained. Recognizing that all link lengths are constant, including the ϕ_1, the resulting component equations are,

$$\dot{f}_1 = \dot{S}_0 - r_4\dot{\phi}_4 \sin\phi_4 - \dot{S}_2 + r_2\dot{\phi}_2 \sin\phi_2 - r_{3u}\dot{\phi}_3 \sin\phi_3 = 0 \tag{2.22}$$

$$\dot{f}_3 = \dot{S}_0 - r_4\dot{\phi}_4 \sin\phi_4 + r_{3b}\dot{\phi}_3 \sin\phi_3 = 0 \tag{2.23}$$

$$\dot{f}_5 = r_3\dot{\phi}_3 \cos\phi_3 + \dot{S}_5 - r_2\dot{\phi}_2 \cos\phi_2 = 0 \tag{2.24}$$

In matrix form, eqs. (2.22), (2.23), and (2.24) can be rearranged and rewritten as

$$\begin{bmatrix} \dot{S}_0 - \dot{S}_2 \\ \dot{S}_0 \\ \dot{S}_5 \end{bmatrix} = \begin{bmatrix} -r_2 \sin\phi_2 & r_{3u} \sin\phi_3 & r_4 \sin\phi_4 \\ 0 & -r_{3b} \sin\phi_3 & r_4 \sin\phi_4 \\ r_2 \cos\phi_2 & -r_3 \cos\phi_3 & 0 \end{bmatrix} \begin{bmatrix} \dot{\phi}_2 \\ \dot{\phi}_3 \\ \dot{\phi}_4 \end{bmatrix} \tag{2.25}$$

Note that, $\dot{S}_0$ is equal to $\dot{S}_2$ in this case. The 3 x 3 coefficient matrix in eq. (2.25) is the Jacobian matrix for the fork mechanism.

$$[J_v] = \begin{bmatrix} -r_2 \sin\phi_2 & r_{3u} \sin\phi_3 & r_4 \sin\phi_4 \\ 0 & -r_{3b} \sin\phi_3 & r_4 \sin\phi_4 \\ r_2 \cos\phi_2 & -r_3 \cos\phi_3 & 0 \end{bmatrix} \tag{2.26}$$

The inverse of the Jacobian matrix $[J_v]$ is

$$\begin{bmatrix} \frac{-\cos\phi_3}{r_2\mathrm{C}} & \frac{\cos\phi_3}{r_2\mathrm{C}} & \frac{-\sin\phi_3}{r_2\mathrm{C}} \\ \frac{-\cos\phi_3}{r_3\mathrm{C}} & \frac{\cos\phi_3}{r_3\mathrm{C}} & \frac{-\sin\phi_3}{r_3\mathrm{C}} \\ \frac{r_{3\mathrm{b}}(\mathrm{B}-\mathrm{C})}{\mathrm{A}} & \frac{(r_{3\mathrm{b}}-2r_3)\mathrm{C}-r_{3\mathrm{b}}\mathrm{B}}{\mathrm{A}} & \frac{r_{3\mathrm{b}}(\mathrm{E}-\mathrm{D})}{\mathrm{A}} \end{bmatrix} \tag{2.27}$$

where $\mathrm{A} = -r_4 r_3 \cos(-\phi_4 + \phi_2 - \phi_3) + r_4 r_3 \cos(\phi_4 + \phi_2 - \phi_3)$, $\mathrm{B} = \sin(\phi_2 + \phi_3)$,

C = $\sin(\phi_2 - \phi_3$, D = $\cos(\phi_2 + \phi_3)$, and E = $\cos(\phi_2 - \phi_3)$. Once the inverse matrix is derived, the angular velocities of links r_2, r_3, and r_4 are determined by multiply it to both side of eq. (2.25).

$$\begin{bmatrix} \dot{\phi}_2 \\ \dot{\phi}_3 \\ \dot{\phi}_4 \end{bmatrix} = \begin{bmatrix} \frac{\dot{S}_0 \cos\phi_3 - \dot{S}_5 \sin\phi_3}{r_2 \mathrm{C}} \\ \frac{\dot{S}_0 \cos\phi_2 - \dot{S}_5 \sin\phi_2}{r_3 \mathrm{C}} \\ \frac{2\dot{S}_0 r_3 \mathrm{C} + \dot{S}_0 r_{3b}(\mathrm{B}-\mathrm{C}) + \dot{S}_5 r_{3b}(\mathrm{D}-\mathrm{E})}{\mathrm{A}} \end{bmatrix} \tag{2.28}$$

Once a velocity analysis is done, the next step is to determine the accelerations of all links and points of interest in the ODR. The computed accelerations are used to calculate the dynamic forces, which contribute to the stresses in the links and other components, from $\mathbf{F}=m\mathbf{a}$. The analytical form of the acceleration equations can be developed by differentiating eqs. 2.22, 2.23, and 2.24. The resulting component equations are,

$$\begin{aligned} \ddot{f}_1 = {} & r_2 \left(\dot{\phi}_2\right)^2 \cos\phi_2 + r_2 \ddot{\phi}_2 \sin\phi_2 - r_{3u} \left(\dot{\phi}_3\right)^2 \cos\phi_3 \\ & - r_{3u} \ddot{\phi}_3 \sin\phi_3 - r_4 \left(\dot{\phi}_4\right)^2 \cos\phi_4 - r_4 \ddot{\phi}_4 \sin\phi_4 = 0 \end{aligned} \tag{2.29}$$

$$\ddot{f}_2 = \ddot{S}_0 + r_{3\mathrm{b}} \left(\dot{\phi}_3\right)^2 \cos\phi_3 + r_{3\mathrm{b}} \ddot{\phi}_3 \sin\phi_3 - r_4 \left(\dot{\phi}_4\right)^2 \cos\phi_4 - r_4 \ddot{\phi}_4 \sin\phi_4 = 0 \tag{2.30}$$

$$\ddot{f}_3 = \ddot{S}_5 + r_2 \left(\dot{\phi}_2\right)^2 \sin\phi_2 - r_2 \ddot{\phi}_2 \cos\phi_2 - r_3 \left(\dot{\phi}_3\right)^2 \sin\phi_3 + r_3 \ddot{\phi}_3 \cos\phi_3 = 0 \tag{2.31}$$

Again, eqs. (2.29), (2.30), and (2.31) are rearranged and rewritten in matrix form. Note that, the $\dot{\phi}_2$, $\dot{\phi}_3$, and $\dot{\phi}_4$ are calculated from velocity analysis.

$$\{R\} = [J_a] \left\{\ddot{\phi}\right\} \tag{2.32}$$

, where $\{R\} = \begin{bmatrix} R_1 & R_2 & R_3 \end{bmatrix}^T = \begin{bmatrix} r_2 \left(\dot{\phi}_2\right)^2 \cos\phi_2 - r_{3u} \left(\dot{\phi}_3\right)^2 \cos\phi_3 - r_4 \left(\dot{\phi}_4\right)^2 \cos\phi_4 \\ \ddot{S}_0 + r_{3\mathrm{b}} \left(\dot{\phi}_3\right)^2 \cos\phi_3 - r_4 \left(\dot{\phi}_4\right)^2 \cos\phi_4 \\ \ddot{S}_5 + r_2 \left(\dot{\phi}_2\right)^2 \sin\phi_2 - r_3 \left(\dot{\phi}_3\right)^2 \sin\phi_3 \end{bmatrix}$

and the $\left\{\ddot{\phi}\right\} = \begin{bmatrix} \ddot{\phi}_2 \\ \ddot{\phi}_3 \\ \ddot{\phi}_4 \end{bmatrix}$.

The angular acceleration of three links can be derived by multiplying inverse of matrix $[J_a]$ to both side of eq. (2.32), where $[J_a] = [J_v]$,

$$\begin{bmatrix} \ddot{\phi}_2 \\ \ddot{\phi}_3 \\ \ddot{\phi}_4 \end{bmatrix} = \begin{bmatrix} \frac{(R_2-R_1)\cos\phi_3 - R_3\sin\phi_3}{r_2 \mathrm{C}} \\ \frac{(R_2-R_1)\cos\phi_2 - R_3\sin\phi_2}{r_3 \mathrm{C}} \\ \frac{\mathrm{B}r_{3\mathrm{b}}(R_2-R_1)+\mathrm{C}(R_1 r_{3\mathrm{b}}+2R_2-R_2 r_{3\mathrm{b}})+R_3 r_{3\mathrm{b}}(D-\mathrm{E})}{r_4 r_3(\cos(\phi_4-\phi_2+\phi_3)-\cos(\phi_4+\phi_2-\phi_3))} \end{bmatrix} \tag{2.33}$$

Case 2: Wheel 1 climbing step

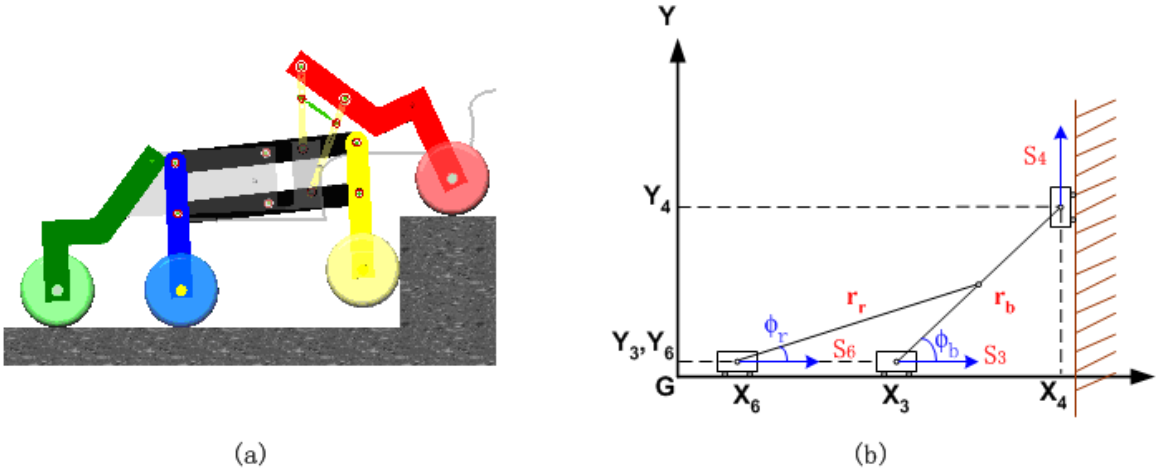

Figure 2.5: Case 2. (a) Wheel 1 is lifting. (b) Kinematic skeleton of the simplified bogies and rear fork mechanism.

In case 2, the front wheel, wheel 2, and rear wheel are moving in constant speed towards right. The system is fully determined by specifying three variables, which is vertical displacement, S_4, and horizontal displacements, S_3 or S_6. Fig. 2.5 shows the kinematic skeleton of the simplified model. Also, all input slider starting locations, (X_3, Y_3), (X_4, Y_4), and (X_6, Y_6) are known. In order to simplify the analysis, S_3 and S_6 are equal. Two scalar position loop equations are

$$f_1 = r_r \cos\phi_r + \frac{r_b}{2}\cos\phi_b - x_4 + x_6 + S_6 = 0 \tag{2.34}$$

$$f_2 = r_r \sin\phi_r + \frac{r_b}{2}\sin\phi_b - Y_4 + Y_3 - S_4 = 0 \tag{2.35}$$

Differentiation of eqs. (2.34) and (2.35) give the velocity loop equation

$$\dot{f}_1 = -\frac{1}{2}r_b\dot{\phi}_b \sin\phi_b - r_r\dot{\phi}_r \sin\phi_r + \dot{S}_6 = 0 \tag{2.36}$$

$$\dot{f}_2 = \frac{1}{2}r_b\dot{\phi}_b \cos\phi_b + r_r\dot{\phi}_r \cos\phi_r - \dot{S}_4 = 0 \tag{2.37}$$

Prior to solving for unknown velocities, these equations are rewritten in matrix form

$$\begin{bmatrix} -\dot{S}_6 \\ \dot{S}_4 \end{bmatrix} = \begin{bmatrix} -\frac{1}{2}r_b\sin\phi_b & -r_r\sin\phi_r \\ \frac{1}{2}r_b\cos\phi_b & r_r\cos\phi_r \end{bmatrix} \begin{bmatrix} \dot{\phi}_b \\ \dot{\phi}_r \end{bmatrix} \tag{2.38}$$

The inverse of the Jacobian matrix $[J_v]$, and $[J_a]$, the 2x2 coefficient matrix in eq. (2.38) are

$$[J_v] = [J_a] = \begin{bmatrix} -\frac{2\cos\phi_r}{r_b\sin(\phi_b-\phi_r)} & -\frac{2\sin\phi_r}{r_b\sin(\phi_b-\phi_r)} \\ \frac{\cos\phi_b}{r_r\sin(\phi_b-\phi_r)} & \frac{\sin\phi_b}{r_r\sin(\phi_b-\phi_r)} \end{bmatrix} \tag{2.39}$$

Once the inverse matrix is derived, the angular velocities of links r_b, and r_r are determined by multiply it to both side of eq. 2.38.

$$\begin{bmatrix} \dot{\phi}_b \\ \dot{\phi}_r \end{bmatrix} = \begin{bmatrix} \frac{2(\dot{S}_6\cos\phi_r - \dot{S}_4\sin\phi_r)}{r_b\sin(\phi_b-\phi_r)} \\ \frac{\dot{S}_4\sin\phi_b - \dot{S}_6\sin\phi_b}{r_r\sin(\phi_b-\phi_r)} \end{bmatrix} \tag{2.40}$$

The secondary acceleration of the mechanism can be developed by differentiating eqs. (2.36) and (2.37).

$$\ddot{f}_1 = -\frac{1}{2}r_b\left(\dot{\phi}_b\right)^2\cos\phi_b - \frac{1}{2}r_b\ddot{\phi}_b\sin\phi_b - r_r\left(\dot{\phi}_r\right)^2\cos\phi_r - r_r\ddot{\phi}_r\sin\phi_r + \ddot{S}_6 = 0 \tag{2.41}$$

$$\ddot{f}_2 = -\frac{1}{2}r_b\left(\dot{\phi}_b\right)^2\sin\phi_b + \frac{1}{2}r_b\ddot{\phi}_b\cos\phi_b - r_r\left(\dot{\phi}_r\right)^2\sin\phi_r + r_r\ddot{\phi}_r\cos\phi_r - \ddot{S}_4 = 0 \tag{2.42}$$

Again, eqs. (2.41), and (2.42) are rearranged and rewritten in matrix form.

Note that, the $\dot{\phi}_b$, and $\dot{\phi}_r$ are calculated from velocity analysis.

$$\{R\} = [J_a]\{\ddot{\phi}\} \tag{2.43}$$

where $\{R\}=[R_b \quad R_r]^T$

$$= \begin{bmatrix} \frac{1}{2} r_b \left(\dot{\phi}_b\right)^2 \cos\phi_b + r_r \left(\dot{\phi}_r\right)^2 \cos\phi_r - \ddot{S}_6 \\ \frac{1}{2} r_b \left(\dot{\phi}_b\right)^2 \sin\phi_b + r_r \left(\dot{\phi}_r\right)^2 \sin\phi_r + \ddot{S}_4 \end{bmatrix},$$

and the $\{\ddot{\phi}\}=[\ddot{\phi}_b \quad \ddot{\phi}_r]^T$. The angular acceleration of two links can be derived by multiplying inverse of matrix $[J_a]$ to both side of eq. (2.43), where $[J_a] = [J_v]$,

$$\begin{bmatrix} \ddot{\phi}_b \\ \ddot{\phi}_b \end{bmatrix} = \begin{bmatrix} -\frac{2(R_b\cos\phi_r + R_r\sin\phi_r)}{r_b\sin(\phi_b-\phi_r)} \\ \frac{R_b\cos\phi_b + R_r\sin\phi_b}{r_r\sin(\phi_b-\phi_r)} \end{bmatrix} \tag{2.44}$$

Case 3: Wheel 2 climbing step

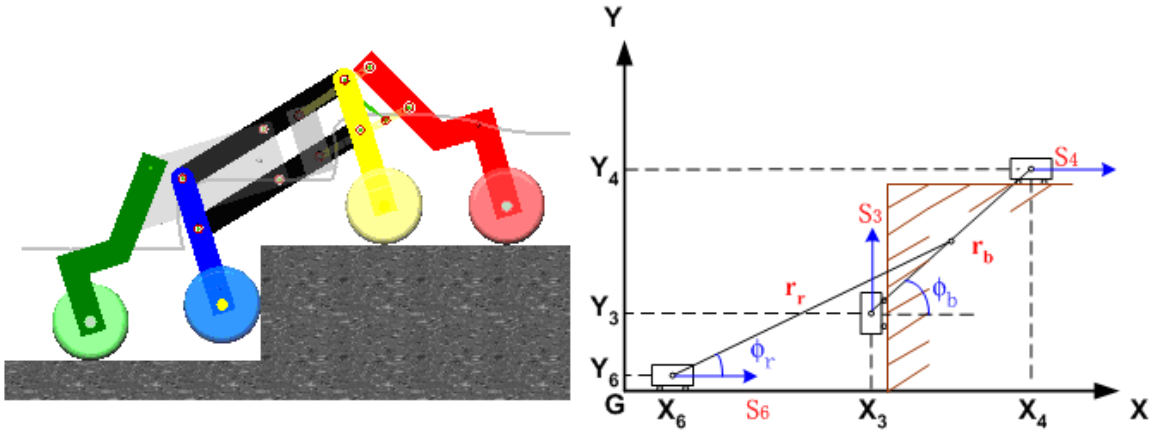

Figure 2.6: Case 3. (a) Wheel 2 is lifting. (b) Kinematic skeleton of the simplified bogies and rear fork mechanism.

In case 3, the front wheel, wheel 1, and rear wheel are moving in constant speed towards right. The system is fully determined by specifying three variables, which is vertical displacement, S_3, and horizontal displacements, S_4 and S_6. Fig. 2.6 shows the kinematic skeleton of the simplified model. Also, all input

slider starting locations, (X_3, Y_3), (X_4, Y_4), and (X_6, Y_6) are known. In order to simplify the analysis, S_3, S_6, and S_4 are equal. Two scalar position loop equations are

$$f_1 = x_6 + S_6 + r_r \cos\phi_r + \frac{r_b}{2}\cos\phi_b - x_4 - S_4 = 0 \tag{2.45}$$

$$f_2 = r_r \sin\phi_r - \frac{r_b}{2}\sin\phi_b - Y_3 + Y_6 - S_3 = 0 \tag{2.46}$$

Differentiation of eqs. (2.45) and (2.46) give the velocity loop equation

$$\dot{f}_1 = -\frac{1}{2}r_b\dot{\phi}_b \sin\phi_b - r_r\dot{\phi}_r \sin\phi_r + \dot{S}_6 - \dot{S}_4 = 0 \tag{2.47}$$

$$\dot{f}_2 = -\frac{1}{2}r_b\dot{\phi}_b \cos\phi_b + r_r\dot{\phi}_r \cos\phi_r - \dot{S}_3 = 0 \tag{2.48}$$

Prior to solving for unknown velocities, these equations are rewritten in matrix form

$$\begin{bmatrix} \dot{S}_4 - \dot{S}_6 \\ \dot{S}_3 \end{bmatrix} = \begin{bmatrix} 0 \\ \dot{S}_3 \end{bmatrix} = \begin{bmatrix} -\frac{1}{2}r_b \sin\phi_b & -r_r \sin\phi_r \\ -\frac{1}{2}r_b \cos\phi_b & r_r \cos\phi_r \end{bmatrix} \begin{bmatrix} \dot{\phi}_b \\ \dot{\phi}_r \end{bmatrix} \tag{2.49}$$

The inverse of the Jacobian matrix $[J_v]$, and $[J_a]$, the 2x2 coefficient matrix in eq. (2.49) are

$$\begin{bmatrix} -\frac{2\cos\phi_r}{r_b \sin(\phi_b - \phi_r)} & -\frac{2\sin\phi_r}{r_b \sin(\phi_b - \phi_r)} \\ -\frac{\cos\phi_b}{r_r \sin(\phi_b - \phi_r)} & \frac{\sin\phi_b}{r_r \sin(\phi_b - \phi_r)} \end{bmatrix} \tag{2.50}$$

Once the inverse matrix is derived, the angular velocities of links r_b, and r_r are determined by multiply it to both side of eq. 2.49.

$$\begin{bmatrix} \dot{\phi}_b \\ \dot{\phi}_r \end{bmatrix} = \begin{bmatrix} -\frac{2\sin\phi_r \dot{S}_3}{r_b \sin(\phi_b + \phi_r)} \\ \frac{\sin\phi_b \dot{S}_3}{r_r \sin(\phi_b + \phi_r)} \end{bmatrix} \tag{2.51}$$

The secondary acceleration of the mechanism can be obtained by differentiating

eqs. (2.47) and (2.48).

$$\ddot{f}_1 = -\frac{1}{2}r_b\left(\dot{\phi}_b\right)^2\cos\phi_b - \frac{1}{2}r_b\ddot{\phi}_b\sin\phi_b - r_r\left(\dot{\phi}_r\right)^2\cos\phi_r - r_r\ddot{\phi}_r\sin\phi_r + \ddot{S}_6 - \ddot{S}_4 = 0 \tag{2.52}$$

$$\ddot{f}_2 = \frac{1}{2}r_b\left(\dot{\phi}_b\right)^2\sin\phi_b - \frac{1}{2}r_b\ddot{\phi}_b\cos\phi_b - r_r\left(\dot{\phi}_r\right)^2\sin\phi_r + r_r\ddot{\phi}_r\cos\phi_r - \ddot{S}_3 = 0 \tag{2.53}$$

Again, the $\ddot{f}_1$,and $\ddot{f}_2$ are rearranged and rewritten in matrix form. Note that, the $\ddot{\phi}_b$ and $\ddot{\phi}_r$ are calculated from velocity analysis.

$$\{R\} = [J_a]\left\{\ddot{\phi}\right\} \tag{2.54}$$

where

$$\{R\} = \begin{bmatrix} R_b & R_r \end{bmatrix}^T = \begin{bmatrix} \frac{1}{2}r_b\left(\dot{\phi}_b\right)^2\cos\phi_b + r_r\left(\dot{\phi}_r\right)^2\cos\phi_r - \ddot{S}_6 + \ddot{S}_4 \\ -\frac{1}{2}r_b\left(\dot{\phi}_b\right)^2\sin\phi_b + r_r\left(\dot{\phi}_r\right)^2\sin\phi_r + \ddot{S}_3 \end{bmatrix}$$

, and the

$$\left\{\ddot{\phi}\right\} = \begin{bmatrix} \ddot{\phi}_b \\ \ddot{\phi}_r \end{bmatrix}$$

. The angular acceleration of three links can be derived by multiplying inverse of matrix $[J_a]$ to both side of eq. 2.54, where $[J_a] = [J_v]$,

$$\begin{bmatrix} \ddot{\phi}_b \\ \ddot{\phi}_r \end{bmatrix} = \begin{bmatrix} -\frac{2(R_b\cos\phi_r + R_r\sin\phi_r)}{r_b\sin(\phi_b+\phi_r)} \\ -\frac{R_b\cos\phi_b - R_r\sin\phi_b}{r_r\sin(\phi_b+\phi_r)} \end{bmatrix} \tag{2.55}$$

Case 4: Rear wheel climbing step

The angular velocity and angular acceleration of various points of the mechanism can be determined directly by modeling the rear fork as a rod whose extremities slides, respectively, in a horizontal and a vertical track, as shown in Fig. 2.7. The coordinates x_b and y_6 of the extremities of the rod can be

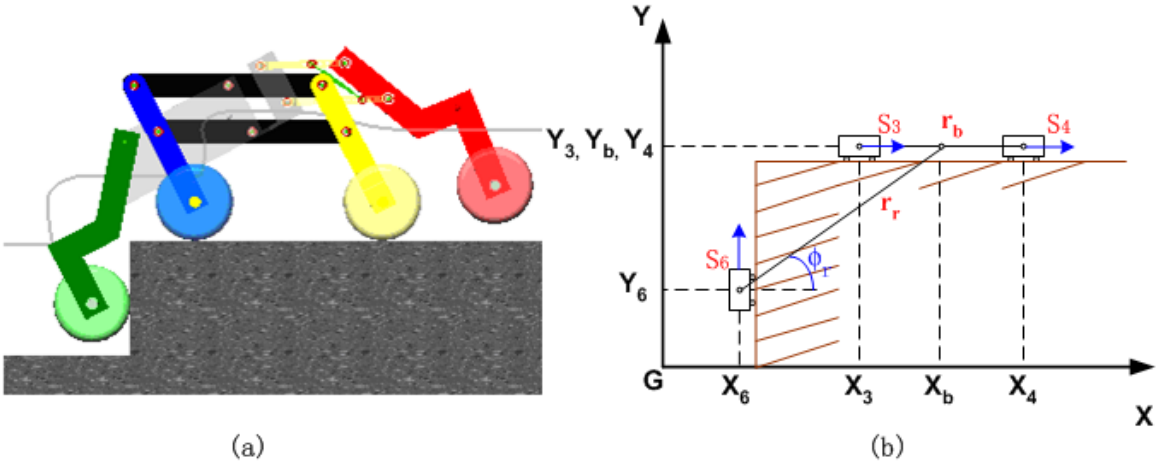

Figure 2.7: Case 4:(a) Rear wheel is lifting. (b) Kinematic skeleton of the simplified bogies and rear fork mechanism.

expressed in terms of the angle ϕ_r :

$$x_b + S_3 - x_6 = r_r \cos\phi_r \tag{2.56}$$

Differentiating eq. (2.56) twice with respect to t, the angular velocity and angular acceleration of link r_r are

$$\dot{S}_3 = -r_r\dot{\phi}_r \sin\phi_r, \quad \dot{\phi}_r = -\frac{\dot{S}_3}{r_r \sin\phi_r} \tag{2.57}$$

$$\ddot{S}_3 = -r_r\ddot{\phi}_r \sin\phi_r - r_r\left(\dot{\phi}_r\right)^2 \cos\phi_r, \quad \ddot{\phi}_r = -\frac{\ddot{S}_3 + r_r\left(\dot{\phi}_r\right)^2 \cos\phi_r}{r_r \sin\phi_r} \tag{2.58}$$

2.1.7 Dynamic Force Analysis of the Locomotion

After computing the geometry and a set of motion parameters for a particular design task using kinematic analysis mentioned in previous section, it is logical and convenient to then use inverse dynamic solution to determine the forces and torques in the system. In this section, the Newtonian solution method, which is written as summation of all forces and torques in the system, is used to solve the forces and torques required to drive the ODR to provide the design accelerations. The 2D-ODR consists 8 moving links and 4 wheels. The solution

requires that three motion equations for each link and three motion equation plus one constraint (rolling without slipping) for each wheel and then solved simultaneously. Figs. 2.8, 2.9, and 2.10 show the linkage "exploded" into its separate links, drawn as free body. A kinematic analysis must have been done in advance of this dynamic force analysis in order to determine, for each moving links, its angular velocities and angular accelerations of its CoG. Also, the mass (m) of each link and wheel, the location of CoG, and its moment of inertia (I_G) about that CoG are also need.

The naming convention of vector, $\mathbf{R}_{ab}$, used for the analysis is as follows. The first subscript a denotes the adjoining link to which the vector point. The second subscript b denotes the parent link where the vector belongs. Figs. 2.8, 2.9, and 2.10 show the free body diagrams for all links and wheels, with all force shown. Note that, four external torques, $\mathbf{T}_I$, $\mathbf{T}_{II}$, $\mathbf{T}_{III}$, and $\mathbf{T}_{IV}$, are shown acting on the wheels. There are total thirty-six unknowns presents in these thirty-six equations, F_{21x}, F_{21y}, F_{31x}, F_{31y}, F_{1Ix}, F_{1Iy}, F_{42x}, F_{42y}, F_{43x}, F_{43y}, F_{54x}, F_{54y}, F_{64x}, F_{64y}, F_{4IVx}, F_{4IVy}, F_{75x}, F_{75y}, F_{76x}, F_{76y}, F_{85x}, F_{85y}, F_{86x}, F_{86y}, F_{8IIx}, F_{8IIy}, F_{7IIIx}, F_{7IIIy}, T_I, T_{II}, T_{III}, T_{IV}, N_I, N_{II}, N_{III}, N_{IV}, so we can solve them simultaneously. This system can be solved by using Maple, MATLAB or any matrix solving operator.

Front Fork Link 1

$$F_{21_x}+F_{31_x}-F_{1\mathrm{I}_x}=m_1 a_{G_{1x}} \tag{2.59}$$

$$F_{21_y}+F_{31_y}-F_{1\mathrm{I}_y}-m_1 g=m_1 a_{G_{1y}} \tag{2.60}$$

$$R_{21_x}F_{21_y}-R_{21_y}F_{21_x}+R_{31_x}F_{31_y}-R_{31_y}F_{31_x}-R_{\mathrm{I}1_x}F_{1\mathrm{I}_y}+R_{\mathrm{I}1_y}F_{1\mathrm{I}_x}=I_{G_1}\alpha_1 \tag{2.61}$$

Front Fork Link 2

$$F_{42_x}+F_{2\mathrm{S}_x}-F_{21_x}=m_2 a_{G_{2x}} \tag{2.62}$$

$$F_{42_y}+F_{2\mathrm{S}_y}-F_{21_y}-m_2 g=m_2 a_{G_{2y}} \tag{2.63}$$

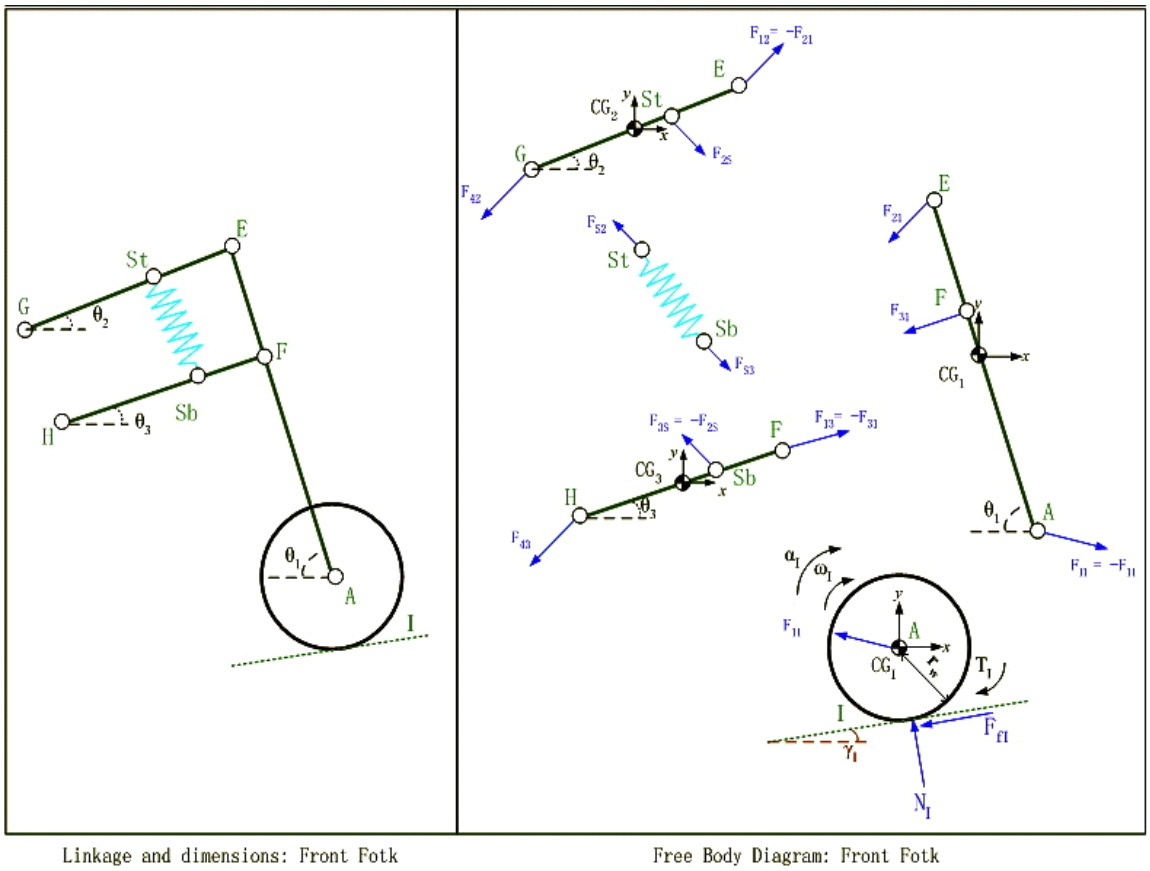

Figure 2.8: Free body diagram of front fork mechanism.

$$R_{42_x}F_{42_y} - R_{42_y}F_{42_x} + R_{2S_x}F_{2S_y} - R_{2S_y}F_{2S_x} - R_{12_x}F_{21_y} + R_{12_y}F_{21_x} = I_{G_2}\alpha_2 \quad (2.64)$$

Front Fork Link 3

$$F_{43_x} - F_{2S_x} - F_{31_x} = m_3 a_{G_{3x}} \quad (2.65)$$

$$F_{43_y} - F_{2S_y} - F_{31_y} - m_3 g = m_3 a_{G_{3y}} \quad (2.66)$$

$$R_{43_x}F_{43_y} - R_{43_y}F_{43_x} - R_{3S_x}F_{2S_y} - R_{3S_y}F_{2S_x} - R_{13_x}F_{31_y} + R_{13_y}F_{31_x} = I_{G_3}\alpha_3 \quad (2.67)$$

Front Fork Wheel I

$$F_{1I_x} - N_{I_x} - F_{fI_x} = m_I a_{G_{Ix}} \quad (2.68)$$

$$F_{1I_y} + N_{I_y} - F_{fI_y} - m_I g = m_I a_{G_{Iy}} \quad (2.69)$$

$$r_{wI_x} N_{I_x} - r_{wI_y} N_{I_y} + r_{wI_x} F_{fI_y} + r_{wI_y} F_{fI_x} + T_I = I_{G_I} \alpha_I \tag{2.70}$$

The above three equations involve four unknowns, namely, N_I, F_{fI}, a_{GI}, and α_I. Therefore, one more equation is needed in order to determine the remaining unknown. The additional equation is determined by assuming the wheel rolls without slipping.

$$a_{GI_x} = r_w \alpha_I \cos\gamma_I \ , \qquad a_{GI_y} = r_w \alpha_I \sin\gamma_I$$

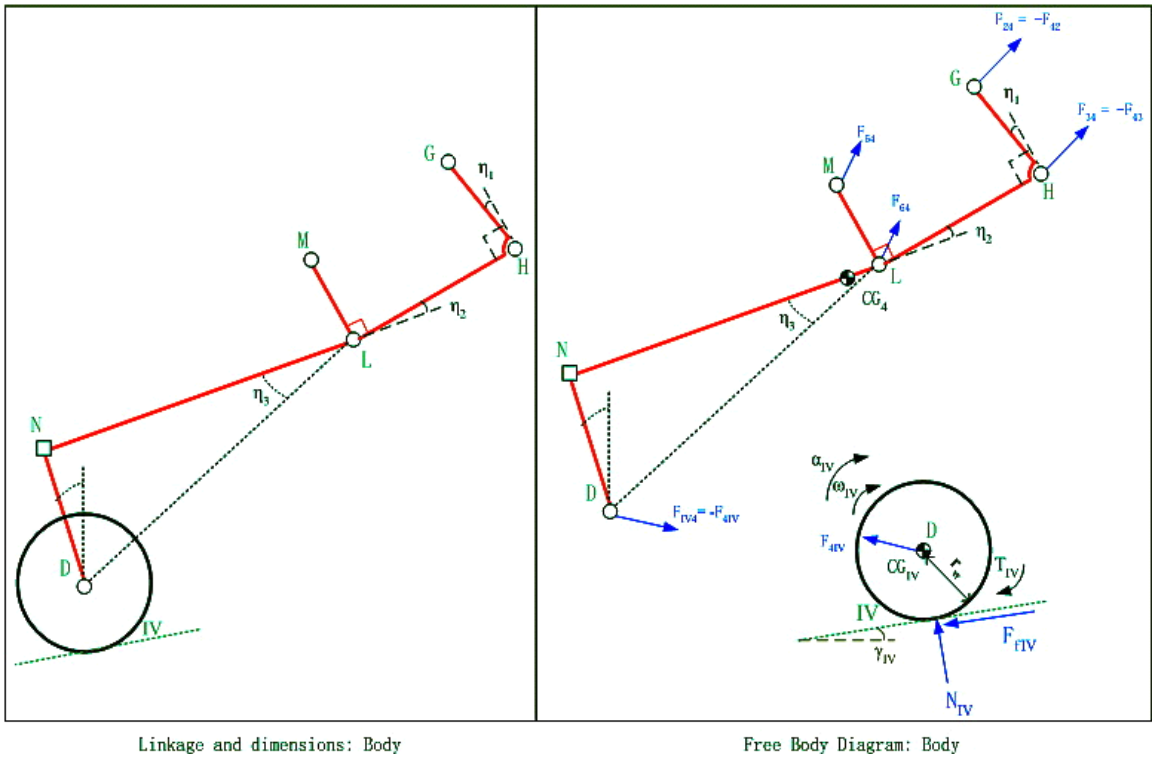

Figure 2.9: Free body diagram of rear fork mechanism.

Rear Fork - Link 4

$$F_{54_x} + F_{64_x} - F_{42_x} - F_{43_x} - F_{4\mathrm{IV}_x} = m_4 a_{G4x} \tag{2.71}$$

$$F_{54_y} + F_{64_y} - F_{42_y} - F_{43_y} - F_{4\mathrm{IV}_y} - m_4 g = m_4 a_{G4y} \tag{2.72}$$

$$R_{54_x} F_{54_y} - R_{54_y} F_{54_x} + R_{64_x} F_{64_y} - R_{64_y} F_{64_x} - R_{24_x} F_{42_y} + R_{24_y} F_{42_x}$$

$$-R_{34_x}F_{43_y} + R_{34_y}F_{43_x} - R_{\mathrm{IV}4_x}F_{4\mathrm{IV}_y} + R_{\mathrm{IV}4_y}F_{4\mathrm{IV}_x} = I_{G_{\mathrm{IV}}}\alpha_{\mathrm{IV}} \quad (2.73)$$

Rear Fork - Wheel IV

$$F_{4\mathrm{IV}_x} - N_{\mathrm{IV}_x} - F_{\mathrm{fIV}_x} = m_{\mathrm{IV}}a_{\mathrm{G_{IVx}}} \quad (2.74)$$

$$F_{4\mathrm{IV}_y} + N_{\mathrm{IV}_y} - F_{\mathrm{fIV}_y} - m_{\mathrm{IV}}g = m_{\mathrm{IV}}a_{G_{\mathrm{IVy}}} \quad (2.75)$$

$$r_{w\mathrm{IV}_x}N_{\mathrm{IV}_x} - r_{w\mathrm{IV}_y}N_{\mathrm{IV}_y} + r_{w\mathrm{IV}_x}F_{\mathrm{fIV}_y} + r_{w\mathrm{IV}_y}F_{\mathrm{fIV}_x} + T_{\mathrm{IV}} = I_{G_{\mathrm{IV}}}\alpha_{\mathrm{IV}} \quad (2.76)$$

$$a_{\mathrm{GIV}_x} = r_w\alpha_{\mathrm{IV}}\cos\gamma_{\mathrm{IV}}, \qquad \text{and } a_{GIV_y} = r_w\alpha_{\mathrm{IV}}\sin\gamma_{\mathrm{IV}}$$

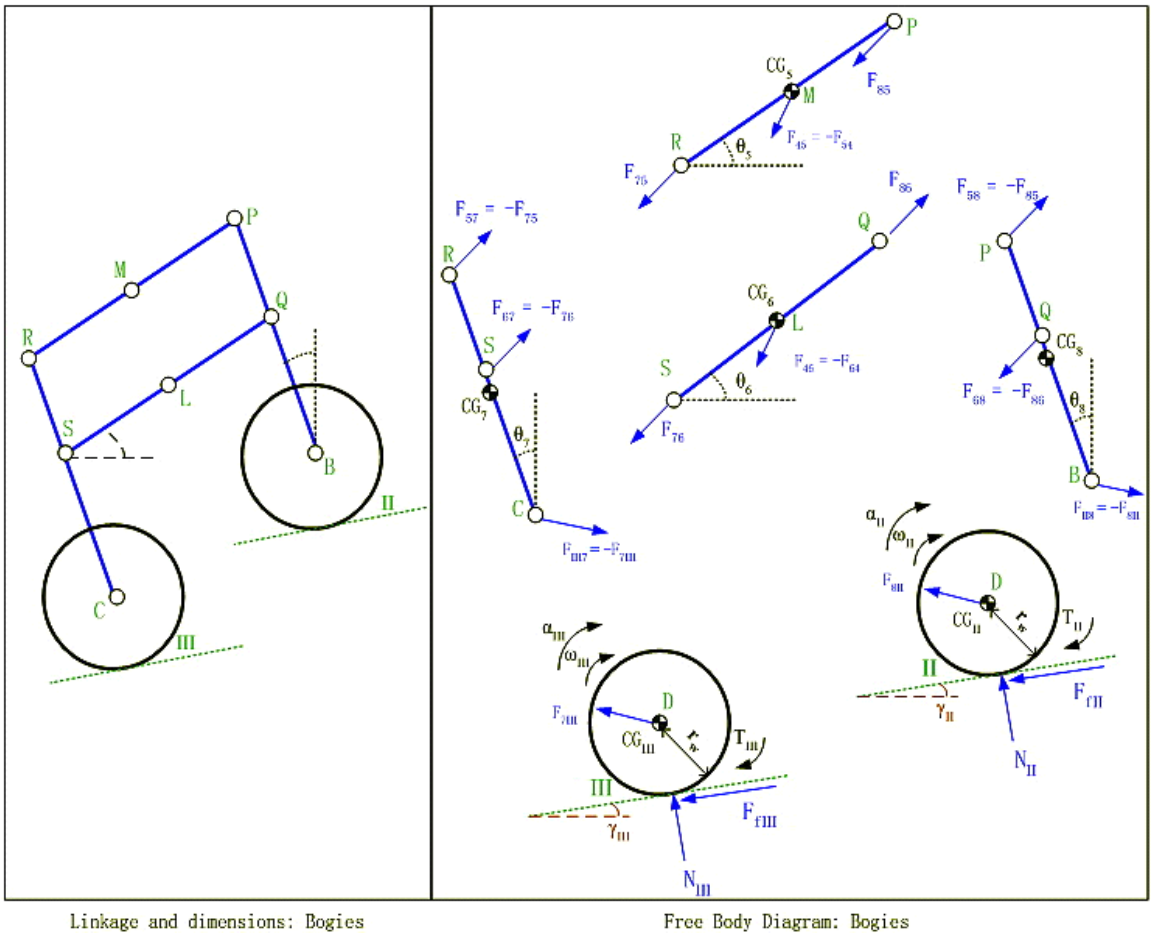

Figure 2.10: Free body diagram of bogies mechanism.

Bogies - Link 5

$$F_{85_x} + F_{75_x} - F_{54_x} = 2m_5a_{G_{5x}} \quad (2.77)$$

$$F_{85_y} + F_{75_y} - F_{54_y} - 2m_5 g = 2m_5 a_{G_{5y}} \tag{2.78}$$

$$R_{85_x} F_{85_y} - R_{85_y} F_{85_x} + R_{75_x} F_{75_y} - R_{75_y} F_{75_x} = 2I_{G_5} \alpha_5 \tag{2.79}$$

Bogies - Link 6

$$F_{86_x} + F_{76_x} - F_{64_x} = 2m_6 a_{G_{6x}} \tag{2.80}$$

$$F_{86_y} + F_{76_y} - F_{64_y} - 2m_6 g = 2m_6 a_{G_{6y}} \tag{2.81}$$

$$R_{86_x} F_{86_y} - R_{86_y} F_{86_x} + R_{76_x} F_{76_y} - R_{76_y} F_{76_x} = 2I_{G_6} \alpha_6 \tag{2.82}$$

Bogies - Link 7

$$-F_{75_x} - F_{76_x} - F_{7\mathrm{III}_x} = 2m_7 a_{G_{7x}} \tag{2.83}$$

$$-F_{75_y} - F_{76_y} - F_{7\mathrm{III}_y} - 2m_7 g = 2m_7 a_{G_{7y}} \tag{2.84}$$

$$-R_{57_x} F_{75_y} + R_{57_y} F_{75_x} - R_{67_x} F_{76_y} + R_{67_y} F_{76_x} - R_{\mathrm{III}7_x} F_{7\mathrm{III}_y} + R_{\mathrm{III}7_y} F_{7\mathrm{III}_x} = 2I_{\mathrm{G}_7} \alpha_7 \tag{2.85}$$

Bogies - Link 8

$$-F_{85_x} - F_{86_x} - F_{8\mathrm{II}_x} = 2m_8 a_{G_{8x}} \tag{2.86}$$

$$-F_{85_y} - F_{86_y} - F_{8\mathrm{II}_y} - 2m_8 g = 2m_8 a_{G_{8y}} \tag{2.87}$$

$$-R_{58_x} F_{85_y} + R_{58_y} F_{85_x} - R_{68_x} F_{86_y} + R_{68_y} F_{86_x} - R_{\mathrm{II}8_x} F_{8\mathrm{II}_y} + R_{\mathrm{II}8_y} F_{8\mathrm{II}_x} = 2I_{\mathrm{G}_8} \alpha_8 \tag{2.88}$$

Bogies - Wheel II

$$F_{8\mathrm{II}_x} - N_{\mathrm{II}_x} - F_{\mathrm{fII}_x} = 2m_{\mathrm{II}} a_{G_{\mathrm{II}x}} \tag{2.89}$$

$$F_{8\mathrm{II}_y} + N_{\mathrm{II}_y} - F_{\mathrm{fII}_y} - 2m_{\mathrm{II}} g = 2m_{\mathrm{II}} a_{G_{\mathrm{II}y}} \tag{2.90}$$

$$r_{w\mathrm{II}_x} N_{\mathrm{II}_x} - r_{w\mathrm{II}_y} N_{\mathrm{II}_y} + r_{w\mathrm{II}_x} F_{\mathrm{fII}_y} + r_{w\mathrm{II}_y} F_{\mathrm{fII}_x} + 2T_{\mathrm{II}} = 2I_{G_{\mathrm{II}}} \alpha_{\mathrm{II}} \tag{2.91}$$

$$a_{\mathrm{GII}_x} = r_w \alpha_{\mathrm{II}} \cos\gamma_{\mathrm{II}}, \qquad \text{and } a_{GII_y} = r_w \alpha_{\mathrm{II}} \sin\gamma_{\mathrm{II}}$$

Bogies - Wheel III

$$F_{7\mathrm{III}_x} - N_{\mathrm{III}_x} - F_{\mathrm{fIII}_x} = 2m_{\mathrm{III}}a_{G_{\mathrm{III}x}} \tag{2.92}$$

$$F_{7\mathrm{III}_y} + N_{\mathrm{III}_y} - F_{\mathrm{fIII}_y} - 2m_{\mathrm{III}}g = 2m_{\mathrm{III}}a_{G_{\mathrm{III}y}} \tag{2.93}$$

$$r_{w\mathrm{III}_x}N_{\mathrm{III}_x} - r_{w\mathrm{III}_y}N_{\mathrm{III}_y} + r_{w\mathrm{III}_x}F_{\mathrm{fIII}_y} + r_{w\mathrm{III}_y}F_{\mathrm{fIII}_x} + 2T_{\mathrm{III}} = 2I_{G_{\mathrm{III}}}\alpha_{\mathrm{III}} \tag{2.94}$$

$$a_{\mathrm{GIII}_x} = r_w\alpha_{\mathrm{III}}\cos\gamma_{\mathrm{III}}, \qquad \text{and } a_{GIII_y} = r_w\alpha_{\mathrm{III}}\sin\gamma_{\mathrm{III}}$$

Chapter 3

Preliminary Motion Analysis of ODR

3.1 General Considerations

Stability is one of the key elements contribute to the rover's overall effectiveness. To achieve statically stable, the rover locomotion needs to do four actions repeatedly in random order:

1. Remove the ground contact point of the rear wheel
2. Place new ground contact point in front of the rover
3. Shift the weight forward
4. Maintain the static equilibrium throughout all motions

In this chapter, the author will discuss the factors, like driving torque, wheel radius, the coefficient of friction of the wheel, that affect the performance of the rover on undulating terrain. The analytical synthesis, and simulation program, Interactive Physics [52], are used to study the motion behaviors of the spring suspension system and to determine the optimum geometry dimensions of the front fork linkage.

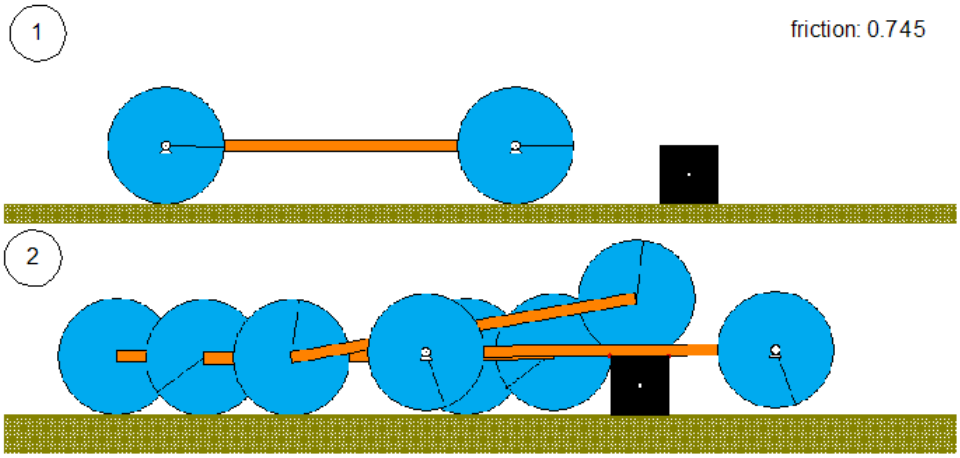

Figure 3.1: Two-dimentional simulation: Car-like WMR climbs over the obstacle.

3.1.1 Number of Wheels

Almost all WMRs adopted car-like wheel arrangement, which clearly have better performance on forward and backward motion compared with other arrangements. However, conventional four-wheel rover is only workable while the maximum height of obstacles is lower than one-third of its wheel diameter. For omni-directional WMRs, the surmountable height is only one-third of roller diameter when the wheel plane is facing obstacle. It is one of the reasons why the Omni-directional WMRs are not popular despite its superior mobility on even surface.

A configuration with a wheel base equal to three wheel diameters and a center of gravity midway between the wheels can be used as an example. If we place a vertical wall, where the wall height equals to the wheel radius, in front of both front wheels of such a vehicle, as depicted in Fig. 3.1. The front wheel will only rise when the coefficient of friction is 0.745 or greater. Given that the coefficients of friction of about 0.7 for dry roads and 0.4 for wet roads reported by Jones and Childers [54], which implies that the conventional car-like WMRs are not able to overcome axle-height obstacle without special mechanism on dry road.

In addition, another significant mobility problem was encountered after the front wheels climbs over the wall. The WMR often became stuck when a wall hit the exposed underside of the vehicle. This space, between the wheels, is an area of great vulnerability when climbing larger obstacle. As shown in Fig. 3.1, obstacle will strike the underside of the WMR, the weight of the WMR is taken off the wheels, causing a reduction in wheel traction. This often leads to the WMR becoming caught. To alleviate this problem, it was suggested to raise the pivot location of the bogie, which provides good terrain adaptability and in the same time keeping a maximum ground clearance [21]. However, an additional wheel is required to keep vehicle in balance.

Altering the number of wheels can significantly affect the system performance on undulating terrain. One of the decisive factors is having enough ground clearance to avoid possible damage on the chassis. In addition, it should be able to withstand a tilt of 45 degrees in any direction without tipping over. Also, all the wheels must maintain optimal ground contact at any time as the maximum amount of driving torque that can be created is limited by the amount of traction, not by the actuator. There is no way to harness the power if the wheel does not stick to the ground, as shown in Fig. 3.1. In the simulation, the five-wheel rover can climb up step height of 1.5 times its wheel diameter with coefficient of 0.8. Six wheels are better than five as it results more climbing traction, the required coefficient of friction is 0.6. Also, a lesser fraction of weight is being lifted, which implies lesser motor power or driving torque is needed. Although more wheels would perform better, but the added complexity and associated steering problems make the idea impractical.

3.1.2 The CoG of ODR

The movement of rover's center of gravity (CoG) is a dynamic phenomenon, and it plays an important role to system stability. As a rule of thumb, the

location of CoG should be as low as possible to avoid undesirable mass transfer effect like rover tips over. Also, it should be positioned toward the center of the rover to have equal weight on each wheel. The more weight on a wheel, the higher traction it has. However, the weight can shift as a rover moves. For instance, when a rover turning about a point, weight shifts to the outside wheels. When it accelerates, weight shifts to the rear wheels. For step or stair climbing, the ability of rover locomotion to transform sharp CoG movement to smooth rising of the CoG contributes to the system stability. Also, the CoG should be located closer to the front fork to reduce the burden on rear wheel. It is the major difference between the conventional WMRs and rover-like robot.

3.1.3 Wheel Diameter

In general, the maximum step height that the conventional car-like mobile robot can pass over depends on its wheel diameter. However, it is not practical to increase the wheel diameter to accommodate the general step height as the robot chassis will become too big. Also, the required driving torque will be increased. Therefore, it is necessary to keep wheel diameter small while maintaining optimum surmountable height through flexible mechanism.

3.1.4 Increasing Acceleration

For rover to overcome obstacle, the ability to maintain its motor output torque is very important. When a robot accelerates or decelerates, it is no longer being acted upon solely by the force of gravity, but also by the force of friction contact with the ground. Therefore, the change of velocity is achieved through vector sum of the above forces and the wheel driving forces yields the net direction and magnitude of force. In other words, the ability to achieve adequate acceleration is critical to drive the rover climbs up the obstacle. It is a function of the weight on the wheel, and coefficient of friction.

Weight of rover - Reducing weight could contribute to faster acceleration. By reducing the mass that must be accelerated for motion, less power would be required to produce the same rate of acceleration. Using a drive system that produced same amount of power would give a higher acceleration to the desired velocity. However, reducing the weight also reduces traction with the ground, so the net effect of reducing weight is questionable.

The coefficient of friction - From a theoretical standpoint, Newton's Laws state that the force required to accelerate a given mass at a given acceleration is equal to mass times acceleration. Thus, a heavier object would take more force than a lighter object to obtain an equal acceleration. However, the rover may be limited in acceleration by maximum frictional force. Classical theory of static friction states that the maximum force that can be applied to a static body is proportional to the normal force. Using equations, we can derive an equation for maximum acceleration of the robot to avoid wheel slip, which is proportional to the coefficient of friction, μ, time gravity, g.

$$a_{\max} = k\mu g$$

in which constant of proportionality k is related to the number of wheels, the positioning of the wheels with respect to the chassis, and the direction of acceleration. The above equation tells us that an easy way to increase the maximum acceleration of the robots is to increase the coefficient of friction. Thus, a great deal of effort was put into redesigning wheels and rollers, and performing tests to determine which could best grip the ground. There are several ways to alleviate this problem, and several have been looked at in greater depth.

The first step in increasing wheel-ground friction was to see what research had already been done on the subject. The conventional rubber wheel is only grip the ground by rubbing one surface against another. The wheel designed

by NASA engineers and used in Mars rovers adopts other mean to gain better traction. The wheel with "cleats" is able to dig into the terrain as deep as possible, as shown in Fig. 3.2.

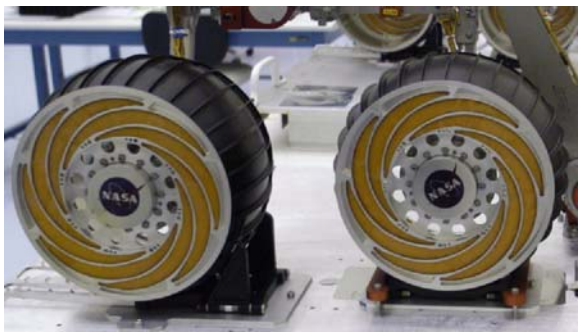

Figure 3.2: NASA mars exploration rover's wheel. [6]

This would in effect help the wheels to grip the ground not by frictional contact, but by contact of one vertical wall, the "cleats" on the wheels, against the terrain. However, the speed of robot would be limited due to possible high stress concentration acting on the cleats. A trade off between the traction and the optimum speed of the robot is necessary. Another possible solution is used different roller material, which provided better traction. After search through the internet, polyurethane is widely considered as popular choices for roller or wheel material. Polyurethane is the toughest of the elastomers used for wheel, characterized by high tensile strength, excellent abrasion resistance, and tear strength.

3.1.5 Suspension system

The ability to overcome obstacle is not the primarily a function of the wheels. It is the rover's suspension system determines the rover obstacle climbing ability. The Shrimp robot adopted spring suspension system to improves Shrimp's traction. However, the downward force increases when the front wheel is raised according to the spring rate. The increasing downward force makes it harder to lift the wheel as it reduces the remaining wheels' traction (rear and bogies

wheels) by reducing their downward force. On the other hand, the compressed spring force improves the shrimp's traction while the front wheel is on top of the step. The overall effect of the spring suspension system will be further discussed in the latter section.

3.1.6 Types of Obstacle

The function of rover is to move from point to point, and able to deal with obstacle autonomously without getting stuck. Obstacles are any physical characteristics of the terrain that impede the mobility of a force. Due to the vast amount of obstacles, it is necessary to define and restrict our analysis to a few specific obstacles. For this reason, the analyses were done to optimize the ability to climb slope and step initially. The concluding portion of the analysis would be channeled back to a more conventional urbanized structure common known as the staircase. To simplify the analysis, we assume that the rover will not climb up any obstacle that higher than the surmountable height of the rover or climb down since it will break the rover structures. In future, the rover with vision or other sensory systems will help to identify the types of the obstacle. In the next section, the author will describe the steps to obtain ODR's front fork optimum geometry configuration.

3.2 Parametric Studies and Optimization

The simulation software provides a general platform for conducting and plotting parametric studies. The results are saved in text files using tab-delimited format, and can be read by other software packages such as Excel for further post-processing and plotting.

The Shrimp's spring suspension is designed to ensure optimum ground contact of front wheel at any time and to produce a smooth elevation of the front

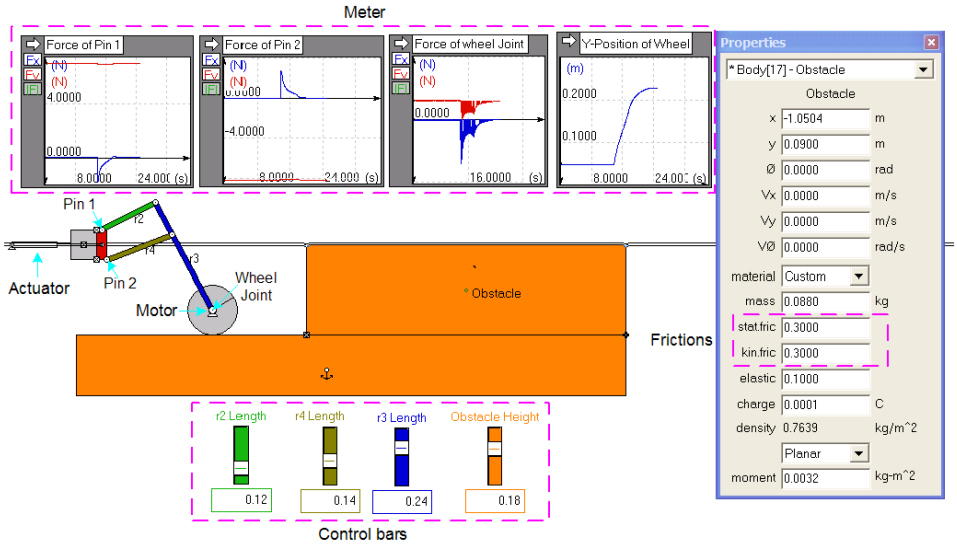

Figure 3.3: Interactive Physics: Front fork mechanism interface

wheel if an obstacle is encountered. To find an optimum front fork configuration, which give us maximum lifting height with minimum energy consumption, *analytical synthesis* and *simulation method* are used. Analytical synthesis allows us to determine front fork dimension based on given prescribed positions of mechanism. Then, the derived front fork is simulated in *Interactive Physics 2000*, as shown in Fig. 3.3. At first, the contact forces between the wheel and step, and the time required to climb up the step for different linkage configurations were recorded. Then, the front fork with different spring locations and spring constant were being investigated. After the optimum front fork configuration is determine, the 3D-model will be built to investigate its *terrainability* and *trafficability* [53] in structured environment.

2.2.2.1 Front Fork - Analytical Synthesis

Analytical synthesis allows us to determine front fork dimension based on prescribed positions of mechanism. The three-position synthesis is used to calculate the corresponding link lengths. Fig. 3.4 shows that the graphical configuration of fork mechanism, which is a typical six-bar linkage. If a local

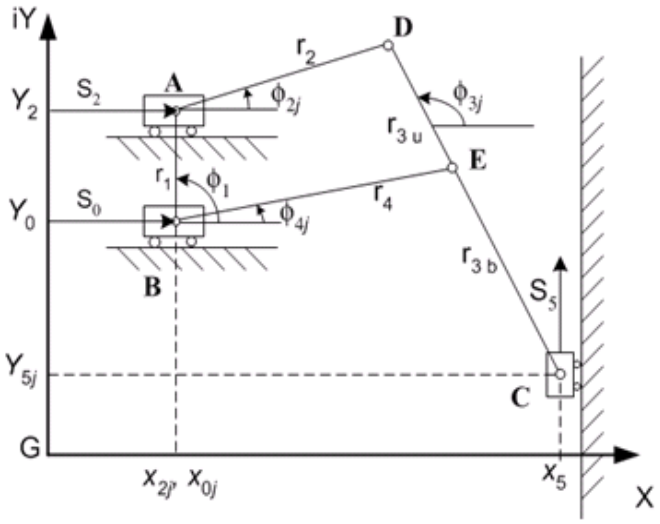

Figure 3.4: Kinematic skeleton of front fork mechanism.

coordinate system is attached to slider B, the sliders A and B will become fixed pivots, and the coordinate of point C will become $(X_{5j} - X_{0j}, Y_{5j})$, where j =1, 2, 3. As a result, the front fork mechanism can be synthesized for four-bar path generator.

In the present work, three-position synthesis is used to calculate the corresponding link lengths, r_2, r_4, r_{3u}, and r_{3b}. With three positions, the free choices can be made such that the resulting equations are linear, and thus easily solved. This leads to two infinities of solutions based on the two free choices. The difficulty here is the need to select values for the free choices, which is generally a non-intuitive task.

To simplify the calculation, the ϕ_1 is fixed, and all input slider locations, (X_0,Y_0), (X_2,Y_2), and (X_5,Y_5) are known. The vectors $\overline{AD}$ and $\overline{DC}$ form the left-hand dyad, ϕ_{2j} is the angle of rotation of the input, ϕ_{3j} is the rotation angle of the coupler, ϕ_{4j} is the rotation angle of the output, and $\overline{BE}$ and $\overline{EC}$ are the vectors forming the right-hand dyad, where j =1, 2, 3 for three position synthesis. Two loop-closure equations, which are often called the

standard-form equation for dyadic linkage synthesis, exist:

$$\overline{AD}\left(e^{i\beta_2}-1\right)+\overline{DC}\left(e^{i\alpha_2}-1\right)=\delta_2 \tag{3.1}$$

$$\overline{BE}\left(e^{i\beta_3}-1\right)+\overline{EC}\left(e^{i\alpha_3}-1\right)=\delta_3 \tag{3.2}$$

For the left-hand dyad, the prescribed positions are given by:

$$\mathbf{R}_j = (X_{5j} \text{ - } X_{0j}) + Y_{5j}i, \text{ where } j = 1, 2 ,3.$$

or, in simplified form, using the definition $\delta_j = R_j$ - R_1,

$$\delta_2 = R_2 \text{ -}R_1, \qquad \delta_3 = R_3 \text{ - } R_1.$$

Given:

$$\beta_2 = \phi_{22} \text{ - } \phi_{21}, \qquad \beta_3 = \phi_{23} \text{ - } \phi_{21},$$

$$\alpha_2 = \phi_{32} \text{ - } \phi_{31}, \qquad \alpha_3 = \phi_{33} \text{ - } \phi_{31}.$$

If δ_2, δ_3, α_2, and α_3 are prescribed, β_2 and β_3 can be picked arbitrarily such that the only unknowns are the vectors, $\overline{AD}$ and $\overline{DC}$. Equations 3.1 and 3.2 are linear and can be solved by Cramer's rule.

$$\overline{AD} = \frac{\begin{vmatrix} \delta_2 & e^{i\alpha_2}-1 \\ \delta_3 & e^{i\alpha_3}-1 \end{vmatrix}}{\begin{vmatrix} e^{i\beta_2}-1 & e^{i\alpha_2}-1 \\ e^{i\beta_3}-1 & e^{i\alpha_3}-1 \end{vmatrix}} \tag{3.3}$$

$$\overline{DC} = \frac{\begin{vmatrix} e^{i\beta_2}-1 & \delta_2 \\ e^{i\beta_3}-1 & \delta_3 \end{vmatrix}}{\begin{vmatrix} e^{i\beta_2}-1 & e^{i\alpha_2}-1 \\ e^{i\beta_3}-1 & e^{i\alpha_3}-1 \end{vmatrix}} \tag{3.4}$$

The right-hand dyad can be synthesized using the same $\delta_2, \delta_3, \alpha_2, \alpha_3$, together with

$$\beta_2 = \phi_{42} - \phi_{41}, and \quad \beta_3 = \phi_{43} - \phi_{41}.$$

An attached Maple worksheet (Appendix C) is provided to show the synthesis results. Note that, the configuration obtained from analytical synthesis can only be regarded as a workable model. To have optimum configuration, a series of simulation tests are needed.

2.2.2.2 Front Fork - Dimension of Linkage

Table 3.1: Results of the optimum link configuration. (r_1=0.06 m, r_2=0.12 m, r_3 =0.246 m, and r_4=0.14 m)

Part 1			Simulation results
Test No.	ϕ 1	***r3u***	**Maximum Height (m)**
T1	90	***0.065***	0.165
T2	90	***0.07***	0.180
T3	90	***0.073***	7.05 s for 0.20 m
T4	90	***0.074***	0.190 (Slippage occurred)
T5	90	***0.075***	Failed

Part 2			Simulation results
Test No.	ϕ 1	*r3u*	**0.2 m Obstacle**
T6	***95***	0.073	8.6 s
T7	***97.5***	0.073	9.75 s
T8	***100***	0.073	10.15 s
T9	***105***	0.073	11.85 s
T10	***110***	0.073	14.95 s

There are too many combinations for the front fork mechanism. To reduce the number of the tests, several assumptions have to be made. The objective is to determine the optimum configuration provides adequate climbing ability with minimum time consumed. Based on the configuration shown in Fig. 3.4, the two possible variations are the ϕ_1 and length of link r_{3u}, given that the length of links r_1, r_2, r_3, r_4, and wheel diameter are fixed. The results are shown in Table 3.1.

The first part of the test (T1 to T5) was varying the length of link r3u

while keeping ϕ_1 at 90 degrees. Result obtained shows link r_{3u} with length 0.073 m gives the best climbing ability, which is test T3. Test T4 failed as slippage occurred although it managed to climb up 0.19 m step. The test T5 failed since the impact force acting on the wheel is too large, which implies that link r3u cannot exceed 0.74 m for this combination.

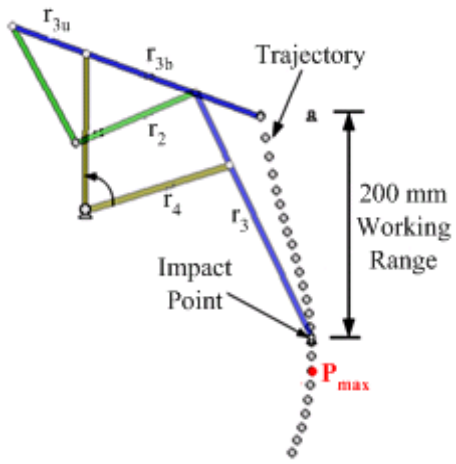

Figure 3.5: P_{max} test: The point P_{max} and working range.

In Part 2, all five combinations can overcome 0.2 m step while ϕ_1 increased from 95 to 110 degrees. Notice that, the duration is increased from 8.6 s to 14.95 s when the rover is running at 0.01 m/s. It implies that the configuration T6 is more efficient than the rest when the obstacle height is 0.2 m. Based on the results obtained in Parts 1 and 2, the first optimum front fork configuration is determined. However, it is still not the final model unless it passes the P_{max} test.

In Fig. 3.5, the trajectory of the front fork mechanism are shown using Interactive Physics. The working range of 200 mm is defined to match the objective of the project. The impact point, where the wheel hits on the vertical step, must be equal or above the point P_{max}, otherwise, the impact force acting on the front fork might damage the structure. The point P_{max} is defined as the maximum point along the path generated by front wheel. Also, the point P_{max}

must be located in lower region of the trajectory to have large working range, which defines the maximum obstacle height. The dimension configuration shown in the Fig. 3.6 is chosen since it satisfies all above mentioned conditions.

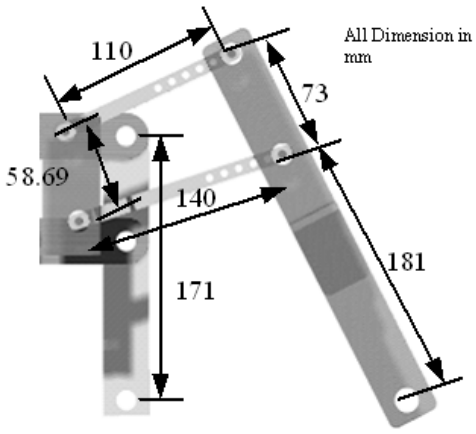

Figure 3.6: The selected front fork configuration.

2.2.2.3 Front Fork - Spring Constant

Spring is introduced to absorb the impact force that was exerted on the front fork upon impact. Two types of spring, tension spring and compression spring, are considered. Tension spring provides additional force to help to lift up the front fork. However, the compression spring will keep the front fork in contact with ground. Simulation interface in Fig. 3.3 was used to investigate the impact of spring types on front fork step climbing performance.

Three tests, front fork only, front fork with tension spring, and front fork with compression spring, were set up. During the first test, "fly-over effect", which the wheel is not in contact with ground for certain instant after climbing up the obstacle, was observed. It is obvious especially when the speed of the robot is increased. The effect is due to the lack of force to push the wheel to be in contact with the ground. Therefore, the author proceeded to use the compression spring in our design. The result shown in Fig. 3.7 once again reassured us the theory used in this design. Comparing all three cases, only

compression spring is able to keep optimum and continuous contact between wheel and terrain while climbing obstacle.

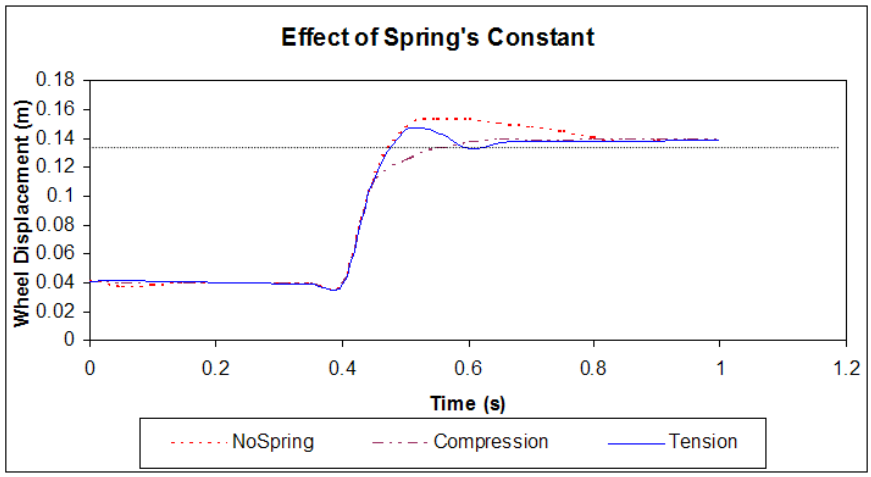

Figure 3.7: The effect of spring constants on wheel trajectory.

2.2.2.4 Front Fork - Spring Configuration

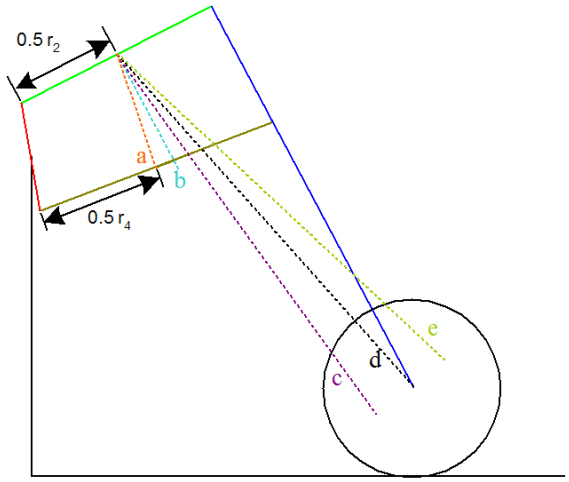

Figure 3.8: Five possible spring's location.

Based on previous results, the compression spring is selected to ensure continuous contact, which is crucial for ODR to perform well. The next task is to investigate the relationships between the spring location and front fork climbing performance. Five possible configurations were considered,

(a) Attached to the center of links r_2 and r_4;

(b) Parallel to the link r_3;

(c) Below of the center of front fork's wheel;

(d) Aligned with the center of front fork's wheel;

(e) Above of the center of front fork's wheel, as shown in Fig. 3.8.

The objective is to investigate possible maximum impact force on the wheel, when the front fork is tasked to move toward obstacle in 0.27 m/s. The spring constant is 350 N/m and the initial length is 0.06 m. Also, the trajectories of wheel are compared to find the optimal spring configuration, which insure a good stability while climbing obstacle. The results of all simulations are plotted and shown in Fig. 3.9 and 3.10. The reference configuration here is the front fork without spring. The results in Fig. 3.10 show that the locations **c**,

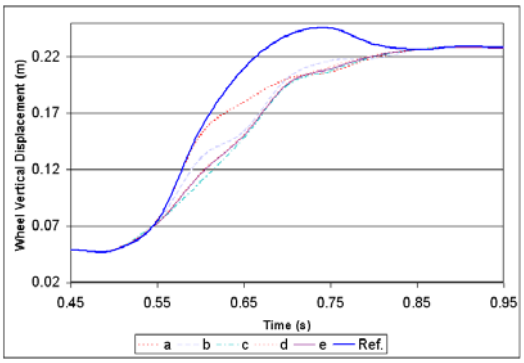

Figure 3.9: The effect of spring locations on wheel trajectory.

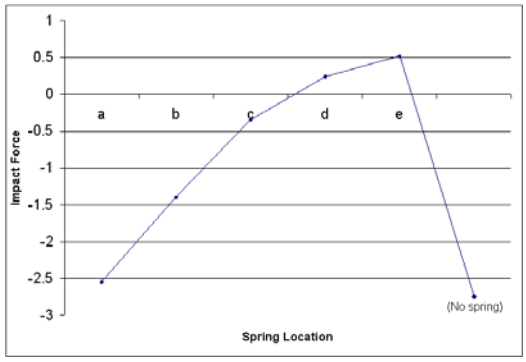

Figure 3.10: The effect of spring locations on impact force.

d, and **e** produce the best trajectories without "fly-over effect". However, the results of the impact force experienced by the wheel upon impact are different. Locations **c** and **d** produces the best impact absorption ability among all configurations. In conclusion, the front fork with compression spring in location **c** or **d** shows the best step climbing performance. The effect of compressed spring on the bogies wheels' step and stair climbing ability will be investigated in next chapter.

Chapter 4

Simulation and Mobility Analysis of ODR

4.1 3D Simulation - Mobility Analysis

In this chapter the dynamic behaviors of the omni-directional rover (ODR) are considered. The analysis of the simulation findings shall only focus on highlighting a few critical area of discussion due to vast amount of data recorded. In the simulations, the author aims

- To evaluate the performance of the optimum front fork configuration;
- To determine the effect of spring rate;
- To identify the possible sources of failure;
- To determine the maximum impact force while front fork hitting on the vertical step;
- To determine the maximum output torque for actuator selection.

In 3D simulation, the mobility analysis started by driving the ODR on structured terrain, as shown in Fig. 4.1. The ODR is tested on three different types of terrain, namely, step, staircase, and slope. Three runs were conducted as follows:

- **Run I**: Spring rate : 5400 N/m, ODR speed: 0.1625 m/s

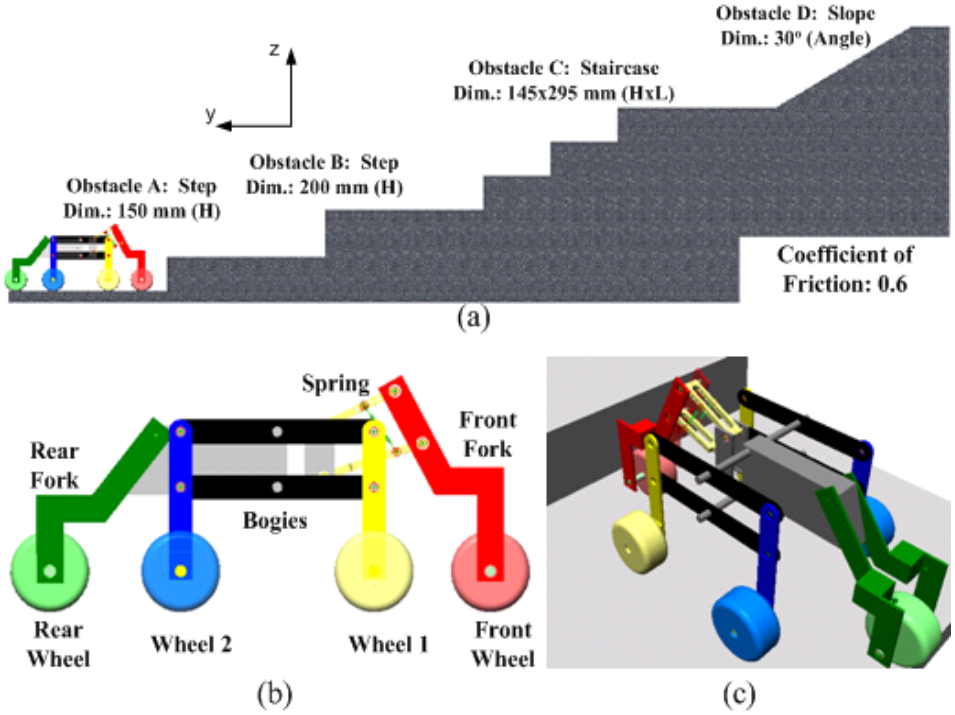

Figure 4.1: The obstacle tests configuration: (a) Dimension of structured terrain; (b) Notation of ODR; (c) ISO view of 3D-model.

- **Run II**: Spring rate: 10000 N/m, ODR speed: 0.1625 m/s
- **Run II**: Spring rate: 10000 N/m, ODR speed: 0.1 m/s

4.1.1 Description of Simulation Setup

By developing the 3D ODR for motion analysis, the author aims to investigate the quantitative relationships among the performance parameters. Based on the input parameters, like speed, weight, spring rate, and traction, the impacts of the "environment" and "mission" on the rover locomotion are reflected by both the text data and graph.

The core program used in this project is MSC. visualNastran 4D [51]. The MSC. visualNastran 4D is designed for the construction of the simulation platform that eventually integrates motion and stress simulation into one functional model. In order to have more accurate results, users can directly import assembled CAD model from a variety of latest CAD software. The list

of compatible software includes the author preferred Solidwork.

Within the window environment, the program continuously computes and shows the analyzed data in the form of graphical output. By creating the graphs and motion with numerical values obtained from the integrated simulation engine, the user is capable of reinforcing the observation by exporting the numerical and graphical data into Excel and movie files.

Three main performance parameters will be carefully investigated with a series of simulated scenarios, namely *trafficability*, *maneuverability*, and *terrainability* [53].

- Trafficability, which is a rover's ability to traverse on undulating terrain without loss of traction.
- Maneuverability, which addresses a robot's ability to navigate through an environment.
- Terrainability, which captures a rover's ability to negotiate terrain irregularities.

The approach of this analysis towards the mobility capabilities of the rover locomotion starts from analyzing the results and observation obtained from the front fork overcoming step obstacle discussed in previous chapter, followed by the motion analysis of 3D ODR overcoming various types of obstacle.

4.1.2 Parameter Settings

Before running the simulation test, a fine-tuning of 3D CAD model is needed to have faster and accurate results. First, the large number of rigid joints that consist of mainly nuts and bolts were taken out from the 3D CAD model in an attempt to reduce the number of constraints. The re-modeling was done by merging the rigid-jointed components into one. Instead of the omni-

Table 4.1: List of components weight.

No.	Name of Components	Weight	No of items	Total Weight
01	Middle Body	3.00	1	3.00
02	Front Wheel Structure	0.10	2	0.20
03	Rear Wheel Structure	0.10	2	0.20
04	Horizontal Bogie Bar	0.10	4	0.40
05	Vertical Bogie Bar	0.10	4	0.40
06	Front Fork C	0.05	1	0.05
07	Front Fork E	0.05	1	0.05
08	Bogie Wheel	0.60	4	2.40
09	Front Wheel	0.70	1	0.70
10	Rear Wheel	0.70	1	0.70
11	Shaft	0.08	6	0.48
			ODR Total weight	8.58
				All weight in kilograms

directional wheels, the cylindrical wheels were used to ensure a more accurate measurement of the contact forces between the wheel and ground.

The simulation test was carried out with an intention to match the realistic weight configuration of the ODR prototype. The respective weight settings for each of the components can be found in Table 4.1 with a pictorial diagram representing the individual components attached in Appendix B for clearer references.

As shown in Table 4.1, the components that have the most significant effect on the weight distribution of the ODR are wheels and the middle body of the model. The weight of the middle body is about 3 kg considering the weight of the lithium-ion rechargeable battery, motion controller card, and the single board computer required to drive the ODR. The front and the rear wheel are slightly heavier than the rest of the bogie wheels due to different mechanical drives.

As mentioned, the CoG of the entire ODR shall play an important role in contributing to the stability of the system when it is climbing obstacles. Therefore, it is necessary to determine the position of the ODR's CoG in terms

of the global coordinates. However, the MSC. visualNastran only provides the CoG of individual components in terms of local coordinates instead of giving the overall CoG of ODR in terms of global coordinates. Therefore, coordinate transformation is needed to determine the CoG of individual components in global coordinates before computing the overall CoG.

Applying the concept of point-to-point mapping, a vector transformation rotational matrix, $\boldsymbol{R}$, sub-divides the mapping process into three frame rotational matrices defined by

Rotation about axis X by angle, α:

$$\mathbf{R}_x(\alpha) = \begin{bmatrix} 1 & 0 & 0 \\ 0 & \cos\alpha & -\sin\alpha \\ 0 & \sin\alpha & \cos\alpha \end{bmatrix} \tag{4.1}$$

Rotation about axis Y by angle, γ:

$$\mathbf{R}_y(\gamma) = \begin{bmatrix} \cos\gamma & 0 & -\sin\gamma \\ 0 & 1 & 0 \\ \sin\gamma & 0 & \cos\gamma \end{bmatrix} \tag{4.2}$$

Rotation about axis Z by angle, θ:

$$\mathbf{R}_z(\theta) = \begin{bmatrix} \cos\theta & -\sin\theta & 0 \\ \sin\theta & \cos\theta & 0 \\ 0 & 0 & 1 \end{bmatrix} \tag{4.3}$$

The subscripts G denotes the global reference frame, and L denotes a reference frame that is embedded in a rigid component. Let P be a point at the CoG of the component and let

$$r_L = \begin{bmatrix} x_L & y_L & z_L \end{bmatrix}^{\mathrm{T}} \tag{4.4}$$

be the position vector of P relatives to local frame; let

$$c_G = \begin{bmatrix} x_G & y_G & z_G \end{bmatrix}^{\mathrm{T}} \tag{4.5}$$

be the position vector of the origin of local frame relatives to global frame. Therefore, the position vector of P relatives to global frame is

$$r_G = \begin{bmatrix} x_G & y_G & z_G \end{bmatrix}^{\mathrm{T}} = \mathbf{R}_x(\alpha)\mathbf{R}_y(\gamma)\mathbf{R}_z(\theta)r_L + c_G \tag{4.6}$$

Understanding the application involved belongs to a three dimensional problem, the CoG of ODR is determined by expressing that the moment about global frame's origin of its total weight is equal to the sum of the moments about global frame's origin of the weight of the various component parts. Therefore, the position vector of overall CoG relatives to global frame is

$$\begin{bmatrix} X_G \\ Y_G \\ Z_G \end{bmatrix} = \begin{bmatrix} \frac{\Sigma x_G W}{\Sigma W} \\ \frac{\Sigma y_G W}{\Sigma W} \\ \frac{\Sigma z_G W}{\Sigma W} \end{bmatrix} \tag{4.7}$$

where W denotes the weight of the individual components.

An attached Excel worksheet (Appendix B) is provided to illustrate the usage of the positional mapping and shows the final calculated CoG of the ODR. As mentioned, the ideal range of position for the overall C.G of the ODR should be located between the bogie wheels and maintain as close as possible to the front fork and ground level. In view of this piece of information, the CoG of the middle body for the MSC.visualNastran model was shifted strategically closer to the parallel center of the horizontal bogie bar.

Another important feature is the 3D models created in CAD programs can be used in MSC.visualNastran environment. It imports CAD modeling solids by means of utilizing the ACIS Converter that represent the bodies in the

form of polyhedron (a solid bounded only with polygons) [51]. In designating features that has non-linear planar surfaces, an approximation method known as *faceting* is used. This involves the tessellating of curvature surfaces into a set of polygons that is governed by the surface deviation and the normal deviation parameters. The surface deviation specifies the maximum distance between a facet and the true surface as a ratio compared to the size of the model. The normal deviation is responsible for the maximum deviation (in degrees) allowed between the normal vectors of any two adjacent facets. In general, increase the number of facets will provide a more accurate result since it affects the smoothness of the object's edge. As a benchmark, the entire CAD assemblies in the simulation use solids that have a zero surface deviation concurrently with one degree of normal deviation as the parameter setting for the contact surface.

Once the initial parameters are set, the individual motor driving each of the wheels were simulated to run at low speed and the simulation was allow to commence until the time when the last wheel climb up the step obstacle. The coefficient of friction was set at 0.5 to simulate terrain likely to be experienced by the ODR. From our simulation analysis, the ODR is able to overcome a step height of 200 mm, which is about two times its wheel diameter, based on the optimum geometry configuration and the results are discussed and analysed in the subsequent sections.

4.1.3 Single Step Climbing Ability - Obstacles A & B

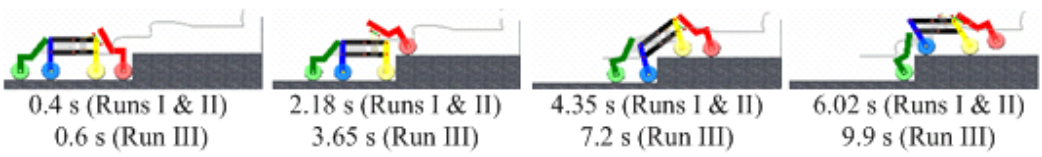

Figure 4.2: Climbing sequence for Obstacles A (H:145 mm) and B (H:200 mm)

The step obstacles, refers to Obstacles A and B depicted in Fig. 4.1, were selected primarily due to its consideration as one of the tougher obstacle that may obstruct the motion of the ODR. At a 90^o inclination to the ground surface, achieving success in overcoming the step obstacle will give us a reasons to believe that the majority of the protruding uneven terrain will not pose too much problem to the ODR. Therefore, the purpose of conducting this simulation is to validate the ODR's step climbing ability based on the optimum front fork configuration, as depicted in Fig. 3.6. Obstacle B is used to test the maximum step climbing ability of the ODR. It shows that the ODR is able to climb up step height about two times its wheel diameter.

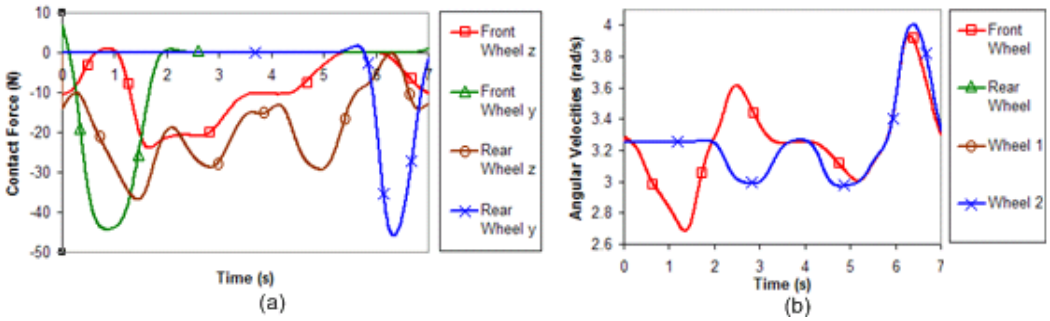

Figure 4.3: Single step analysis diagrams of Run I: (a) Front wheel contact force; (b) Angular velocities.

Climbing sequence and registered time of the different Runs, as shown in Fig. 4.2, are used as reference in the following discussion. At simulation time 0.4 s, the front wheel of the ODR contacts the step obstacle and registered a high amount of contact force, 45 N, displayed in Fig. 4.3(a). Also, the angular velocity of front wheel is reduced gradually due the above contact force. However, the rest of the wheels maintain their speed and provide adequate forces to allow the front wheel steadily climb up the step, as showed in Fig. 4.3(b). At the same time, the front wheel also registered highest output torque since the driving torque is directly proportional to the contact force, as shown in Fig. 4.4(a).

As the front wheel progressively moves upward, there will be a change of contact force at simulation time one second from the negative Y direction to the Z direction, as depicted in Fig. 4.3(a). It shows that the front wheel has crossed the step with more that half of the wheel diameter. At this point in time, the front fork is under high compressive force due to the change of the spring length. The attempt by the spring mechanism to release the compressive load will trigger an upward lifting force sufficient enough to lift the bogie wheel 1 off the ground when there are in contact with the vertical step. During the climbing process, the CoG of the ODR also is lifted concurrently.

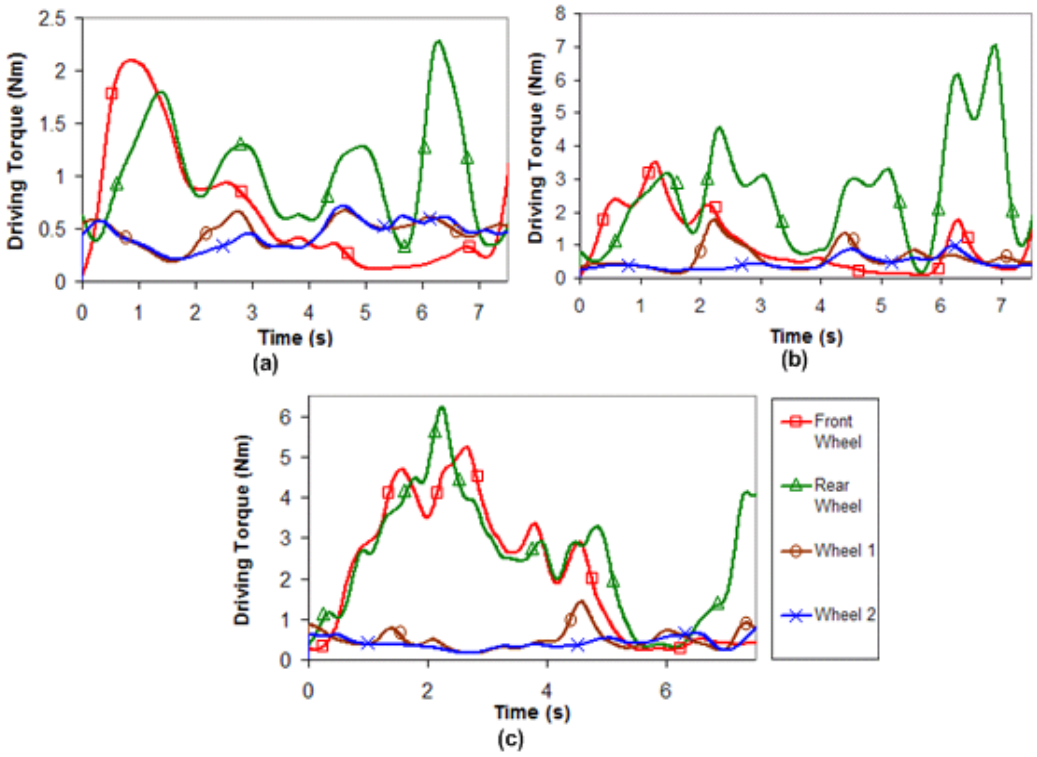

Figure 4.4: Torque diagrams of single step climbing analysis : (a) Run I; (b) Run II; and (c) Run III.

By now, at simulation time 4.35 s (see Fig. 4.2), the first three wheels of the ODR have reached the top of the step, leaving the last set of bogie wheels to alliance with the rear wheels to push the CoG of the ODR above the step. The moment bogie wheel 2 are lifted off the ground, the rear wheel

has to provide a forward force or driving torque sufficient enough to maintain the present motion together with the wheels on top of the step. It explains the significant increment in torque readings from 4 to 6 seconds, as shown in Fig. 4.4. As the motion continues, the rear wheel could be seen once again critically overcoming the large contact forces, 45 N, to push itself up the step obstacle, as shown in Fig. 4.3 (b).

At the same time, the simulation also registered sharp increases in angular velocities at time 6.02 s, which implies that all the wheels experience traction failure. However, the rear wheel still able to maintain a contact force in negative Y direction which enables the last wheel to climb up. In addition, it can be noted that the front wheel is lifted up in the air at 6.02 s in **Run I**. A good explanation could be the front fork assembly has reached the configuration limited by the spring assembly before falling into the stage of singularity.

4.1.4 Multiple Steps Climbing Ability - Obstacle C

To extend the covering range of the robot in the urban environment, the functionality of traveling over multiple steps, also conventionally termed as staircase, is equally important to our analysis. Contrary to what was perceived as an insignificant study, the results show a new dimension of analysis that was not possibly foreseeable with the single step findings. What was previously established as a successful operating ODR may not be capable of even climbing up the very first step of the staircase. As a rule of thumb, a complete staircase climb would require the ODR to at least overcome three multiple steps to provide a strong evidence for validating the success was not an occurrence of riding up the stairs by sheer momentum. Therefore, this section of the report aims at deducing the major geometry constraints faced by the ODR that shall enable it to climb up the staircase.

Climbing sequence and registered time of **Runs I** and **II**, as shown in

Fig. 4.9, are used as reference in the following discussion. The results obtained for the stair possess certain similarity to those recorded for the single step obstacle until 18.93 s for **Run I**, and **II**, or 31.25 s for **Run III**. Therefore, the discussion will only focus on the later section. At 18.93 s in **Run I**,

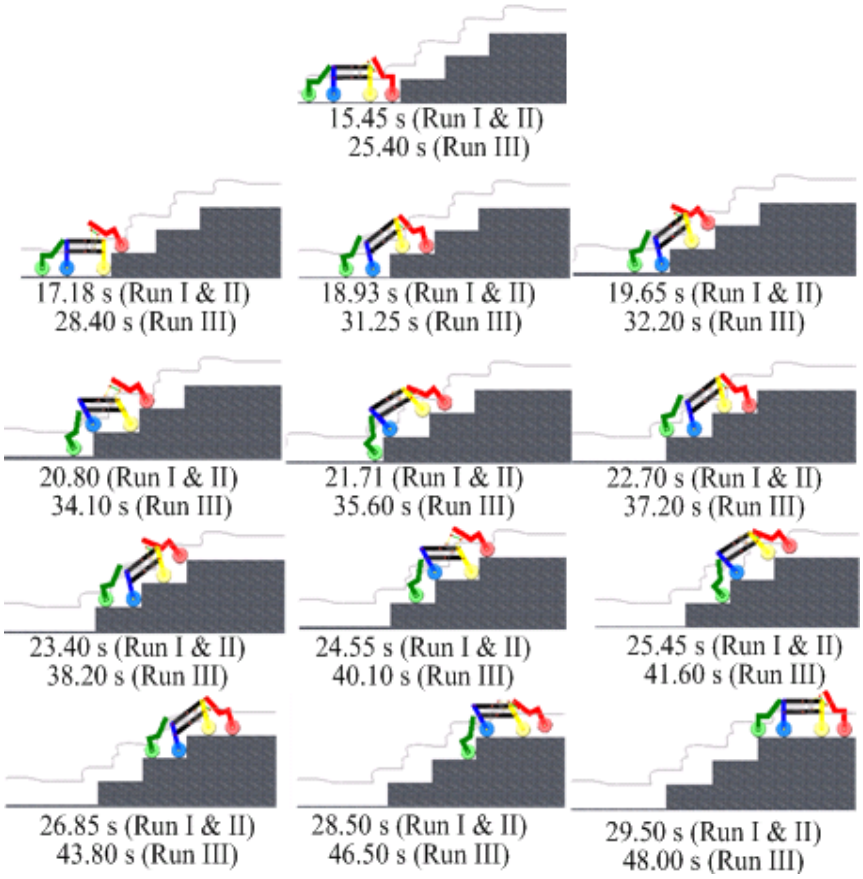

Figure 4.5: Climbing sequence for Obstacles C (H×L:145×295 mm)

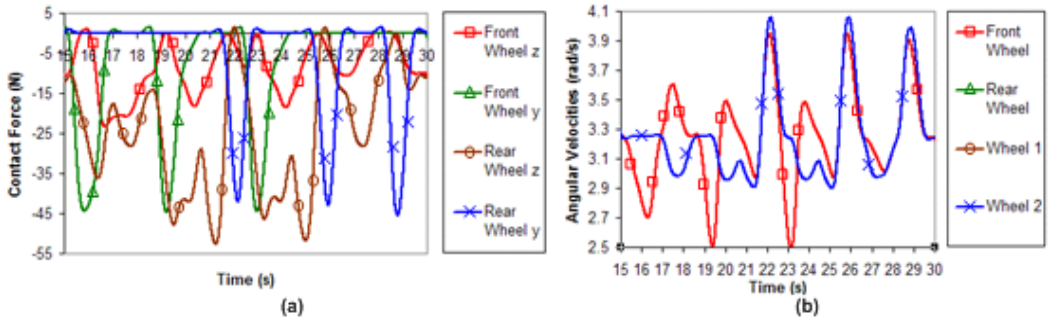

Figure 4.6: Multiple-steps analysis diagrams of Run I: (a) Front wheel and rear wheel contact force; (b) Angular velocities.

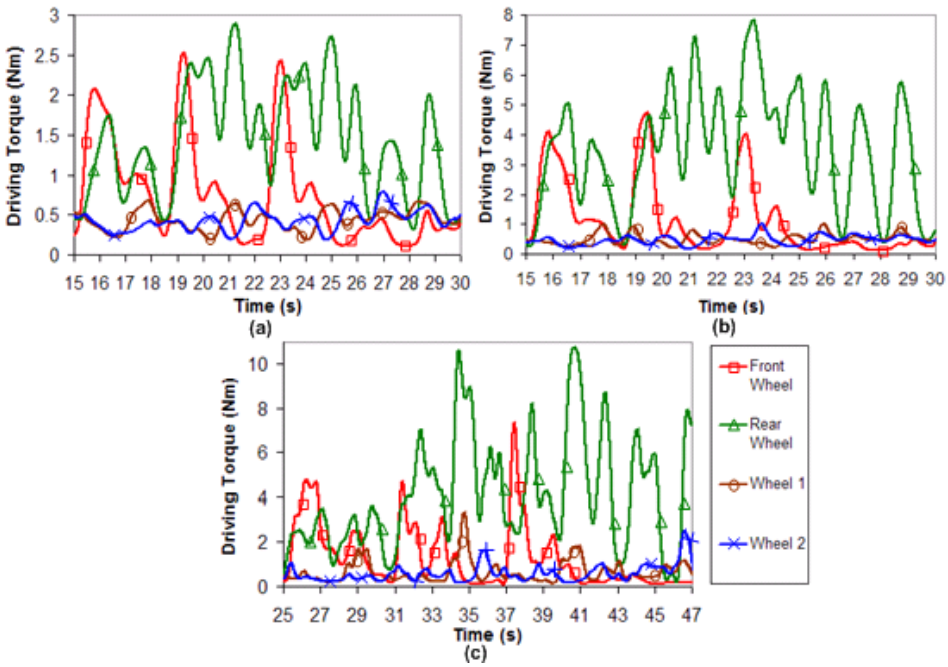

Figure 4.7: Torque diagrams of multiple-steps climbing analysis: (a) Run I; (b) Run II; and (c) Run III.

the expected large contact force in negative Y direction is registered on front wheel, as depicted in Fig. 4.6 (a). Compared with the time at 15.45 s, the rear wheel is subjected to much higher contact force in negative Z direction. It is because the spring mechanism is under compression at a value of 5.08 N. However, the front wheel still manages to move up the second step until the wheel 2 experiences two points contact with first step at 19.65 s.

Initially, the majority of the ODR models fail to proceed forward beyond this point. After studied the torque diagrams of the failed models, the rear wheel registered extremely high torque values compared to the rest of the wheels. It also implies that the ODR is not able to climb up multiple steps with front wheel and wheel 2 climbing upward simultaneously. To alleviate this problem, the geometry dimensions of the ODR is modified such that *only one wheel is moving upward at any instance*. The first geometry constraint based on above criterion is determined at simulation time 20.8 s, where the wheel 1 is having two point contacts with second step,

$$l_{Bogie} + r_{\mathrm{w}} \leq \text{Stair Width}$$

Another critical moment is at simulation time 21.7 s, the rear wheel hits the first step while the wheel 1 is about overcoming the second step. It is even worsen than previous scene as the front wheel is lifting in the air, and wheel 2 becomes the only propelling force. Based on the above criterion, the wheel 1 needs to cross the second step more than half wheel diameter before the rear wheel establishes two point contacts with first step. As a result, the wheel 1 and 2 will work together to propel the ODR moves forward.

Based on the above observations, the relationships between the stair and ODR geometry dimensions can be determined. The selected length of bogie, l_{Bogies}, and length of rear fork, l_{Rear}, must satisfy the two constraints listed in Fig. 4.8 in order to avoid possible failure during the stair climbing.

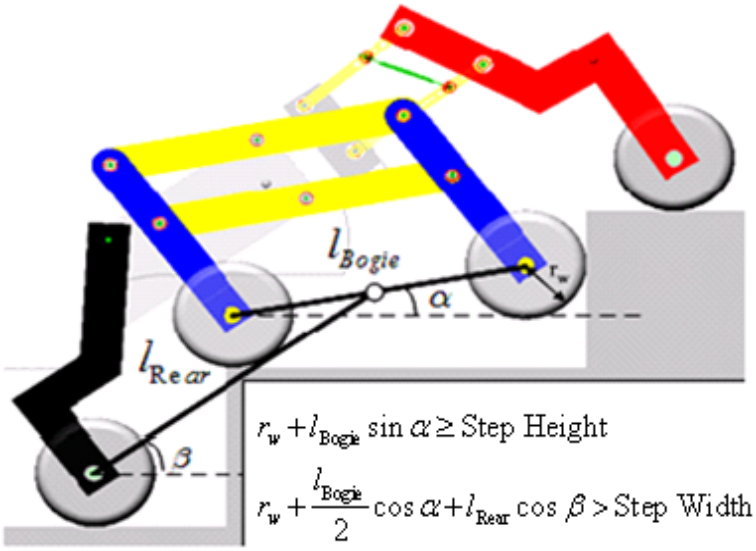

Figure 4.8: The stair climbing constraints.

Fig. 4.7 shows the recorded wheels driving torque in the Runs I, II, and III. The results obtained from three tests indicate that the rear wheel could register highest driving torque among the wheels. This may be due to the absence of driving force from front wheel when it is unable to get a horizontal foothold. Comparing the Runs I and II, the higher spring rate does not help

much to the ODR's stair climbing ability. Indeed, it creates extra problem by requiring higher torque output. However, ODR without spring mechanism can only climb up the stair with coefficient of 0.8. A miniature simulation study of the influence of the spring force to weight ratio on ODR step climbing ability reveals that the minimum spring force to weight ratio was found to be approximately 58 percents before any lifting of the bogie wheels is possible. Therefore, the two springs with spring rate 2700 N/m are selected to enhance the ODR step and stair climbing ability.

4.1.5 Slope Climbing Ability - Obstacle D

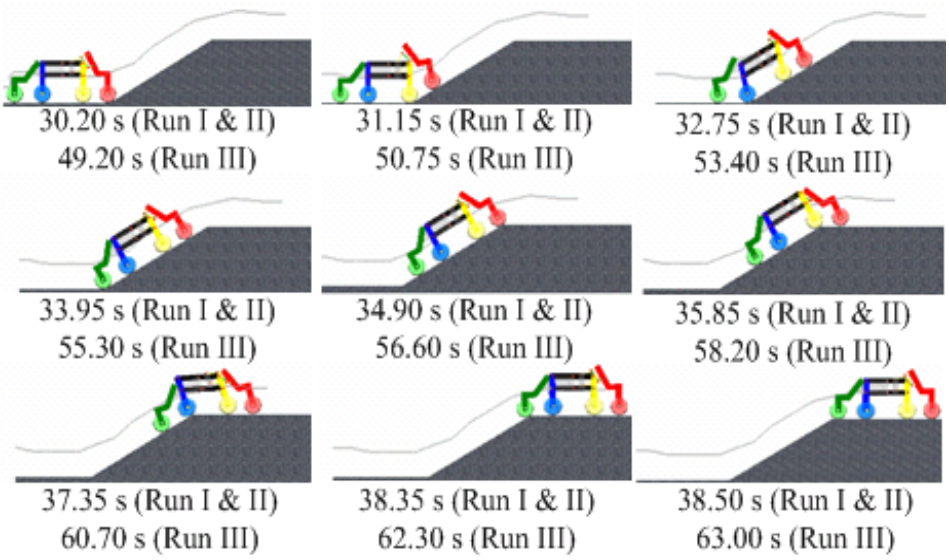

Figure 4.9: Climbing sequence for Obstacles C (Slope angle: 30°)

As one of the most commonly anticipated protruding contours, slope is included in the mobility analysis. In fact, a series of tests was carefully conducted with an objective to first determine the maximum slope that the ODR is able to negotiate before any form of data collection is carried out. By means of a progressive increment of 10°, which reduces to a mere 5° difference when a specific range was obtained, the maximum slope that the ODR was capable of overcoming peaks at 30°. Also, the length of the slope is longer than the

overall length of the ODR. This will ensure at a certain period of time, the entire ODR has to transverse entirely on the slope which will reduce the possibility of erroneous simulation results. The results of the 30° slope test were tabulated and will be discussed in the subsequent sections.

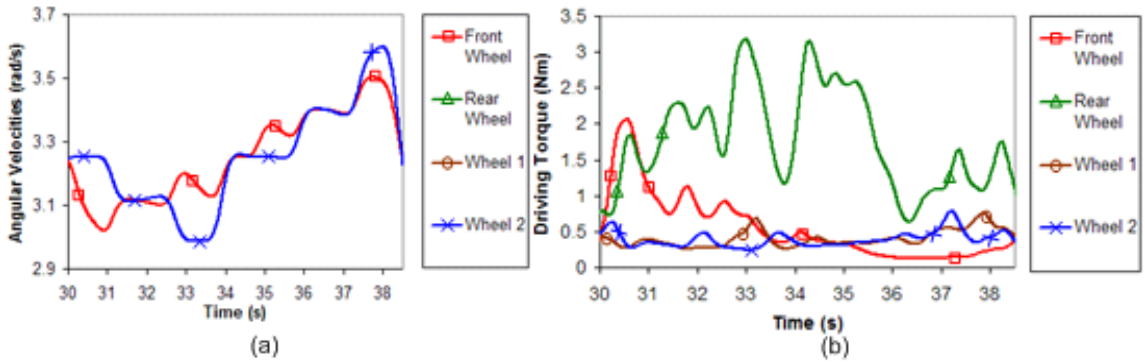

Figure 4.10: Slope analysis diagrams of Run II: (a) Angular Velocities Diagram; (b) Driving Torque Diagram.

From simulation time 30 to 33.95 s, the ODR is experienced speed reduction from 3.25 rad/s to 3 rad/s, as shown in Fig. 4.10 (a). In the same time, the torque output increased significantly. These results may be explained by the Newton's third law that the applied force from the wheels acting in the direction up the slope must balance the forces down the slope resisting that force. These resisting forces are the friction force and portion of the ODR weight. As a result, the motors need to increase the torque output to balance the additional force component due to weight, as depicted in Fig. 4.10 (b).

After the rear wheel passed the base of the slope at simulation time 33.95 s, the angular velocities increased to 3.6 rad/s, and dropped back to 3.25 rad/s when the ODR is on top of the slope. The results seem that ODR is having difficulty to maintain traction when it is on the slope although the ODR is still climbed up the designed slope.

4.1.6 Remarks

Another area of study was the singularity problem faced by the ODR. The first few models of the simulated ODR do not process any form of length control to restrict the front fork from over extension. It resulted in the front fork assembly reaching the singularity state where link r_2 touches link r_4 and is unable to return back to its initial position. Through numerous test and analysis, the optimum distance the front fork assembly is allow to stretch forward should be set at a maximum value of an additional 20 % to the initial length. To implement this in real prototype, it will come in a simple arrangement of a rod within the springs with a locknuts at one end to prevent any further forward extension of the front fork assembly.

4.1.7 Summary

The functional capabilities of the ODR were thoroughly analysed in this chapter through the modeling within the MSC. visualNastran environment. By subjecting the ODR to situational tests that determine the trafficability and terrainability of the simulated model, detailed and conclusive observation was obtained. As the task of improving the ODR becomes more complex in the near future, the knowledge gained from running these tests will prove to be invaluable and necessary in preparing more realistic platform for further analysis.

Chapter 5

Design and Development of ODR

5.1 Introduction

In order to build a teleoperated omni-directional rover, some constraints have to be taken into consideration like the space on the mobile robot for components like the motion controller, actuators, sensors and batteries. Besides, the robot is required to perform several planned motions and navigation in teleoperated mode by using the single board computer as a microcontroller. A new robot has to be constructed from scratch and a set of design specifications is proposed. In this chapter, the mechanical design of ODR is outlined; furthermore, redesigned ODW is introduced to minimize slippage problems.

5.2 Design Specifications

The ODR, a wheeled vehicle with ability to navigate on undulating terrain, is designed, developed and fabricated according to the following design specification:

- 6-wheel shrimp spring suspension system
- Omni-directional wheel; zero turning radius and no steering is required

- Wheel size: 10 cm diam, 5 cm width
- Rover top speed: 0.2 m/s
- Wheel torque: nominally 1 Nm for driving on flat terrain; stall torque is 6 Nm
- Maximum obstacle size: 15 cm based on mobility system alone.
- Harzard avoidance will limit clearances to 5 cm rocks
- Wheel actuators have encoders

5.3 Redesigned Omni Directional Wheel Development

5.3.1 Overview of ODW Design

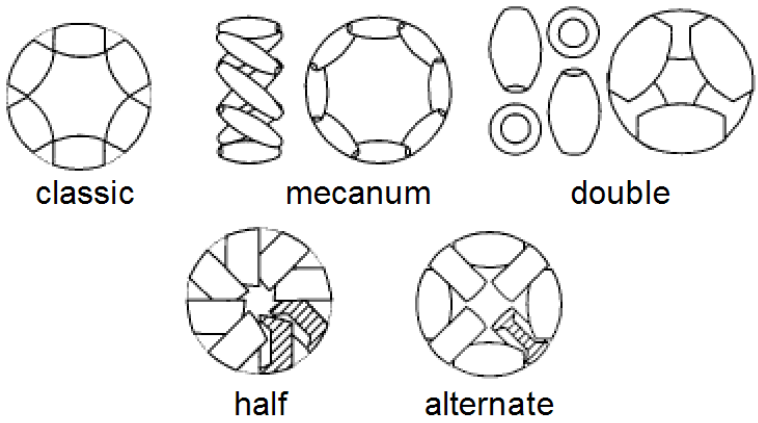

Figure 5.1: Various wheel designs with passive roller mechanism [55].

Conventional wheels are mechanically simple, high load capacity, and easier to control. However, due to their non-holonomic characteristic, various designs have been proposed and tested to achieve omni-directional motion without having time delay. One of the solution is ODW. The working principle of Mecanum wheel is discussed in Section 1.4.3.

In general, ODWs are more complex and difficult to fabricate when compared to conventional wheels; moreover, WMRs built around such wheels have lower load carrying capacity and their surmountable bump height depends on the roller diameter rather than on the wheel diameter. However, what these robots lacks in load-carrying capacity and surmountable bump height, they make up with fluent manoeuvrability and no singularities.

Various variations of ODW have been designed and prototyped [55], as shown in Fig. 5.1. The first one is *classic mechanism* where a series of passive rollers whose axes are arranged tangent to the the wheel circumference. The major drawback of such design is the gap between the rollers, which will generate discontinuous footprint and severe vertical vibration problems.

Two alternative solutions are provided to minimize the gap. The first one is *Mecanum wheel*, where the rollers are mounted at an angle to the wheel plane of rotation. The second is the double wheel mechanism, the rollers are arranged in overlapping manner. Both designs are able to produce continuous foot print with minimum vertical vibration, but the contact point between wheel and terrain for double wheel is not straight line. This results poor performance on smooth terrain due to horizontal vibration.

In order to further minimize the gap and to reduce the vertical and horizontal vibrations, two alternative wheel mechanisms, known as *alternate* and *half wheel mechanism*, are proposed [55]. The alternate wheel mechanism used large and small rollers, which are configured alternatively as shown in Fig. 5.1. The half divided rollers are used in half wheel mechanism to solve the problems, however the gap can not be eliminated completely. The major disadvantages of both designs are complicated mechanism, and possible high manufacturing cost, considering the tolerance needed.

Figure 5.2: Interoll omni-directional conveyor wheel [56].

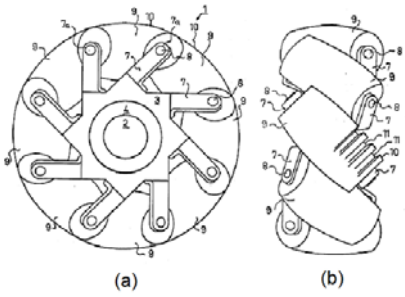

Figure 5.3: Mecanum wheel based on Ilon's design [32].

5.3.2 The 3-Wheel OWMR with Redesigned ODW

The current available ODW in the local market is the Omni-Directional Conveyor Wheel [56] from *Interoll*. The Interoll's wheel used double wheel mechanism with the passive elliptical rollers held in place from outside as depicted in Fig. 5.2, which is similar to Ilon's design [32], as shown in Fig. 5.3. One major drawback of such design is the wheel may not perform correctly when the vehicle operates on non-hard terrains, as the wheel will sink into the surface and the rims of the wheel contact with the ground surface, which stops the roller movements. As a result, the gear boxes in the actuator may be destroyed when subjected to unexpected high torque.

In addition, the wheels are made of polyamide, which is not giving enough traction to prevent wheel slippage. If slipping occurs, the robot will not able to position itself if no other position means provided. It is because the maximum acceleration of the wheel and the minimum stopping distance of the wheel is limited by the the friction between the wheel and the terrain.

Another drawback is the performance of the robot is determined by the roller starting position, as the roller is freely moved along the axle. In this case, the wheel hub becomes one of the significant factors in slip dynamic analysis [58]. For instance, the ODW's starting position shown in Fig. 5.4 (a). The reaction force due to the vehicle weight will pushed roller to close

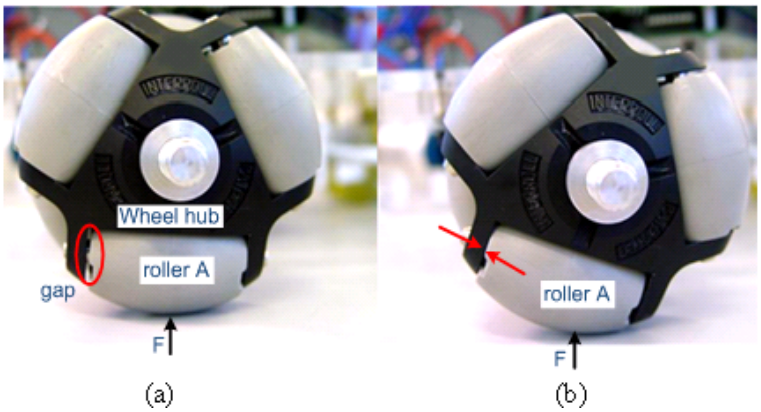

Figure 5.4: Positions of roller. (a) In idle position; (b) In contact with wheel hub.

the gap with the wheel hub, as depicted in Fig. 5.4 (b). As the result, the actuator required to overcome the extra friction between roller and the hub. The performance of robot is degraded as the roller's location is unpredictable.

To alleviate the above problems, alternative wheel hub design is proposed, as shown in Figs. 5.5 and 5.7. The rollers split in two and centrally mounted as shown in Figs. 5.6 and 5.8. In the new design, the roller is restricted to move horizontally as the shaft is fixed by setscrews. Also, the roller material is changed from polyamide to polyurethane. Two types of ODWs, double and *Mecanum* whee mechanism, with new design are fabricated, as shown in Fig. 5.9.

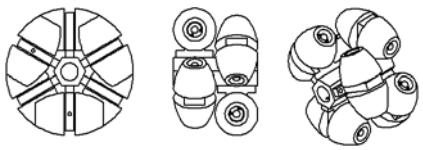

Figure 5.5: Redesigned ODW.

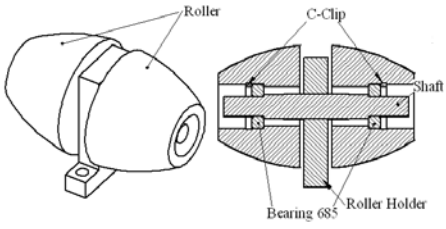

Figure 5.6: The sectional view of redesigned ODW's roller.

Figure 5.7: Redesigned *Mecanum* wheel.

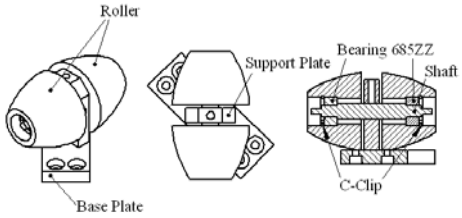

Figure 5.8: The sectional view of redesigned *Mecanum* wheel's roller.

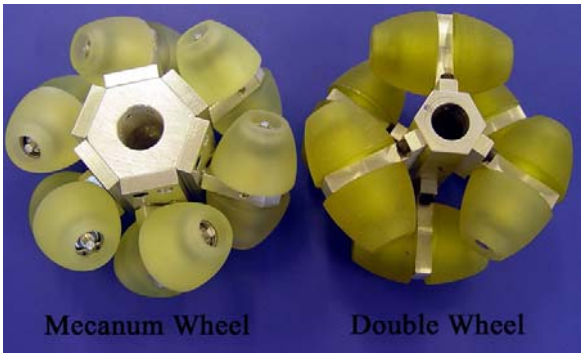

Figure 5.9: The picture of redesigned ODWs.

5.3.3 Experimental Setup

Within the scope of this thesis, we focus here on the design and testing of WMR with three Interoll ODWs and redesigned ODWs. A tele-operated three-wheel WMRs, Omni-directional Wheeled Mobile Robot II (OWMR II) with ODWs is designed and prototyped to test the redesigned ODW, as shown in Fig. 5.10. OWMR II was conceived as a mechanical and control system upgrade of the simple robot OWMR I, as shown in Fig. 5.11. The details of two system are listed in Table 5.1. The hope of this new OWMR was to create a more mobile vehicle, which is larger in size and higher in payload.

A major improvement from the first to the second prototype was the use of micro-controller board, *Handyboard* [61], and rechargeable battery. The work space of the robot is enlarged by eliminating the wires tagging between the robot and the power supply. In order to eliminate the backlash experienced in OWMR I [59], the miter gear drive is replaced with direct drive. With the use of these new system, the author is able to test the redesigned ODW on

different terrains. And, the results will be plotted and discussed later.

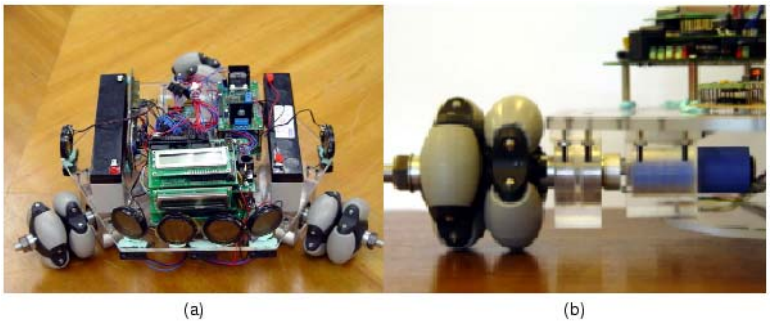

Figure 5.10: (a) Three wheel OWMR II; (b) OWMR II main mechanical drive.

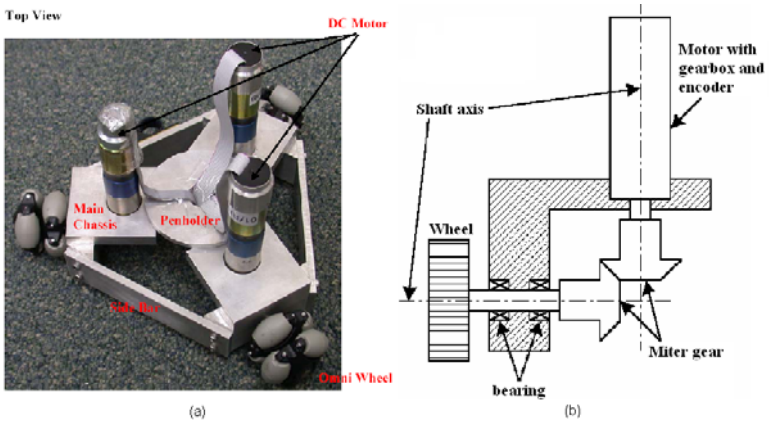

Figure 5.11: (a) Three wheel OWMR I; (b) OWMR I main mechanical drive.

5.3.4 Testing of the WMR with Three ODWs

The kinematics of a WMR with three omni-directional wheels was discussed in [35, 36, 59]. A series of tests was conducted to determine the positioning repeatability of the Interoll ODWs and redesigned ODWs. The OWMR II is tested in its performance to move to three main directions, North, East and North-East, as depicted in Fig. 5.12. First, the mobile robot is equipped with the Interoll ODWs that is made of polyamide, and it is tasked to move to three main directions using conventional trapezoidal velocity profile.

The actual outputs refer to the start and end positions for $T_m = 3$ s over a distance of 100 mm on flat ground, are measured, recorded and tabulated.

Table 5.1: Comparison of OWMR I and OWMR II.

	OWMR I	OWMR II
Physical		
Mass	1.5 kg	5 kg
Power Consumption	36 W max.	80 W max.
Platform Diameter	26 cm	150 cm
Locomotion	Miter Gear	Direct Drive
Wheel Diameter	4 cm	8 cm
Speed	0.22 m/s Maximum	0.5 m/s Maximum
	0.1 m/s Average	0.25 m/s Average
Computing		
Host Terminal	Pentium II 300 MHz	NIL
Controller	Pic-Servo Motion Controoler	Handyboard(2 MHz)
Teoperation	NIL	Yes(IR-Remote)
Autonomous	NIL	Yes

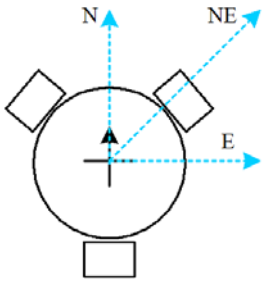

Figure 5.12: Directions used during traction test.

20 records were made for each direction. After that, the test is repeated with redesigned ODWs that made of polyurethane. The error is calculated from the differences between the commanded output and the actual output. The aims of the test is to investigate the improvement of traction of the wheel, in this case the polyurethane material and new hub design.

5.3.5 Results

The effect of different types of ODWs on the positioning behaviour of a OWMR was investigated. A comparison test has been carried out. To study the exact improvement, variances of the results are tabulated and compared in Table 5.2. Given that the variance is one of several indices of variability that engineers and researcher use to characterize the dispersion among the measures in a given

population. To calculate the variance of a given population, it is necessary to first calculate the mean of the errors, then measure the amount that each error deviates from the mean and then square that deviation (by multiplying it by itself). Numerically, the variance equals the average of the several squared deviations from the mean. It can be clearly seen that the errors arose from the polyamide material and previous hub design are improved significantly as shown in Table 5.2. The mobile robot also showed the ability to move on ceramic and road surface, which previously cannot be done.

Table 5.2: Comparison of variances before and after using the redesigned ODWs.

Direction	Variance (Interoll ODWs)	Variance (Redesigned ODWs)	Percentage
East	1.38	1.14	17.4
North-East	1.77	0.45	74.6
North	3.2	2.8	12.5

After the traction performance of the redesigned wheel was investigated, the next issue is to discuss to examine the vertical vibration characteristics of the vehicle. During the test, vertical vibration is observed due to the imperfection of the mecanum wheel's circumference. In Fig. 5.13 (a), the 3-D ODR was tasked to move forward at speed 0.1625 m/s, and the position meter was used to measure the vertical displacements of the mid-body, front wheel, wheel 1, and wheel 3. The test was aimed at validating the effect of the discontinuous footprint and severe vertical vibration problems on the system. The results were plotted and showed in Fig. 5.13 (b). It can be seen that the mecanum wheel do experience a slight vertical displacement of about 0.323 cm. However, the mid-body only experiences about 0.19 cm vertical displacement. To avoid possible hardware failure, a most robust storage device is needed especially the robot may hit on the vertical obstacle occasionally. In general, the destructive force generated by vibration and shock is best quantified through

the measurement of acceleration. However, the selected embedded board only supports two types of storage device, namely, compact flash (CF) and hard disk. CF card is chosen given that it has an operating shock rating of 2,000 Gs [64], which is about 10 times of 2.5 inch hard disk. As a result, 512 MB compact flash card, which has better shock resistance, was used to replace original 2.5 inch hard disk.

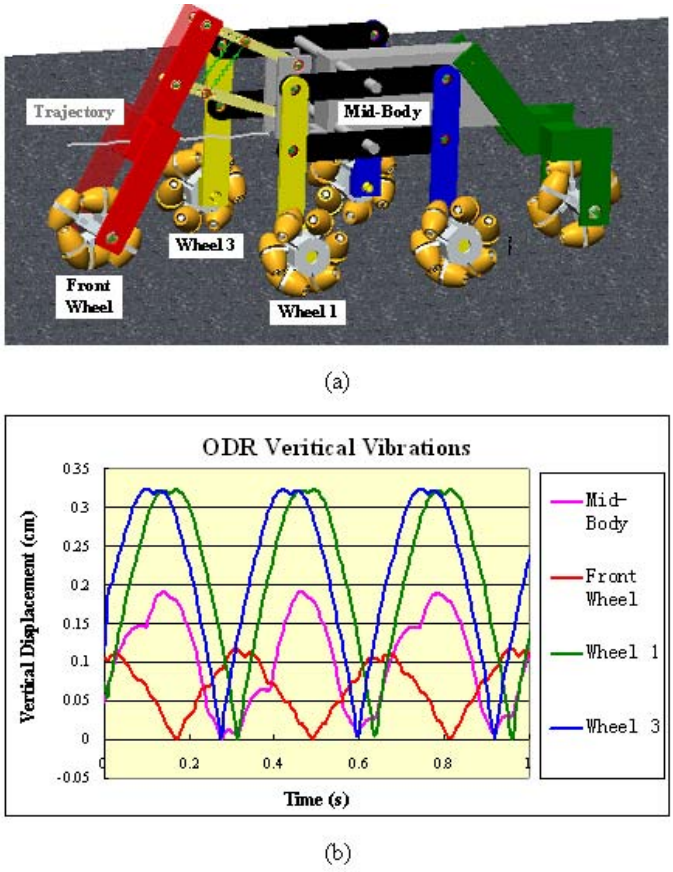

Figure 5.13: The effect of mecanum wheel on 3D-ODR. (a) The 3D-ODR equipped with six ODWs; (b)The mid-body and wheels vertical displacement.

To verify the simulation result, a single wheel sub-system was setup. The vertical displacement of mecanum wheel was plotted by a pen which attached to the subsystem as showed in Fig. 5.14 (a). As showed in Fig. 5.14 (b), the result obtained indicates that the results provided by the MSC. visualNastran indeed close resemble to the realistic prototype behavior. With this information, the author may now be confident in relying the results obtained from

previous simulated model.

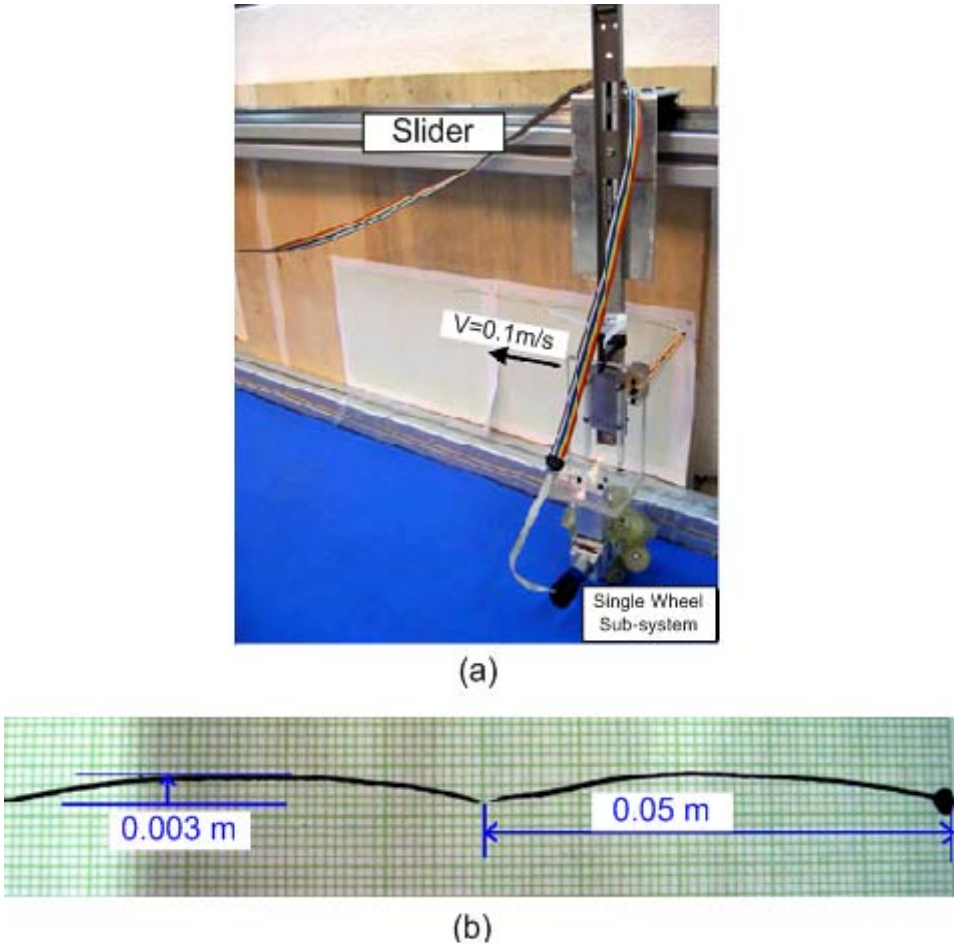

Figure 5.14: The Mecanum wheel vertical vibration test. (a) The single wheel sub-system; (b)The recorded *mecanum* wheel vertical path.

5.4 Development of ODR

5.4.1 Mechanical Design

Fig. 5.15 shows the **Lego** prototype with six actuators and DC power supply. Base on the optimum front fork dimension determined in the Chapter 2, **Lego** prototype was set up to test its step climbing capability. The focuses were on the spring configuration and geometry dimensions. The results showed that the Lego prototype was able to produce moment to lift up the front fork while

encounter the obstacle.

Lego *dacta* [60] was being chosen to be the prototyping set because of it is easier to assemble and dismantle. However, the rigidity of the **Lego** parts limits the possible further used of the prototype. In the test, scotch tape is widely used to fix the connection block of the main body, as these blocks will disconnect easily upon impact. As a result, the author was unable to fully test the step climbing capability. Therefore, it raised the need to construct a new prototype using stronger material and stronger connection.

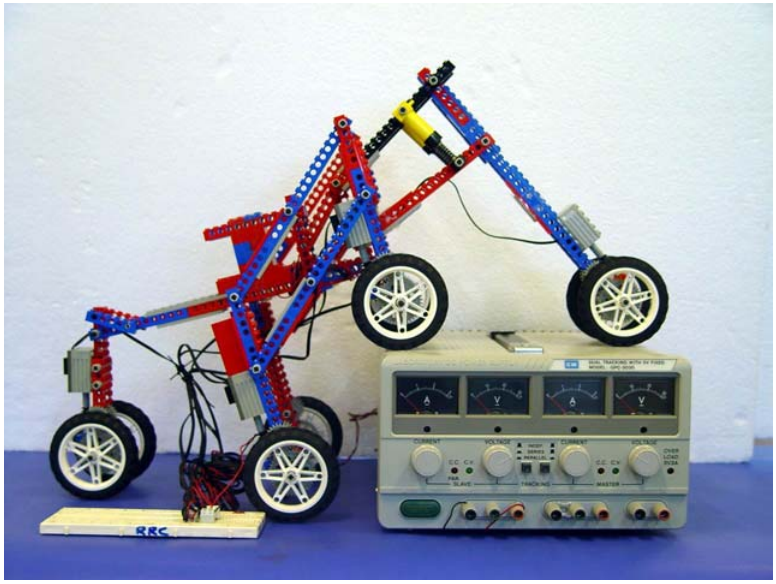

Figure 5.15: LEGO prototype and DC power supply.

Material Selection

Recalled the design specification in Section 3.2, the author aims to reduce the ODR's weight to be as low as possible. A heavy mobile robot will require a larger actuator and higher capacity battery since it needs higher power to drive the robot. Aluminum alloy and acrylic were considered initially for its light weight as compared with steel and other metals. Although the acrylic is almost 45 percents lighter than aluminium alloy, all components' material still can not be acrylic. Acrylic plate is tends to crack when it is subjected to

external forces. Also, poor rigidity also generates undesired warping problems. As a results, the aluminium alloy is selected as structure material.

Actuator Selection

In an attempt to find what types of motors are suitable to drive ODR, numerous online-search were conducted. In the fields of mobile robot, *DC motor*, *R/C servo*, and *stepper motor* are the most popular choices. For our case, the selection criteria is,

- Stepping rotation. It means the application of power cause the shaft to rotate few degrees then stop.
- Bi-directional.
- Torque rating, 6 Nm with safety factor 2 for **Run I** configuration.
- The operating voltage and current draw are crucial. The maximum operating voltage is 14.7 V, and the total current can not draw more 4.5 A (Lithium-ion battery).
- It must allows closed loop control.
- Low cost.

DC servo motor seems as ideal choice to the project. Based on the required torque obtained in Chapter 2, DC servo motor A-max of Maxon [62] is selected. The calculation is listed in Appendix C. Redesign or purchase of external gear and encoder are not needed due to the built-in reduction box and encoder of the motor sets. Some important specifications of this motor are as follows:

Motor data	Front and rear Wheel	Bogies wheel
Maximum Speed (rpm)	45.45	54.74
Gear Ratio	132	190
Operating Voltage (V)	12	12
Maximum Power (w)	11	20
Maximum Torque (mNm)	44.5	15.7
Stall Torque (mNm)	131	70
Encoder Resolution	256	16

Wheel Mounting

The next issue to be considered after the actuator selection is the attachment of the wheels to the motor. The simplest and straightforward way is mounted wheel directly on the shaft coming from the gearbox. However, the gearbox of the motor is required to support the entire weight of the robot. The acceptable shaft load can be easily exceeded when the robot bounces too violently as it moves over uneven terrain. To alleviate this problem, an alternative design is considered as it is difficult to estimate the maximum shaft load when the ODR encountered obstacles. Timing-belt system can isolate the motor and gearbox from the undesired shaft load and shocks. Also, the timing-belt system will raise the center of gravity of the system. It reduces the power needed to "lift" the wheel when encounters obstacle. However, the timing-belt system can not installed to all six wheels due to space constraint in the bogies. The author decided to install timing-belt to front and rear forks, and bevel gear drive is selected for bogie to solve above problems. The mechanical design of the was implemented in the CAD software system SolidWork; the design consists of three subassemblies, namely,

- Front fork sub-assembly

- Bogie sub-assembly
- Rear fork sub-assembly

The drawing and picture of complete design are shown in Figs. 5.16 (a) and (b). The front fork and rear fork use timing belt as mechanical drive, and direct drives are installed to the bogie. The picture of the drives are shown in Fig.5.17. The next chapter will discuss the control system setup and the effect of PID on system dead reckoning performance.

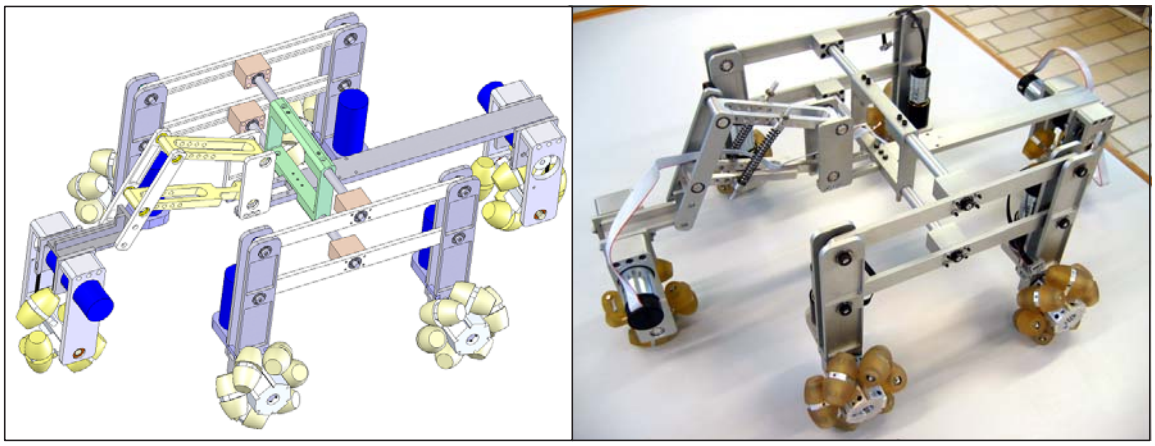

Figure 5.16: Assembly of ODR: (a) CAD model (b) Prototype

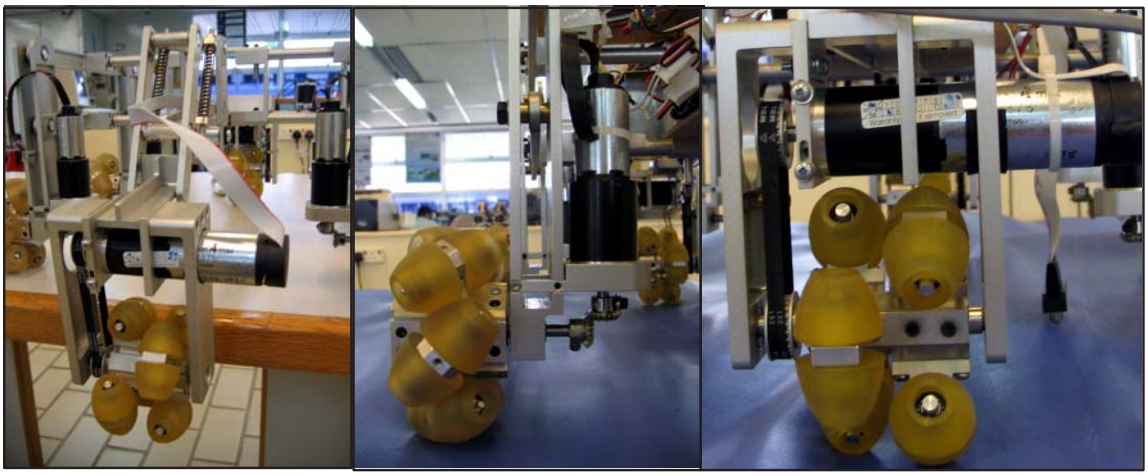

Figure 5.17: Picture of the ODR's mechanical drive: (a) Front fork and timing belt drive; (b) Bogies and bevel gear drive; (c) Rear Fork and timing belt drive.

Chapter 6

Position Feedback Control System

6.1 Introduction

With the emergence of computers and microprocessor technology, the control of position, velocity or torque was no more difficult, expensive, time consuming task. Instead of keep changing the gear with larger or smaller one to change the speed of the operations, the embedded motion control card was developed. In this programmable control system, one may manipulate a variety of system parameters by simply changing the software within the system. In conjunction with feedback devices, like encoder or tachometer, one can maintain the prescribed relationship between desired response and actual response by comparing the difference as a mean of control. In this chapter, the author will discuss the position feedback control system setup, and PID manual tuning used in ODR.

6.2 Description of the Experimental Setup

The feedback control system of ODR includes a embedded board, six motion controllers, six actuators, the mechanical system, position sensors, and power system, as shown in Fig 6.1.

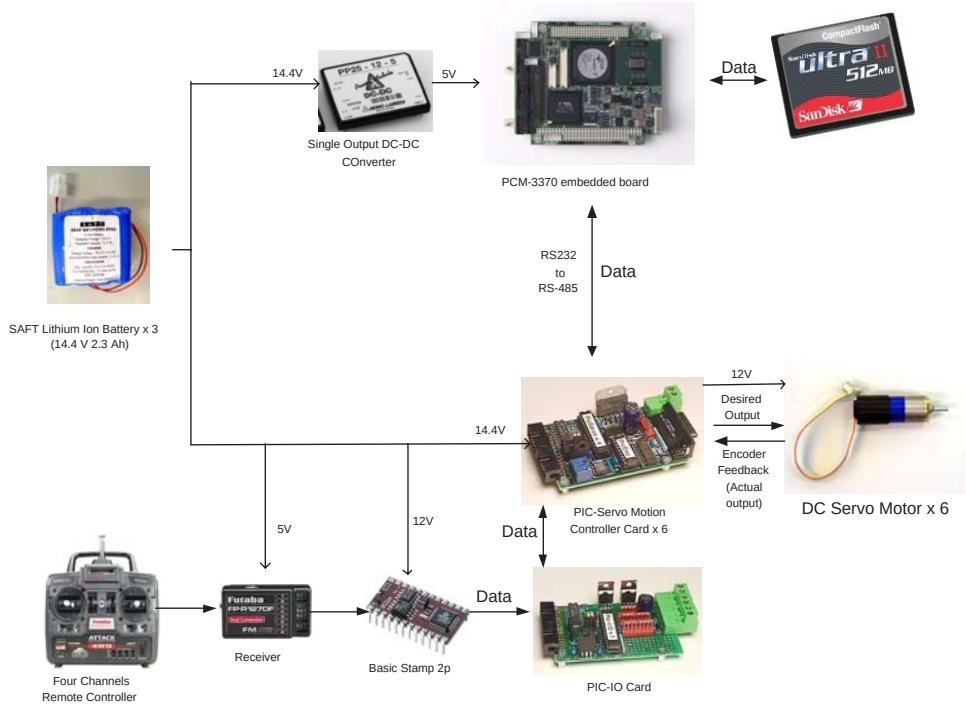

Figure 6.1: The general layout of ODR feedback control system.

6.2.1 Embedded Board

The PCM-3370 embedded board, [65], has a 400-MHz Intel Celeron Processor. It is designed for space constraint applications with only the size of a 96 x 115 mm and weight of 200 g. It supports the full functions of an AT-compatible industrial computer on a single board. The PCM-3370 on board is a low power consumption, +5 V and +12 V only, and high performance processor. The board also contains an SDRAM SODIMM socket that can support up to 512 MB memory. The operating system and data can be stored in ATA-100 hard disk or compact flash type I storage card.

The compact flash card 512 MB is selected as data storage media due its high capacity (up to 12 GB), reliability, and light weight. It also runs in True IDE Mode that is compatible with IDE disk drive, which means it can runs as normal hard disk. The selected operating system is WINDOW 98, and it executes the control programs written in visual basic to control the robot.

6.2.2 Motion Controller

The motion controller used in this robot is the PIC-Servo motion control board [67] from KAE J R Kerr Automation Enginnering [66]. It is a complete servo control system, which includes a servo controller amplifier, serial communication interface, optical encoder interface, limit switch inputs and an auxiliary analog input with pre-amplifier all packed into a board not bigger than 80 mm by 53 mm. It offers an all-in-one solution, which suits our application perfectly. The motion control card contains a velocity profile generator, which computes a sequence of desired position in term of encoder counts at regular interval. It also read in the actual encoder count and generate a position error signal to a digital controller to ensure that this position error is minimized at all time. In our the case, the digital controller is PID controller.

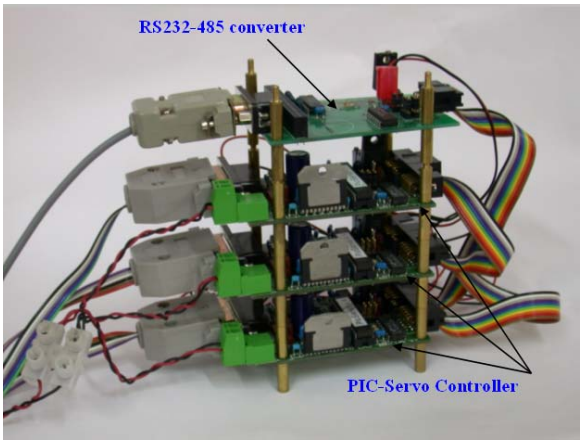

Figure 6.2: Assembled unit of controllers and RS 232-485 convector.

Figure 6.2 shows the assembled unit of 3-controller configuration, the connections for the single card or multiple card setup can be found in [67]. The following lists are the time rate of PIC-servo:

- Servo rate: 1953.12 Hz (max.)
- Serial baud rate: 9600 - 115200 baud (faster rates are possible at lower servo rates)

- PWM frequency: 19531.2 Hz (fixed)
- Max. Command rate: 1000 Hz max.

6.2.3 Rechargeable Batteries

Rechargeable batteries are the most common solution employed by mobile robots for the problem of power system. Lead-acid, NiMH (Nickel Metal Hydride), NiCd (Nickel Cadmium), and lithium ion are the current market available rechargeable batteries. An ideal battery for mobile robot must have very high energy density. It must maintain a constant voltage during discharge. In addition, it have a low internal resistance, therefore be capable of rapid discharge. Other preferable characteristics like low unit cost, unlimited shelf life, and be able to withstand temperature extreme. Unfortunately, non of the above battery technology exhibit all these characteristics. Thus, trade-offs must be made based on the requirements of the task. Fig. 6.2.3 serves as general guide when choosing the proper trade-offs among the above characteristics.

Table 6.1: Comparison of characteristics for selected batteries [68].

Rechargeable Battery	Lead Acid	NiCd	NiMH	Lithium Ion
Energy Density (Wh/kg)	30	40-60	60-80	150
Cell Voltage (V)	6 / 12	1.2	1.2	3.6
Typical Capacity (Ah)	2	0.8	1.3	1.2
Internal resistance (mOhms)	100	100-200	200-300	150-250
Comments	Available in a wide variety of size.	Low internal resistance.	Better energy density than NiCd, expensive.	Excellent energy density, high unit cost, and no memory effect.

All number listed here are approximate.

NiCd and NiMH both share many characteristics in common. Currently, the NiMH batteries are about two times as costly as NiCds, but the energy density of NIMHs is about 50 % more than NiCds. The rechargeable sealed-lead acid battery are available in a variety of rectangular sizes. They are relatively inexpensive, however the energy density is poor. Lithium ion batteries, a new rechargeable battery, are becoming a practical alternative for mobile

robot power. It provides high capacity by weight and by volume, which is about twice that of NiCds. In addition, the lithium ion batteries do not suffers "memory" effect, which is common for other batteries. The drawbacks are the unit cost, it costs about 1.7 times of NiMHs, and it is not recommended for applications requiring very high instantaneous current such as power tools.

In our case, the weight of the battery is our main concern. Three **SAFT** [69] lithium-ion batteries are used to power ODR. A single DC-DC converter, PP25-12-5, from **Densei-lambda** [70] is needed to supply constant voltage (5 V) and sufficient current (4 A) to the PCM-3370 embedded board. The maximum recommended current of the lithium batteries is 4.5 A. The calculated surged current for the ODR is 2.6 A, given that the robot weight is 8 kg and average speed is 0.1625 m/s.

6.3 Feedback Control System

A feedback control system is defined as the application of programmable hardware and software for the control of one or more linear or rotary motions. It compares the desired trajectory to the actual trajectory and computes the appropriate signals to be used for wheel movement routine. In our current implementation, only PC mode and tele-operation mode are realized. The motion control system will be comprised of the following basic elements: embedded board, programmable motion controller, amplifier, actuator and encoder, as shown in Fig. 6.3.

The main aim of motion control system is to control any one, or combination of the following parameters: position, velocity, and torque. As a result, a trapezoidal velocity function is required to generate a smooth trajectory, which always limiting the acceleration and deceleration values to acceptable values. The trapezoidal velocity profile, which time interval of acceleration,

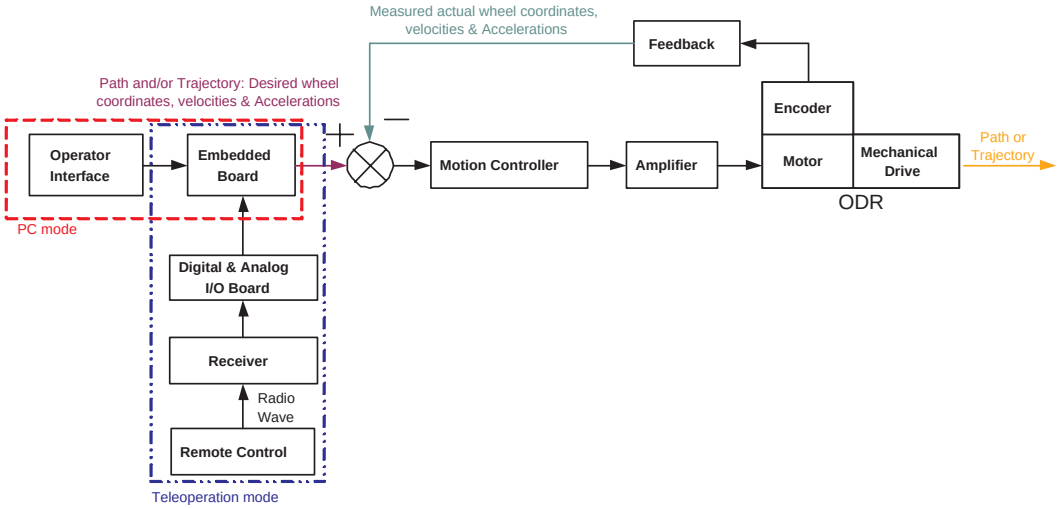

Figure 6.3: Schematic diagram of feedback control system.

slew velocity, and deceleration are all equals to one-third of the total motion time, is implemented. The profile is shown in Figure 6.4.

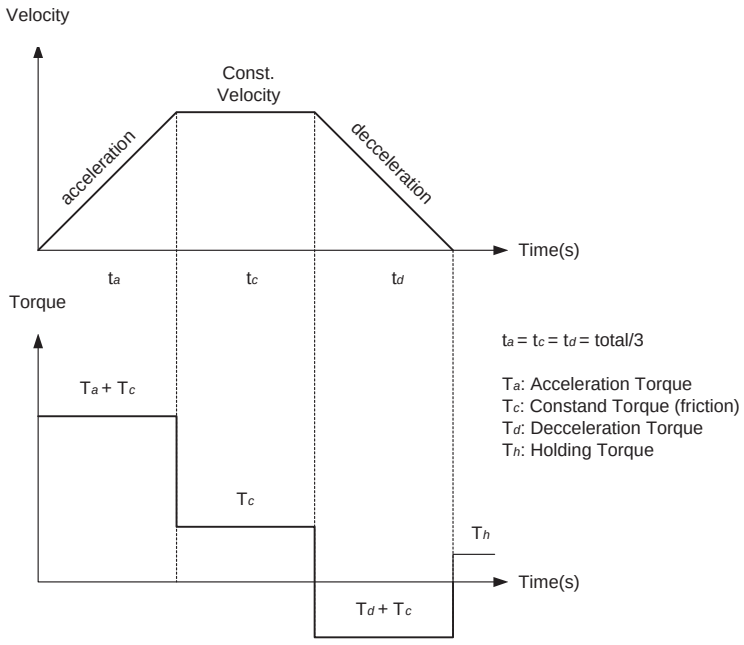

Figure 6.4: Trapezoidal profile configuration.

When commanding a trapezoidal profile motion, the motor should always start at zero velocity and the move will end also at zero velocity. When a motion is started, the motor will accelerate up to the programmed peak velocity

at a constant acceleration, which is also programmable. It will then slew at the maximum velocity until it nears the destination and begins to decelerate at a constant acceleration. When the motor approaches its goal position, the motor controller will continue to servo the motor to the specified goal position.

Sample Calculation of Joint Parameters

Given:

No load speed : 7630 (rev/min) / 190 (gear ratio) =40.16 rpm

Encoder resolution lines: 16 lines (bits)

Wheel circumference : $2 \times \Pi \times 50$ mm =314.16 mm

Servo rate : 1.953 kHz (max)

Tick time: 0.512 ms

The position, velocity and acceleration are programmed as 32 bits quantities in units of encoder counts and servo ticks. In another words, a transfer equation is needed to transfer the desired wheel velocities to encoder counts per servo tick. For example, a velocity of one revolution per second of a motor with a 16-line encoder and reduction gear with internal gear ratio 190 at a tick time of 0.512 ms would correspond to a velocity of 6.226 counts/tick. Velocities and accelerations use the lower 16 bits as a fractional component so that the actual programmed velocity would be 6.226×2^{16} or 408022.

1 cycle = 4×16 lines $\times$ 190 (internal gear ratio) = 12160 counts/rev

Velocity = 1 rev/s $\times$ 12160 counts/rev $\times$ 0.512 ms/tick = 6.226 counts/tick

Programmed velocity = 6.226×2^{16} = 408022 counts.

An acceleration of 3 rev/sec/sec, which would bring actuator rotation speed up to the desired speed in 1/3 of total time, would be 0.0021 counts/tick/tick

with the lower 16 bits the fractional component This would be programmed as 0.009563×2^{16} or 627.

Acceleration = 3 rev/s/s × 12160 counts/rev × 0.512 ms/tick × 0.512 ms/tick

= 0.009563 counts/tick/tick

Programmed Acceleration = 0.009563×2^{16} = 627 counts

Position is programmed as a straight 32 bit quantity with no fractional component. Therefore, 1 degree is corresponding to 15.3 counts.

Number of counts per degree = 1 degree × 12160 counts / 360 degree = 33.8 counts per degree

In addition to the PC control mode, the author also set up a tele-operated system consists of remote controller, receiver, programmable digital and analog I/O board, and Basic Stamp [63]. The remote controller that uses radio wave technology to transmit signal will be installed. The receiver is set up on the robot. The remote signal will be decoded by Basic Stamp and passed the instruction to the ODR. Although radio wave still has its limitation inside a concrete building but compared to IR remote, which used in OWMR II, the radio wave remote has larger transmitting range.

6.3.1 PID Control

The aim of PID tuning is to obtain a system with no overshoot, fast rise time, and probably no steady-state error. A proportional controller (K_p) will have the effect of reducing the rise time and will reduce, but never eliminate, the

steady-state error. Steady-state error is defined as the difference between the input and output of a system in the limit as time goes to infinity (i.e. when the response has reached the steady state). The steady-state error will depend on the type of input (step, ramp, etc) as well as the system type (0, I, or II). An integral control (K_i) will have the effect of eliminating the steady-state error, but it may make the transient response worse. A derivative control (K_d) will have the effect of increasing the stability of the system, reducing the overshoot, and improving the transient response. Effects of each of controllers K_p, K_d, and K_i on a closed-loop system are summarized in the Table 6.2.

Table 6.2: The effect of PID [72].

CLOSE LOOP RESPONSE	RISE TIME	OVERSHOOT	SETTLING TIME	STEADY STATE ERROR
Kp	Decrease	Increase	Small Change	Decrease
Ki	Decrease	Increase	Increase	Eliminate
Kd	Small Change	Decrease	Decrease	Small Change

Note that these correlations may not be exactly accurate, because K_p, K_d, and K_i are dependent of each other. In fact, changing one of these variables can change the effect of the other two.

The control filter used by the PIC-SERVO is a proportional-integral-derivative (PID) filter. According to controller manual [67], 8 parameters and limits monitoring the performance of motor. There are:

Position gain K_p	Velocity gain K_d
Position gain K_i	Integration limit IL
Output limit OL	Current limit CL
Position error limit EL	Servo rate divisor SR

The output to the motor amplifier is the sum of three components K_p, K_d, and K_i. There are the servo gains that will be programmed to optimise performance for a particular motor. The following is a description of each gain:

- K_p is proportional to the position error providing most of the error correction
- K_d is proportional the change in the position error that provides a stabilizing damping effect
- K_i is proportional to the accumulated position error, which helps to cancel out any long-term error, or "steady state error".

The PID control filter, operating on the command position and the actual position each servo tick, produces an output calculated as follows:

Output $= K_p(pos_{error}) + K_d(prevpos_{error} - pos_{error}) + K_i(integral_{error})$

where,

pos_{error}: the current command position minus the actual position.

$prevpos_{error}$: position error from the previous servo tick.

$integral_{error}$: the running sum of pos_{error} divided by 256.

To keep from growing a potentially large $integral_{error}$, the running sum is bounded by a user-specified integration limit. By temporarily setting the integration limit to 0, the user can zero out the accumulated running sum.

6.3.2 Manual Tuning

Selection of the optimal PID control parameters can be done analytically, but more typically, they are chosen through experimentation, manual tuning method. In order to design a proper PID controller for our system, the steps shown below are used to obtain a desired response,

1. Obtain an open-loop response and determine what needs to be improved.
2. Add a proportional control to improve the rise time.
3. Add a derivative control to improve the overshoot.

4. Add an integral control to eliminate the steady-state error.

5. Adjust each of K_p, K_d, and K_i until you obtain a desired overall response.

To demonstrate the effects of the three control parameters on our system, the rear fork wheel was used as an example. The first step is completely assemble the robot before tuning of motion parameters. Note that, the tuning may needs to repeat again if new equipment is added.

Proportional Term

The proportional term, K_p, indicates how hard the actuator should work to

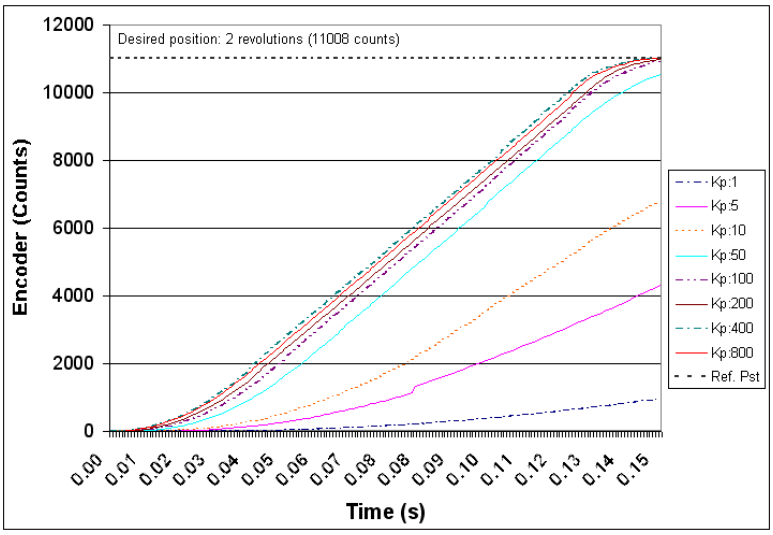

Figure 6.5: The motion trajectories when using only K_p. ($K_p = 1$ through 800, K_i=0, K_d=0)

remain in its current position. It means that the controller will try to servo the motor stayed at its desired position when the actuator is enabled. Fig. 6.5 shows the result of moving 11008-encoder count (2 revolutions) using $K_p = 1$ to 800. If K_p is too low, the actuator does not get close to desired position. As the K_p is increased to 800, the motion trajectories get closer to desired position, then it begins to overshoot the target them backs up. Even greater K_p values will only make the actuator overshoot and then oscillate around the desired position.

Derivative Term

The derivative term, K_d, controls the velocity of the system. It combines with K_p to tell the system the desired velocity as well as desired position. The PIC-Servo controller will internally generate both desired values during the move. If K_p is too large, any small disturbance might cause the controller turns the motor on in opposite direction. Fig. 6.6 shows that what happens when K_d increased from 500 to 6000. It shows the performance of the system gets worsen and never reached the desired position due to able reason.

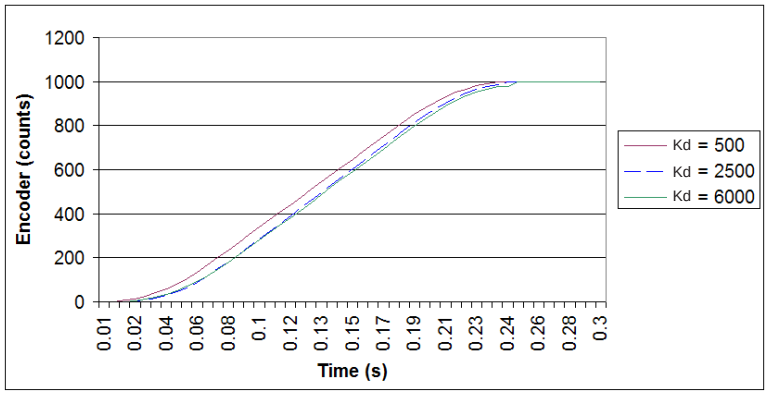

Figure 6.6: The motion trajectories when using K_p and K_d. ($K_p = 320$, K_i=0)

Integration Term

The integration term, K_i, is often used to eliminate the steady state error. It allows the error value to sum up, and slowly move toward desired position. The controller will not turn off PWM value means it will be able to stop the motor at desired position even if there is a disturbance. However, the PWM remains on also allows the error value to accumulate over time. It may leads to unstable response. The Fig. 6.7 shows the impacts of K_i value on the system.

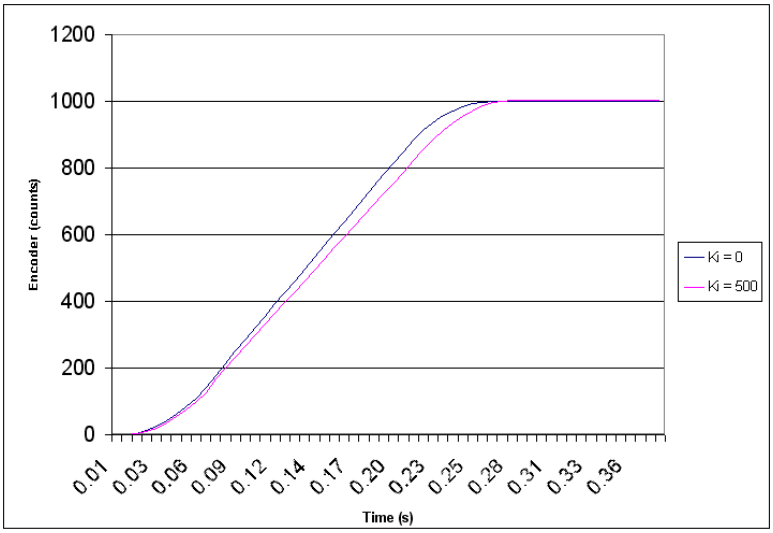

Figure 6.7: The motion trajectories when using different K_i values. (K_p = 1220, K_d=3600)

Chapter 7

Motion Planning and Testing

7.1 Motion Planning - Omni-directional Mobility

For testing omni-directional mobility, various trajectories are performed by ODR. For all tests, no external sensors are used. The magnetic incremental encoder is enough for making the ODR trajectory asymptotically close to the desired path on flat terrain. All motions are based on kinematic equations derived in Chapter 2, the maximum speed is limited to 0.1625 m/s.

7.1.1 Theory

In Chapter 2, the kinematics model of the 6-wheel ODR is derived. This means that by using the equations of the motion of the ODR, we can determine what the required wheel velocities in order to move the ODR to desired position and orientation. In the mobility analysis of 2-DOF WMRs, two fundamental motions are translation and rotation. With ODW, the ODR, which is 3-DOF, is fully capable of executing more complex motion like dual-path motion. The path planning of ODR will be discussed in the following sections.

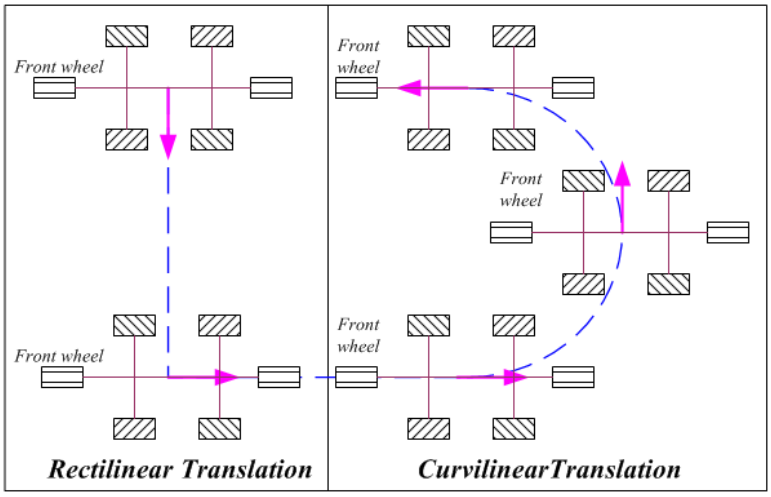

Figure 7.1: Rectilinear translation and curvilinear translation.

7.1.2 Translation

Translation is a motion in which the orientation remains unchanged. In *rectilinear translation*, all points in the platform move in parallel straight lines; while in *curvilinear translation*, all points move along congruent curves as shown in Fig. 7.1. Clearly, curvilinear translation is a special case of rectilinear translation. In both cases, the motion of the platform can be completely described by the motion of any point in the body, since all points undergo the same motion.

7.1.3 Rotation

There are two types of rotations. In the first case, as shown in Fig. 7.2, the center of rotation (COR) is selected at the operating point C and the ODR rotates with an angular velocity of $\dot{\psi}$. As for the second case in the same figure, the COR is selected at an arbitrary point U and the ODR rotates with an angular velocity of $\dot{\psi}$.

One distinct difference between the two scenarios is the displacement of the operating point C during rotation. Point C in the first case is fixed during rotation, while in the latter one it changes with time during rotation. The

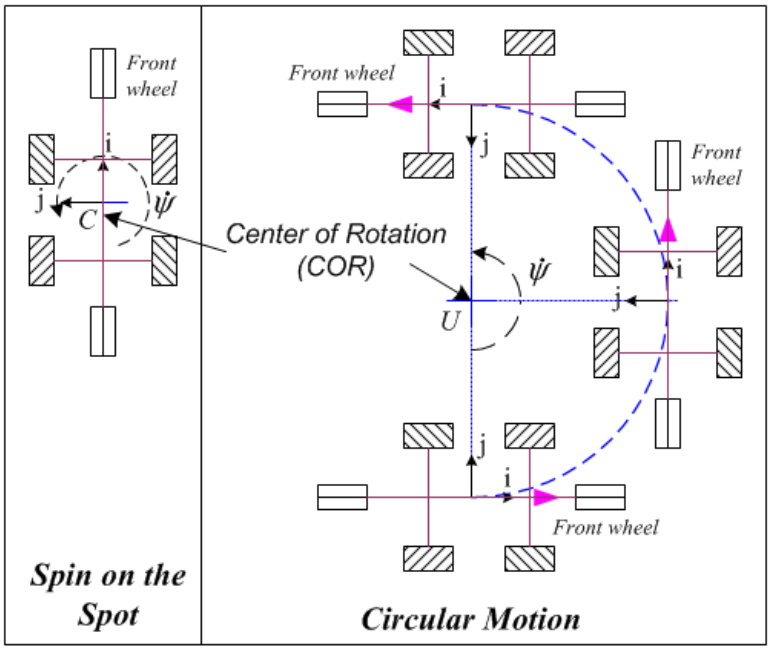

Figure 7.2: WMR in rotation with COR located at the operating point C and with COR located at an arbitrary point U.

ODR can only rotate about the COR. However, the vectors **j** must always pointing towards the COR for second case. In this report, only the first case is tested to examine ODR zero turning radius property.

7.1.4 Dual Path: Combined Translation and Rotation

Let $\mathbf{r}_C$ be the position vector of the center of the disk point C with respect to its initial point, and the ODR has rotated counter-clockwise through an angle ψ, as shown in Fig. 7.3. The no-slip condition requires that the horizontal displacement, d, equals to a circular arc as follows:

$$d = r\psi$$

Therefore, we have,

1. Position vector of point C

$$\mathbf{r}_C = r\psi\mathbf{j} \tag{7.1}$$

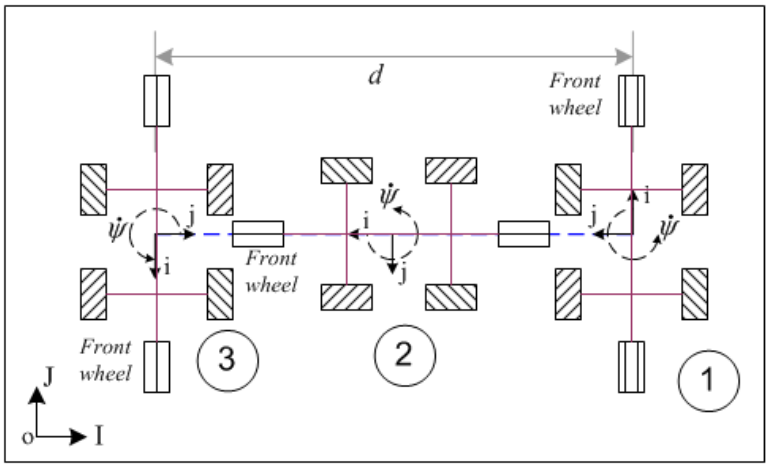

Figure 7.3: Dual-path motion.

2. Velocity vector of point C

$$\dot{\mathbf{c}} = \mathbf{v}_C = r\dot{\psi}\mathbf{j} \tag{7.2}$$

3. Angular velocity of any arbitrary point P on the disk (constant rate)

$$\dot{\psi} = \frac{\psi}{t} \tag{7.3}$$

The actuated joint-rate $\dot{\theta}_i$ can be determined based on $\dot{\mathbf{c}}$ and $\dot{\psi}$ given in eqs. (7.2) and (7.3), which are,

$$\dot{\theta}_n = \frac{-1}{r_w} \begin{bmatrix} r & -1 & -1 \\ r_3 & -1 & 1 \\ r & -1 & 0 \\ r & 1 & 1 \\ r & 1 & -1 \\ r_6 & 1 & 0 \end{bmatrix} \begin{bmatrix} \dot{\psi} \\ 0 \\ r\dot{\psi} \end{bmatrix} \tag{7.4}$$

7.1.5 Results

This section summarized the performance of the 6-wheel ODR during testing. Once the path equations for various motion paths are established, the next

step is translate its to programming codes. The program, *ODR Test*, which is written in visual basic, is used to test the omni-directional mobility of the ODR. It comprises basic controls (translation and rotation) and a number of demontration applications. The form of the program is shown in Fig 7.4.

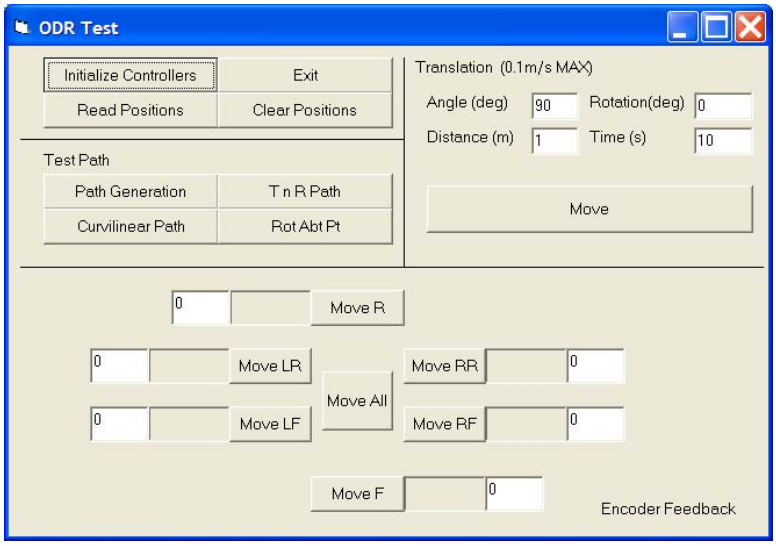

Figure 7.4: The Visual Basic form: "ODR Test".

The ODR was tested in its ability to execute three different type of motions. In the first test, the ODR is tasked to move in a octagon shaped path without any change in orientation of the ODR. This type of the translation, referred to as rectilinear translation. Initially, the constant 10 mm distance error for forward and backward motion and 100 mm distance error for lateral motion were observed. It is due to the *mecanum* wheel's imperfect circumference. The final distance error was less than 30 mm after the distance errors were compensated .

In the second test, the ODR is tasked to spin on the spot clockwise and anti-clockwise 360 degrees. In the final test, the ODR is programmed to move in a straight path and at the same time rotate about its centre. This type of motion, the author termed it as dual path. Three parameters, $\dot{x}$, $\dot{y}$, $\dot{\psi}$, needed to be controlled simultaneously. Therefore, the dual-path is ideally to prove that the 6-wheel ODR is a 3-DOF system. For curvilinear and dual path

motion, the smooth path was obtained. The measured error is less than 10 cm when the ODR was tasked to translate 1 m and rotate a full cycle of 360°.

7.1.6 Remarks

The author has demonstrated the ability of a ODR with six ODWs, to execute three different types of motions, namely, *rectilinear translation*, *rotaion*, and *dual-path* motion. The results show that this class of WMR has very fluent maneuverability. During the test, it was observed that the vertical vibration, and the imperfection of the wheel circumference caused most of the odometry errors. Therefore, a correction parameter are added kinematic equation to compensate the above errors. The imperfection of the wheel circumference can be solved by increasing the numbers of the rollers. Spring suspension system can be installed to minimize the vertical vibration.

In tele-operated mode, the control inputs are listed in Fig. 7.5. In the next section, all experiments will be conducted in tele-operated mode. The only input commands is moving forward.

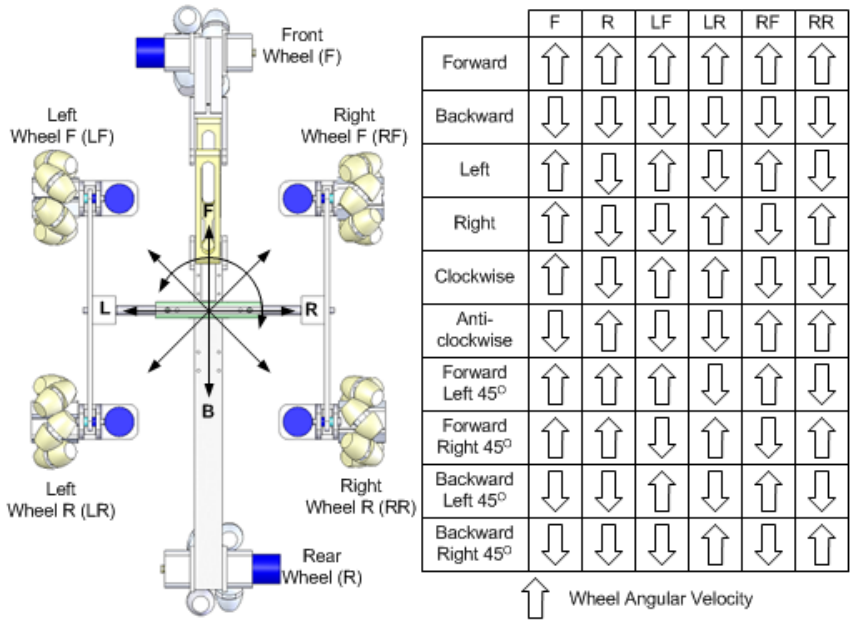

Figure 7.5: ODR control inputs in tele-operated mode.

7.2 Motion in Structured Environment

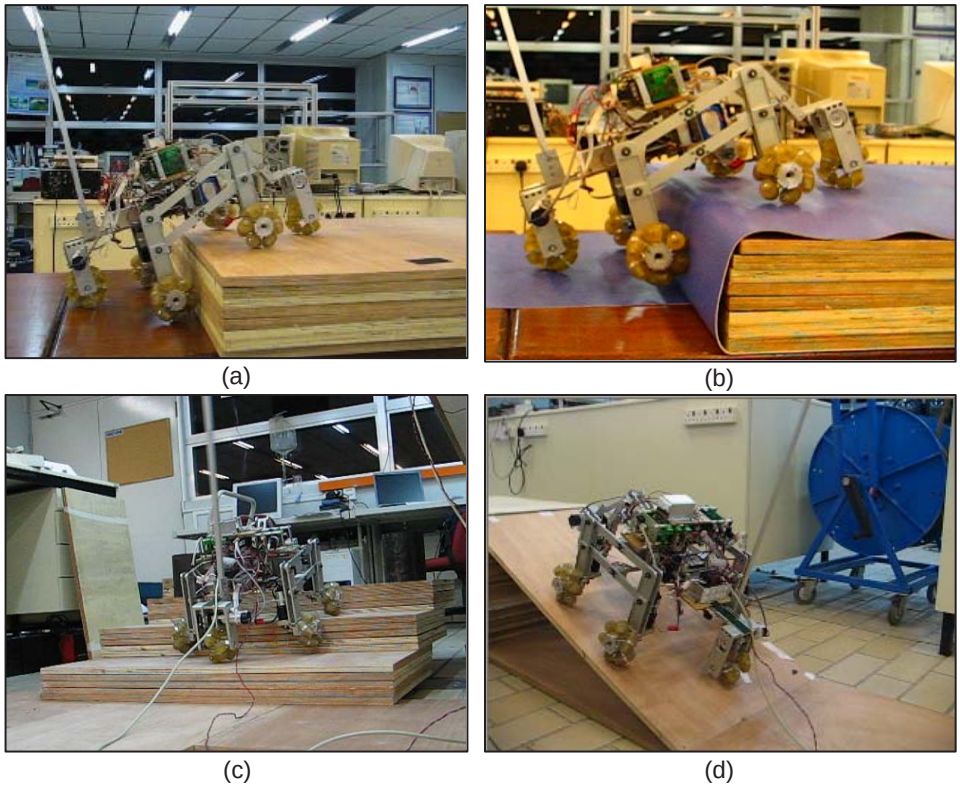

Figure 7.6: ODR in actions: (a)Wooden step (150 mm) (b)Carpet step (150 mm) (c)Wooden steps (100 × 290 mm) (d)Wooden slope (25 degs)

To investigate the motion capability of constructed ODR on undulating terrain, it was commanded to overcome three designed obstacles, namely, step, slope, and stair. The plywood was used to form the various obstacles, as shown in Fig. 7.6.

One of the objectives of this research work was the overcoming of a step which height had to be st least 1.5 times the wheel diameter. Two different types of terrain, wood and carpet, were setup. The only motion command is moving forward. All motions are based on kinematic equations derived in Chapter 2, the maximum speed is limited to 0.1625 m/s. Fig. 7.7 shows the main sequences of the rover climbing a step. First, the front fork gets on the step, compressing its spring then the energy accumulated in the spring

helps the first wheel of the bogie to climb. When the second bogie wheel is in contact with the wall, the bogie turns around the step. Finally, the last wheel can easily get on the step.

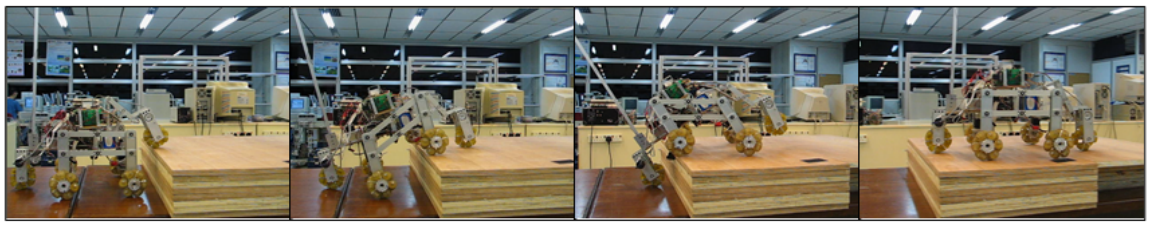

Figure 7.7: Climbing sequence for a step of 150 mm high (1.5 times the wheel diameter). (a) The front wheel climbs up the step; (b) The front bogie wheels climb up the step; (c) The rear wheel climbs up the step; (d) The ODR on the step.

The next mission is to test rover stairs climbing ability. Due to a good correlation between the bogies and rear fork sizes and the steps dimensions, the rover is able to climb 100 mm x 290 mm stair. However, the rover failed to overcome 150 mm x 290 mm stair due to poor traction.

In the third test, the rover is tasked to climb up a wooden slope. The objective is determined maximum climbable slope. The experiment shows that the rover is able to overcome 30 degrees slope effortlessly.

7.2.1 Discussion of Dynamic Force Analysis

At first, the dynamic force equations of ODR derived in Chapter 2 were used to calculated driving torques required to driving up the slope. The objective of the analysis is to compare the driving torques between the analytical and simulation methods. However, the rank of 36 $\times$ 36 matrix becomes 35 or less in the four configurations, as shown in Fig 7.8, where at least two links are co-linear. Since the matrix is singular, it does not have an inverse. Moreover, the results of any configurations that are closed to the above configurations may be inaccurate even the rank is 36.

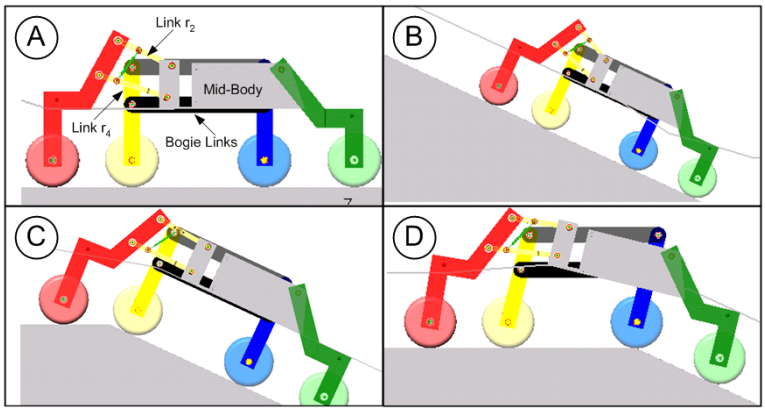

Figure 7.8: Singularity configurations: (a) Mid body and bogie links; (b) Mid body and bogie links; (C) Mid body, link r_4 and bogie links; (C) Link r_2 and Mid Body are aligned.

For example, the inverse dynamic solutions of ODR on flat terrain as shown in Fig 7.8(a) is obtained by changing the angle between mid-body and body horizontal links. As seen in Fig 7.9(a), the results is unrealistic especially when $(\theta_r - \theta_5)$ is closed to zero as it is singular. In fact, reasonable amount should be closed than 0.67 Nm, given the rover weight is 8 kg, and coefficient of friction is 1. To overcome the problem, we assume the $(\theta_r - \theta_5) = 4$ degrees for $-4 \leq (\theta_r - \theta_5) \leq 4$. The filtered result helps to reduce spike, as depicted in Fig 7.9(b). However, it may not working well when more than 2 links involved as showed in Fig 7.8(c), where bogie links, mid-body and link r_4 are aligned. It is a mathematical problems. As a result, we need to look at other methods to verify the simulation results.

To verify the simulation results derived in Chapter 3, an alternative method is proposed. A simple circuit, shown in Fig. 7.10, is setup to measure the required current for ODR driving up the slope. The reading is converted to driving torque using the eq (7.5) and shows in Fig. 7.11(a).

$$T_m = K_m I G E_G E_M \tag{7.5}$$

where T_m: Driving Torque, N; K_m: Torque Constant, Nm/A; I: Measured

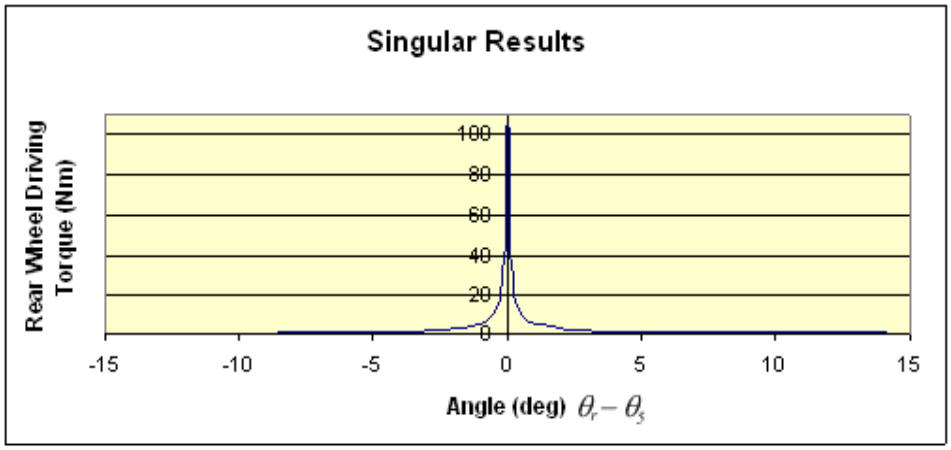

(a)

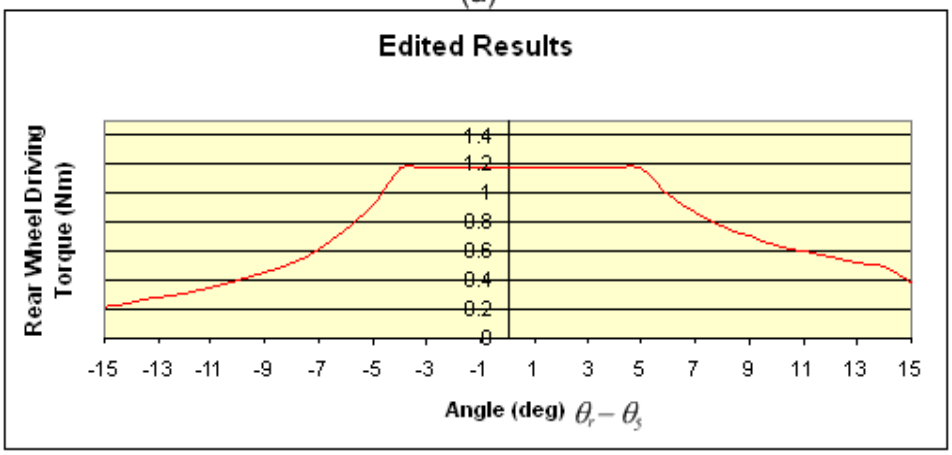

(b)

Figure 7.9: Derived driving torque of ODR's rear wheel on flat terrain. (a) Singular results; (b) Filtered results.

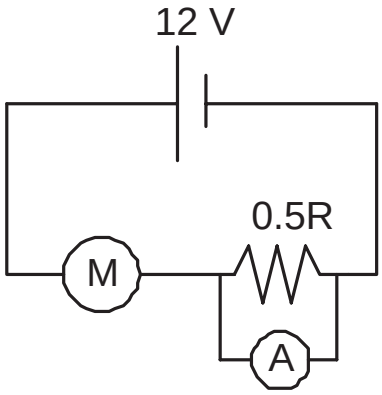

Figure 7.10: Circuit diagram for driving torque measurement.

Current; G: Gear Ratio; E_G: Maximum Efficiency of Gear Box; E_M: Maximum Efficiency of Motor.

As shown in Fig. 7.11, the measured result is not exactly matched the simulated result found in Chapter 4. The major difference between two setups is the method of handling disturbances. First, The real prototype is able to maintain motor output through PID control that mentioned in Chapter 5. However, the means of MSC. visualNastran Desktop handling uncertainty is not known. Also, the ground coefficient of friction used in the simulation is different from the real test. However, the output patterns of the measured values enabled us to meet the objective listed in Chapter 4, which is to determine the maximum output torque for actuator selection.

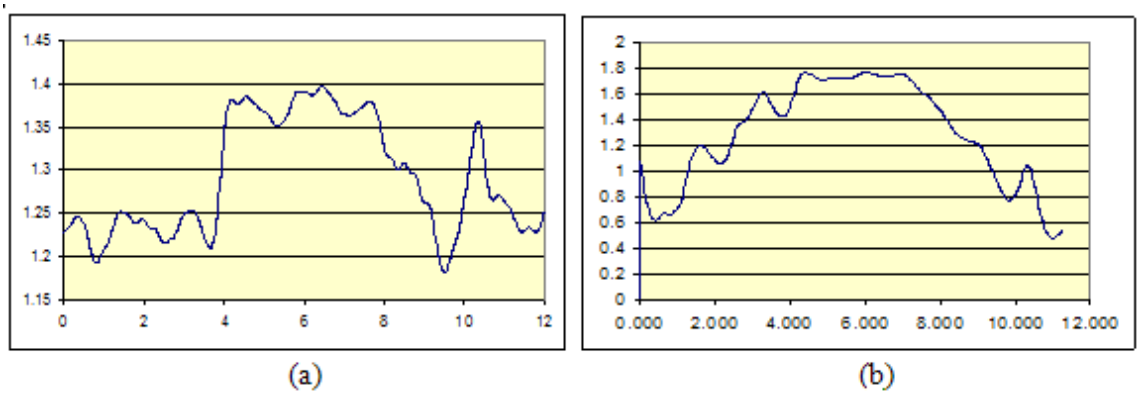

Figure 7.11: Rear wheel driving torque: (a) Measured Result; (b) Simulation Result.

Chapter 8

Conclusions and Recommendations for Further Research

This chapter concludes the work done in this project and discusses some possible future development of 6-wheel ODRs.

8.1 Conclusion

The research presented in this report revolved around four main topics, namely, kinematic and dynamic analysis of the system, motion analysis of ODR, design, control system setup of an ODR. Within the scope of the topic of design, the author discussed both the design of the ODW, as well as the design of the robot passive locomotion. The 2-D and 3-D simulation interface was setup to further investigate the step and stair climbing performance of the ODR. Conclusion pertaining to the above four topics are drawn separately and summarised below.

1. Kinematic and dynamic analysis of the ODR

In order to better understand the characteristic of the locomotion of the 6-wheel ODRs, the kinematic and dynamic model of the robot were formulated in Chapter 2. The author derived first the kinematic model for a generic 6-wheel platform. Then, we derived the kinematic model for the ODW. Com-

bined this two models to get composite kinematic equation of the system. It offers singular-free operations, as no steering angle involved. To verify the kinematic model, the ODR was tasked to follow various sharp angle path (rectilinear translation), smooth circle (rotation), as well as combined translation and rotation, as shown in Chapter 7. The results show that this ODR is highly maneuverable; able to response to quick changes in direction; and allows control of its orientation without any worry of running into singularities. In addition, the dynamic models of ODR is developed for initial study and future development.

2. Motion Analysis of the ODR

Shrimp suspension system and parallel bogies were employed as robot locomotion. It adapts to the terrain profile passively and it has better climbing capability than other rovers. The focus of the research was to determine the optimum configuration of the ODR not only for step climbing but also for the stair climbing. It means the rover must be able to overcome 0.15 m (average step height) obstacle with minimum time consumed. First, the analytical synthesis, front fork simulation and P_max test were used front fork dimension to find the optimal dimension of front fork mechanism as shown in Chapter 3. After that, the 3D model of ODR in MSC. visualNastran environment was setup to investigate the relationship between the obstacles and the ODR as discussed in Chapter 4. By means of creating three tests for a terrain consists of three different types of obstacle, namely step, slope, and stair, the ODR's dynamic behavior was monitor. In chapter 5, the found dimensions will be tested its ability on **Lego** prototype before proceed to fabrication.

3. Design of the ODR

An ODR with six redesigned ODWs was developed and prototyped as shown in Chapter 5. The geometry dimensions are based on the simulation results obtained from Chapters 3, and 4. Also, the ODWs were re-designed and proto-

typed to alleviate poor traction and undesired friction between the wheel hub and rollers. The polyurethane was used as roller material, and an alternative hub design was proposed. Positioning repeatability of the redesigned wheel was tested on OWMR II. The errors are improved significantly as shown in Table 5.2. The results can be used for future development. In addition, the author also discuss the purpose of having two different mechanical drives, timing belt and bevel gear, in the system.

4. Position feedback control System of the ODR

The control aspect of the 6-wheel ODR has been covered in Chapter 6. The details of setting up of the motion control system, manual tuning of the amplifier, PID of the controller, and the trapezoidal velocity profile, are highlighted. The ODR is controlled using the control program written in visual basic. In addition, the details of tele-operation system are unveiled.

8.2 Suggestions for Further Research

The current design is adequate to fulfill its task as and omni-directional platform and path test-bed. However, the ultimate aim of these research is to create an ODR with excellent off-road capability without giving up the WMRs high mobility on smooth terrain. if ODR is to become more useful, several design changes need to be implemented. Any changes should be carefully considered, however, since a single change, mechanically or computationally, could drastically alter the performance of all remaining systems. The following recommendations are suggested for the direction of future work.

1. Improvements on Current Prototype Design

As mentioned, the ODR experiences vertical vibration due to its wheel's circumference imperfection. To alleviate the problem,the numbers of roller on the mecanum wheel can be increased to smooth the ODR motion. An alternative

solution is to install four additional suspension systems to absorb the impact owing to ODW vertical vibrations. It is hoped that motion of the ODR will be smoothen after that.

2. Positioning System

For dead-reckoning, the current system with only incremental encoder is not enough for outdoor terrain. Because the encoder only provides the relative position of the robot, and the accuracy is depend on the flatness of the terrain. To determine the absolute location of the robot, the simplest solution is make use of GPS signal. The nice feature of GPS implementation is that GPS receiver outputs absolute location of the roving robot. GPS positioning would also help in maneuvering because we know exactly current position and target definition, thus can effectively adjust control effort.

3. Crash Prevention Module

In general, the rover must be able to roam around and:

1. Judge the height of obstacles
2. Decide whether it can climb them
3. Climb any step that is within its surmountable height
4. Line itself up perpendicular with the step
5. Do not climb down from the step since it will break the rover structures
6. Move away from impassable objects i.e. walls

Sometimes, the operator may not identify possible threat, likes hole, and continually commands the robot move forward. Therefore, it is important to develop a crash prevention module to overwrite the human control commands to protect the system. And, it must alert the human operator and takes the alternative path.

4. Torque feedback control system

Currently, encoders are the only feedback sources in our system. Also, slippage are always encountered during the step climbing process. In order to avoid wheel slip, the wheel driving torque should satisfy the following equation

$$T_m \leq r_w \mu N \tag{8.1}$$

where T_m is driving torque, r_w is wheel radii, μ is static friction coefficient, and N is normal force acting on the wheel. In general, it difficult to know μ precisely. However, the ODR performance on undulating terrain can be improved by minimizing the $T_m/(r_w N)$. The system can self-adjust the wheel output speed to reduce the slippage based on torque reading.

Bibliography

[1] Asimo. 2003. The humanoid robot by Honda. *http://www.honda.co.jp/ASIMO*

[2] Aibo. 2003. The Robot dog by Sony. *http://www.sony.com/hitbox/goto-blue-play-aibo.shtml*

[3] Necoro. 2003. The Robot cat by Omron. *http://www.necoro.com/home.html*

[4] H.R. Everett. 1995. *Sensors for Mobile Robots: Theory and Application*, Natick, Massachusetts. A K Peters.

[5] Pyramid Rover. 2003. The Rover by IRobot for National Geographic mission. *http://www.irobot.com/industrial/prover.asp*

[6] Mars Exploration Rover. 2003. The Rover by Nasa for Mars mission. *http://mars.jpl.nasa.gov/mer/overview/index.html*

[7] K. Schilling and C. Jungius. 1996. Mobile robots for planetary exploration, *Control Engineering Practice*, (4)4:513–524.

[8] Fiorini, P. 2000. Ground mobility systems for planetary exploration, *Proc. IEEE Int Conf on Robotics and Automation, San Francisco, USA*, (1):908–913.

[9] "Omni-Bot" A six-legged omni-directional walking robot designed by A/P Frank Nickols, *http://www.ntu.edu.sg/home/mfnickols/home.htm*

[10] K.H. Low, and T.W. Tee. 2004. *Trajectory planning and implementational of four-legged walking machine*, *IFToMM2004, Tianjin*, Page: 1547 - 1551.

[11] Paolo Fiorini, Samad Hayati, Matt Heverly, Jeff Gensler. 1999. A Hopping Robot for Planetary Exploration. Alternative Education Resource Organization (AERO) Conference 99.

[12] Biologically-Inspired Fast Running Robots, 2004. *http://www.mechatronics.mech.tohoku.ac.jp/research/Kenken/kenken_en.htm*

[13] Iida, F., Dravid, R., and Paul, C. 2002. Design and control of a pendulum driven hopping robot, *Proc. IEEE/RSJ International Conference on Intelligent Robots and System*, (3):2141–2146.

[14] Fiorini, P., Hayati, S., Heverly, M., and Gensler, J. 1999. A hopping robot for planetary exploration, *Proc. IEEE Aerospace Conference* (2):153–158.

[15] GMD-snake. 2003. Robot-Snake with Flexible Real-Time Control. *http://ais.gmd.de/BAR/snake.html*

[16] Atacama Desert Trek, *http://www.ri.cmu.edu/projects/project_153.html*

[17] Octopus Robot. 2002. An Autonomous Wheeled Climbing Robot with Tactile Wheels, http://asl.epfl.ch/research/systems/Octopus/octopus.php

[18] Moore, K.L. and Flann, N.S. 2000 A six-wheeled omnidirectional autonomous mobile robot, *IEEE Control Systems Magazine*, (20-6):53–66.

[19] E. Rollins, J. Luntz, A. Foessel, B. Shamah, and W.L. 1998. Nomad: A Demonstration of the Transforming Chassis Whittaker, *In Proceedings of the Intelligent Components for Vehicles*, March, 1998.

[20] NASA JPL Mars Rover: Rocker 8. 2003. http://mars.jpl.nasa.gov/mer/mission/spacecraft_surface_rover.html

[21] Roland Siegwart, Pierre Lamon, Thomas Estier, Michel Lauria and Ralph Piguet. 2002. Innovative design for wheeled locomotion in rough terrain, *Robotics and Autonomous Systems*, Volume 40, Issues 2-3, 31 August 2002, 151–162.

[22] Takashi Kubota, Yoji Kuroda, Yasuharu Kunii and Ichiro Nakatani. 2003. Small, light-weight rover "Micro5" for lunar exploration, *Acta Astronautica*, Volume 52, Issues 2-6, January-March 2003, 447–453.

[23] Muir, P.F. and Neuman, C.P. 1987. Kinematic modeling of wheeled mobile robots, *J. Robotic Systems*, 4 (2):281–340.

[24] Muir, P.F. 1988. *Modeling and Control of Wheeled Mobile Robots*, Ph.D Thesis, Carnegie Mellon University, Pittsburgh, Pennsylvania.

[25] Dong Sung Kim, Hyun Chul Lee, and Wook Hyun Kwon. 2000. Geometric kinematics modeling of omni-directional autonomous mobile robot and its applications, *Proc. IEEE Int Conf on Robotics and Automation*, 2033–2038, San Francisco, Califonia.

[26] Wada, M.and Mori, S. 1996. Holonomic and omnidirectional vehicle with conventional tires Wada omnidirectional vehicles, *Proc. IEEE Int Conf on Robotics and Automation, Minneapolis, MN*, (4):3671–3676.

[27] Wada, M., and Mori, S. 1996. Modeling and control of a new type of omnidirectional holonomic vehicle, *Proc. IEEE Int Workshop on Advanced Motion Control, AMC, Piscataway. NJ*, (1):265–270.

[28] NomadXR4000. Omni-directional Robot by Nomadic Technologies, Inc. *http://www.robots.com*

[29] Byung-Ju Yi, and Whee Kuk Kim. 2002. The Kinematics for Redundantly Actuated Omnidirectional Mobile Robots, *Journal of Robotic Systems*, 19(6), 255–267.

[30] Campion, G., Bastin, G. and D'Andréa-Novel, B. 1993. Structural properties and classification of kinematic and dynamic models of wheeled mobile robots, *Proc. IEEE Int Conf on Robotics and Automation*, 462–469, Atlanta, Georgia.

[31] Killough, S.M. and Pin, F.G. 1992. Design of an omni-directional and holonomic wheeled platform prototype, *Proc. IEEE Int Conf on Robotics and Automation*, 84–90, Nice, France.

[32] Ilon, B. E. 1972. *Wheels for a course stable selfpropelling vehicle movable in any desired direction on the ground or some other base.* US Patents and Trademark Office, Patent 3,876,255.

[33] Fisette, P., Ferrière, L., Raucent, B. and Vaneghem, B. 2000. A multibody approach for modelling universal wheels of mobile robots, *Mechanism and Machine Theory*, (35), 329–351.

[34] Leow, Y. P. 2003. Kinematic Modelling, Mobility Analysis and Design of Wheeled Mobile Robots, *Master Thesis*, School of Mechanical and Production Engineering, Nanyang Technological University, Singapore.

[35] Y.P. Leow, K.H. Low and W.K. Loh. 2002. Kinematic Modelling and Analysis of Mobile Robots with Omni-Directional Wheels, *Proc. Seventh International Conference on Control, Automation, Robotics and Vision*, 2-5 Dec, Singapore.

[36] W.K. Loh, K.H. Low and Y.P. Leow. 2003. Mechatronics Design and Kinematic Modelling of a Singularityless Omni-Directional Wheeled Mo-

bile Robot, *Accepted for presentation at the IEEE International Conference on Robotics and Automation 2003*, 14 to 19 Sep, Taipei, Taiwan.

[37] Muir, P.F. and Neuman, C.P. 1987. Kinematic modeling for feedback control of an omnidirectional wheeled mobile robot, *Proc. IEEE Int Conf on Robotics and Automation, Raleigh, North Carolina, USA*, (4):1772–1778.

[38] Houshangi, N., and Lippitt, T. 1999. Omnibot mobile base for hazardous environment, *Proc. IEEE Canadian Conference on Electrical and Computer Engineering, Alberta, Canada*, (3), 1357–1361.

[39] Palm Pilot Robot Kit (PPRK). The Omni-directional Wheeled Mobile Robot by Carnegie Mellon Robotics Insitute, *http://www-2.cs.cmu.edu/ reshko/PILOT*

[40] ODV. 2001. The omni-directional vehicle by U.S. Navy, *http://www.robotics.com/robomenu/odv.html*

[41] ATX-Series Sidewinder Omni-directional Forklift by Airtrax Inc. 2002. *http://www.airtrax.com/home.htm*

[42] West, M., and Asada, H. 1995. Design and control of ball wheel omnidirectional vehicles, *Proc. IEEE Int Conf on Robotics and Automation, Nagoya, Japan*, (2):1931–1938.

[43] Wada, M., and Asada, H., 2000. Design and Control of a Variable Footprint Mechanism for Holonomic Omnidirectional Vehicles and Its Application to Wheelchair, *Proc. IEEE Trans.Rob. Autom.*, 16, (1):1–9.

[44] Holonomic Wheelchair by Houzumi Gear Co., Ltd. *http://www.homco.co.jp/HomePage/HOMEPAGE(E)/mainpage/mainpageE.htm*

[45] Jorge Angeles, Svetlana Ostrovskaya, and Alessio Salerno. 2002. The Development of Quasiholonomic Wheeled Robots, *Proc.IEEE Int Conf on Robotics and Automation, Washington D.C., USA*, (4):3514–3520.

[46] Wada, M.and Asada, H. H. 1998. A holonomic omnidirectional vehicle with a reconfigurable footprint mechanism and its application to wheelchairs, *Proc. IEEE Int Conf on Robotics and Automation, Leuven, Belgium*, (1):774–780.

[47] Chugo, D.; Kawabata, K.; Kaetsu, H.; Asama, H.; and Mishima, T. 2003. Development of omnidirectional vehicle with step-climbing ability, *Proc. IEEE Int Conf on Robotics and Automation*, 3849–3854, China Taipei, Taiwan.

[48] Angeles, J. 2002. *Fundamentals of Robotic Mechanical Systems: Theory, Methods, and Algorithms*, Second Edition, New York: Springer-Verlag.

[49] Ostrovskaya, S. 2001. *Dyanamics of Quasiholonomic and Nonholonomic Reconfigurable Rolling Robots*, Ph.D Thesis, McGill University, Montreal, Canada.

[50] Low K H, 2003. Mechanics of Mechanisms: Basic and Systematic Approaches, P rentice Hall, Singapore, 271 pages.

[51] 3D Simulation software.
http://www.mscsoftware.com

[52] 2D Simulation software/
http://www.interactivephysics.com

[53] Dimitrios S. Apostolopoulos. 2001. Analytical Configuration of Wheeled Robotic Locomotion. Ph.D Thesis, The Robotics Institute Carnegie Mellon University, Pittsburgh, Pennsylvania.

[54] HyperPhysics. Friction and Automobile Tires.
http://hyperphysics.phy-astr.gsu.edu/hbase/mechanics/frictire.html#c1

[55] Kyung-Seok Byun, Sung-Jae Kim, and Jae-Bok Song. 2001. Design of continuous alternate wheels for omnidirectional mobile robots, *Proc. of the IEEE Int Conf on Robotics and Automation*, (1)767–772.

[56] Catalogue. 2000. Interroll conveyor.
http://www.interoll.com

[57] General Information on Polyurethanes. 2003.
http://www.sunray-inc.com/techdata.html

[58] Williams, R.L., II; Carter, B.E.; Gallina, P.; Rosati, G. 2002. Dynamic model with slip for wheeled omnidirectional robots, *Proc. IEEE Int Conf on Robotics and Automation*, 18(3): 285–293.

[59] Loh, W. K. 2002. Development of an Omni-dircetional Wheeled Mobile Robot, *Final Year Project Report*, School of Mechanical and Production Engineering, Nanyang Technological University, Singapore.

[60] Lego. 2003.
http://www.lego.com/dacta

[61] Handyboard. 68HC11-based microcontroller system. 2003.
http://www.handyboard.com

[62] Specification Sheet. Maxon Motor. 2003.
http://www.maxonmotor.sg

[63] BASIC Stamp microcontroller
http://http://www.parallax.com

[64] Information about CompactFlash
http://www.compactflash.org/info/cfinfo.htm

[65] LV Intel Pentium III , PC/104-Plus CPU Module. 2004.
http://www.advantech/products

[66] J R Kerr. 2003. Motion Control Specialists.
http://www.jrkerr.com

[67] J R Kerr. 2003.
Documentation and Software. *http://www.jrkerr.com/docs.html/datasheets*

[68] Choosing a Battery that Will Last. 2003.
http://www.powerpulse.net/powerpulse/archive/aa_040201b1.stm

[69] Specification Sheet. 2003. SAFT lithium ion rechargeable battery.
http://www.saftbatteries.com

[70] Specification Sheet. 2003. Densei-lambda single output DC-DC Converter.
http://www.densei-lambda.com/products/sps/ps_onboard/pp/indexe.html

[71] Microcontroller. 2004. *http://www.parallax.com/*

[72] Katsuhiko Ogata. 1997. *Modern Control Engineering, 3rd edition*, Prentice-Hall International (UK) Limited, London.

H.R. Everett. 1995. *Sensors for Mobile Robots: Theory and Application*, Natick, Massachusetts. A K Peters.

[73] General Enginerring Material Properties. 2003.
http://www.cnc-precisionmachining.com/pdfs/general.pdf

Appendix A

Kinematics Analysis of Six Wheels ODRs

A. Kinematic Analysis of Six-wheel ODR

```
> restart: with(linalg): with(LinearAlgebra):
```

Platform Kinematics

```
> v[c](t):=<<diff(x(t),t), diff(y(t),t)>>;
```

$$v_c(t) := \begin{bmatrix} \frac{d}{dt}x(t) \\ \frac{d}{dt}y(t) \end{bmatrix}$$

lamda[n] is measured from positive i-direction(rover coordinate) and positive in anti-clockwise direction.

alpha[n] is measured from positive e[n]-direction(wheel coordinate) and positive in anti-clockwise direction.

```
> lambda[1]:=45*Pi/180:  lambda[2]:=135*Pi/180: lambda[3]:=180*Pi/180:
                  lambda[4]:=225*Pi/180: lambda[5]:=315*Pi/180:
  lambda[6]:=0*Pi/180:
> alpha(1):=135*Pi/180: alpha(2):=45*Pi/180: alpha(3):=90*Pi/180:
> alpha(4):=135*Pi/180: alpha(5):=45*Pi/180: alpha(6):=90*Pi/180:
> E[1]:=<<cos(alpha(1)) | -sin(alpha(1))> , <sin(alpha(1)) |
  cos(alpha(1))>>;
> E[2]:=<<cos(alpha(2)) | -sin(alpha(2))> , <sin(alpha(2)) |
  cos(alpha(2))>>;
> E[3]:=<<1 | 0> , <0 | 1>>;
> E[4]:=<<cos(alpha(4)) | -sin(alpha(4))> , <sin(alpha(4)) |
  cos(alpha(4))>>;
> E[5]:=<<cos(alpha(5)) | -sin(alpha(5))> , <sin(alpha(5)) |
  cos(alpha(5))>>;
> E[6]:=E[3];
```

$$E_1 := \begin{bmatrix} -\frac{1}{2}\sqrt{2} & -\frac{1}{2}\sqrt{2} \\ \frac{1}{2}\sqrt{2} & -\frac{1}{2}\sqrt{2} \end{bmatrix}$$

$$E_2 := \begin{bmatrix} \frac{1}{2}\sqrt{2} & -\frac{1}{2}\sqrt{2} \\ \frac{1}{2}\sqrt{2} & \frac{1}{2}\sqrt{2} \end{bmatrix}$$

$$E_3 := \begin{bmatrix} 1 & 0 \\ 0 & 1 \end{bmatrix}$$

$$E_4 := \begin{bmatrix} -\frac{1}{2}\sqrt{2} & -\frac{1}{2}\sqrt{2} \\ \frac{1}{2}\sqrt{2} & -\frac{1}{2}\sqrt{2} \end{bmatrix}$$

$$E_5 := \begin{bmatrix} \frac{1}{2}\sqrt{2} & -\frac{1}{2}\sqrt{2} \\ \frac{1}{2}\sqrt{2} & \frac{1}{2}\sqrt{2} \end{bmatrix}$$

$$E_6 := \begin{bmatrix} 1 & 0 \\ 0 & 1 \end{bmatrix}$$

To find the vector g in world coordinate, vectors g transformed from roller coordinate -> wheel coordinate --> rover body coordinate.

```
> Tg[1]:=<<cos(alpha(1)+90*Pi/180)| sin(alpha(1)+90*Pi/180)>>;
> Tg[2]:=<<cos(alpha(2)+90*Pi/180)| sin(alpha(2)+90*Pi/180)>>;
> Tg[3]:=<<cos(alpha(3)+90*Pi/180)| sin(alpha(3)+90*Pi/180)>>;
> Tg[4]:=<<cos(alpha(4)-90*Pi/180)| sin(alpha(4)-90*Pi/180)>>;
> Tg[5]:=<<cos(alpha(5)-90*Pi/180)| sin(alpha(5)-90*Pi/180)>>;
> Tg[6]:=<<cos(alpha(6)-90*Pi/180)| sin(alpha(6)-90*Pi/180)>>;
```

$$Tg_1 := \begin{bmatrix} -\frac{1}{2}\sqrt{2} & -\frac{1}{2}\sqrt{2} \end{bmatrix}$$

$$Tg_2 := \begin{bmatrix} -\frac{1}{2}\sqrt{2} & \frac{1}{2}\sqrt{2} \end{bmatrix}$$

$$Tg_3 := [-1 \quad 0]$$

$$Tg_4 := \begin{bmatrix} \frac{1}{2}\sqrt{2} & \frac{1}{2}\sqrt{2} \end{bmatrix}$$

$$Tg_5 := \begin{bmatrix} \frac{1}{2}\sqrt{2} & -\frac{1}{2}\sqrt{2} \end{bmatrix}$$

$$Tg_6 := [1 \quad 0]$$

```
> d[1]:=<<r[1]*cos(lambda[1]), r[1]*sin(lambda[1])>>;
> d[2]:=<<r[2]*cos(lambda[2]), r[2]*sin(lambda[2])>>;
> d[3]:=<<r[3]*cos(lambda[3]), r[3]*sin(lambda[3])>>;
> d[4]:=<<r[4]*cos(lambda[4]), r[4]*sin(lambda[4])>>;
> d[5]:=<<r[5]*cos(lambda[5]), r[5]*sin(lambda[5])>>;
> d[6]:=<<r[6]*cos(lambda[6]), r[6]*sin(lambda[6])>>;
```

$$d_1 := \begin{bmatrix} \frac{1}{2} r_1 \sqrt{2} \\ \frac{1}{2} r_1 \sqrt{2} \end{bmatrix}$$

$$d_2 := \begin{bmatrix} -\frac{1}{2} r_2 \sqrt{2} \\ \frac{1}{2} r_2 \sqrt{2} \end{bmatrix}$$

$$d_3 := \begin{bmatrix} -r_3 \\ 0 \end{bmatrix}$$

$$d_4 := \begin{bmatrix} -\frac{1}{2} r_4 \sqrt{2} \\ -\frac{1}{2} r_4 \sqrt{2} \end{bmatrix}$$

$$d_5 := \begin{bmatrix} \frac{1}{2} r_5 \sqrt{2} \\ -\frac{1}{2} r_5 \sqrt{2} \end{bmatrix}$$

$$d_6 := \begin{bmatrix} r_6 \\ 0 \end{bmatrix}$$

```
> eqn1:=vp[1]=E[1].d[1] * diff(psi(t),t) + v[c](t):
> eqn2:=vp[2]=E[2].d[2] * diff(psi(t),t) + v[c](t):
> eqn3:=vp[3]=E[3].d[3] * diff(psi(t),t) + v[c](t):
> eqn4:=vp[4]=E[4].d[4] * diff(psi(t),t) + v[c](t):
> eqn5:=vp[5]=E[5].d[5] * diff(psi(t),t) + v[c](t):
> eqn6:=vp[6]=E[6].d[6] * diff(psi(t),t) + v[c](t):
```

Wheel Kinematics

r[w] refers to radii of wheel hubs;

r[r] refers to the radii of the rollers;

diff(theta(t),t) is the rates of kth wheel hub;

diff(phi(t),t) is the rates of kth active roller

```
> f1:=vw[1]=<<r[r] * diff(psi(t)[1],t) * p[1], -r[w] *
  diff(theta(t)[1],t) * f[1]>>:
> f2:=vw[2]=<<r[r] * diff(psi(t)[2],t) * p[2], -r[w] *
  diff(theta(t)[2],t) * f[2]>>:
```

```
> f3:=vw[3]=<<r[r] * diff(psi(t)[3],t) * p[3], -r[w] *
  diff(theta(t)[3],t) * f[3]>>:
> f4:=vw[4]=<<r[r] * diff(psi(t)[4],t) * p[4], -r[w] *
  diff(theta(t)[4],t) * f[4]>>:
> f5:=vw[5]=<<r[r] * diff(psi(t)[5],t) * p[5], -r[w] *
  diff(theta(t)[5],t) * f[5]>>:
> f6:=vw[6]=<<r[r] * diff(psi(t)[6],t) * p[6], -r[w] *
  diff(theta(t)[6],t) * f[6]>>:
```

Dot-multiply f1 to f6 with Transpose(g[n]) to eliminate un-controllable variable diff(psi(t)[n],t);

Note that Transpose(g[n])*f[n]=sin(alpha[n]); g[n].h[n]=0; so,

```
> f1N:=Tg[1].vp[1] = -r[w] * diff(theta(t)[1],t) * sin(alpha(1)):
                             f2N:=Tg[2].vp[2] = -r[w] *
  diff(theta(t)[2],t) * sin(alpha(2)):
    f3N:=Tg[3].vp[3] = -r[w] * diff(theta(t)[3],t) * sin(alpha(3)):
                             f4N:=Tg[4].vp[4] = -r[w] *
  diff(theta(t)[4],t) * sin(alpha(4)):
   f5N:=Tg[5].vp[5] = -r[w] * diff(theta(t)[5],t) * sin(alpha(5)):
                               f6N:=Tg[6].vp[6] = -r[w] *
  diff(theta(t)[6],t) * sin(alpha(6)):
```

Dot-multiply eqn1 to eqn6 with Tg[n], n=1..6

```
> eqn1N:=Tg[1].vp[1] = Tg[1].E[1].d[1]*diff(psi(t),t) + Tg[1].v[c](t):
> eqn2N:=Tg[2].vp[2] = Tg[2].E[2].d[2]*diff(psi(t),t) + Tg[2].v[c](t):
> eqn3N:=Tg[3].vp[3] = Tg[3].E[3].d[3]*diff(psi(t),t) + Tg[3].v[c](t):
> eqn4N:=Tg[4].vp[4] = Tg[4].E[4].d[4]*diff(psi(t),t) + Tg[4].v[c](t):
> eqn5N:=Tg[5].vp[5] = Tg[5].E[5].d[5]*diff(psi(t),t) + Tg[5].v[c](t):
> eqn6N:=Tg[6].vp[6] = Tg[6].E[6].d[6]*diff(psi(t),t) + Tg[6].v[c](t):
```

```
> K:=simplify(<<Tg[1].E[1].d[1] | Tg[1]> , <Tg[2].E[2].d[2] | Tg[2]> ,
  <Tg[3].E[3].d[3] | Tg[3]> , <Tg[4].E[4].d[4] | Tg[4]>,
  <Tg[5].E[5].d[5] | Tg[5]> , <Tg[6].E[6].d[6] | Tg[6]>>);
```

$$K := \begin{bmatrix} \frac{1}{2} r_1 \sqrt{2} & -\frac{1}{2}\sqrt{2} & -\frac{1}{2}\sqrt{2} \\ \frac{1}{2} r_2 \sqrt{2} & -\frac{1}{2}\sqrt{2} & \frac{1}{2}\sqrt{2} \\ r_3 & -1 & 0 \\ \frac{1}{2} r_4 \sqrt{2} & \frac{1}{2}\sqrt{2} & \frac{1}{2}\sqrt{2} \\ \frac{1}{2} r_5 \sqrt{2} & \frac{1}{2}\sqrt{2} & -\frac{1}{2}\sqrt{2} \\ r_6 & 1 & 0 \end{bmatrix}$$

```
> v[c](t):=<<diff(x(t),t), diff(y(t),t)>>:twist:=<<diff(psi(t),t),
  v[c](t)>>;
```

$$twist := \begin{bmatrix} \frac{d}{dt}\psi(t) \\ \frac{d}{dt}x(t) \\ \frac{d}{dt}y(t) \end{bmatrix}$$

```
> V:=Vector([-r[w]*sin(alpha(1)),-r[w]*sin(alpha(2)),-r[w]*sin(alpha(3))
  ,-r[w]*sin(alpha(4)),-r[w]*sin(alpha(5)),-r[w]*sin(alpha(6))]):
  J:=Matrix(1..6,1..6,V,shape=diagonal);
```

$$J := \begin{bmatrix} -\frac{1}{2}r_w\sqrt{2} & 0 & 0 & 0 & 0 & 0 \\ 0 & -\frac{1}{2}r_w\sqrt{2} & 0 & 0 & 0 & 0 \\ 0 & 0 & -r_w & 0 & 0 & 0 \\ 0 & 0 & 0 & -\frac{1}{2}r_w\sqrt{2} & 0 & 0 \\ 0 & 0 & 0 & 0 & -\frac{1}{2}r_w\sqrt{2} & 0 \\ 0 & 0 & 0 & 0 & 0 & -r_w \end{bmatrix}$$

```
> with(LinearAlgebra): Inverse_J:=(MatrixInverse(J));
```

$$Inverse\_J := \begin{bmatrix} -\frac{\sqrt{2}}{r_w} & 0 & 0 & 0 & 0 & 0 \\ 0 & -\frac{\sqrt{2}}{r_w} & 0 & 0 & 0 & 0 \\ 0 & 0 & -\frac{1}{r_w} & 0 & 0 & 0 \\ 0 & 0 & 0 & -\frac{\sqrt{2}}{r_w} & 0 & 0 \\ 0 & 0 & 0 & 0 & -\frac{\sqrt{2}}{r_w} & 0 \\ 0 & 0 & 0 & 0 & 0 & -\frac{1}{r_w} \end{bmatrix}$$

```
> Thetadot:=<<diff(theta[1](t),t), diff(theta[2](t),t),
  diff(theta[3](t),t), diff(theta[4](t),t),
  diff(theta[5](t),t),diff(theta[6](t),t)>>;
```

$$Thetadot := \begin{bmatrix} \frac{d}{dt}\theta_1(t) \\ \frac{d}{dt}\theta_2(t) \\ \frac{d}{dt}\theta_3(t) \\ \frac{d}{dt}\theta_4(t) \\ \frac{d}{dt}\theta_5(t) \\ \frac{d}{dt}\theta_6(t) \end{bmatrix}$$

```
> Thetadot=(Inverse_J.K).twist;
```

$$\begin{bmatrix} \frac{d}{dt}\theta_1(t) \\ \frac{d}{dt}\theta_2(t) \\ \frac{d}{dt}\theta_3(t) \\ \frac{d}{dt}\theta_4(t) \\ \frac{d}{dt}\theta_5(t) \\ \frac{d}{dt}\theta_6(t) \end{bmatrix} = \begin{bmatrix} -\frac{r_1\left(\frac{d}{dt}\psi(t)\right)}{r_w} + \frac{\frac{d}{dt}x(t)}{r_w} + \frac{\frac{d}{dt}y(t)}{r_w} \\ -\frac{r_2\left(\frac{d}{dt}\psi(t)\right)}{r_w} + \frac{\frac{d}{dt}x(t)}{r_w} - \frac{\frac{d}{dt}y(t)}{r_w} \\ -\frac{r_3\left(\frac{d}{dt}\psi(t)\right)}{r_w} + \frac{\frac{d}{dt}x(t)}{r_w} \\ -\frac{r_4\left(\frac{d}{dt}\psi(t)\right)}{r_w} - \frac{\frac{d}{dt}x(t)}{r_w} - \frac{\frac{d}{dt}y(t)}{r_w} \\ -\frac{r_5\left(\frac{d}{dt}\psi(t)\right)}{r_w} - \frac{\frac{d}{dt}x(t)}{r_w} + \frac{\frac{d}{dt}y(t)}{r_w} \\ -\frac{r_6\left(\frac{d}{dt}\psi(t)\right)}{r_w} - \frac{\frac{d}{dt}x(t)}{r_w} \end{bmatrix}$$

Appendix B

3D Picture and Global CoG Calculations

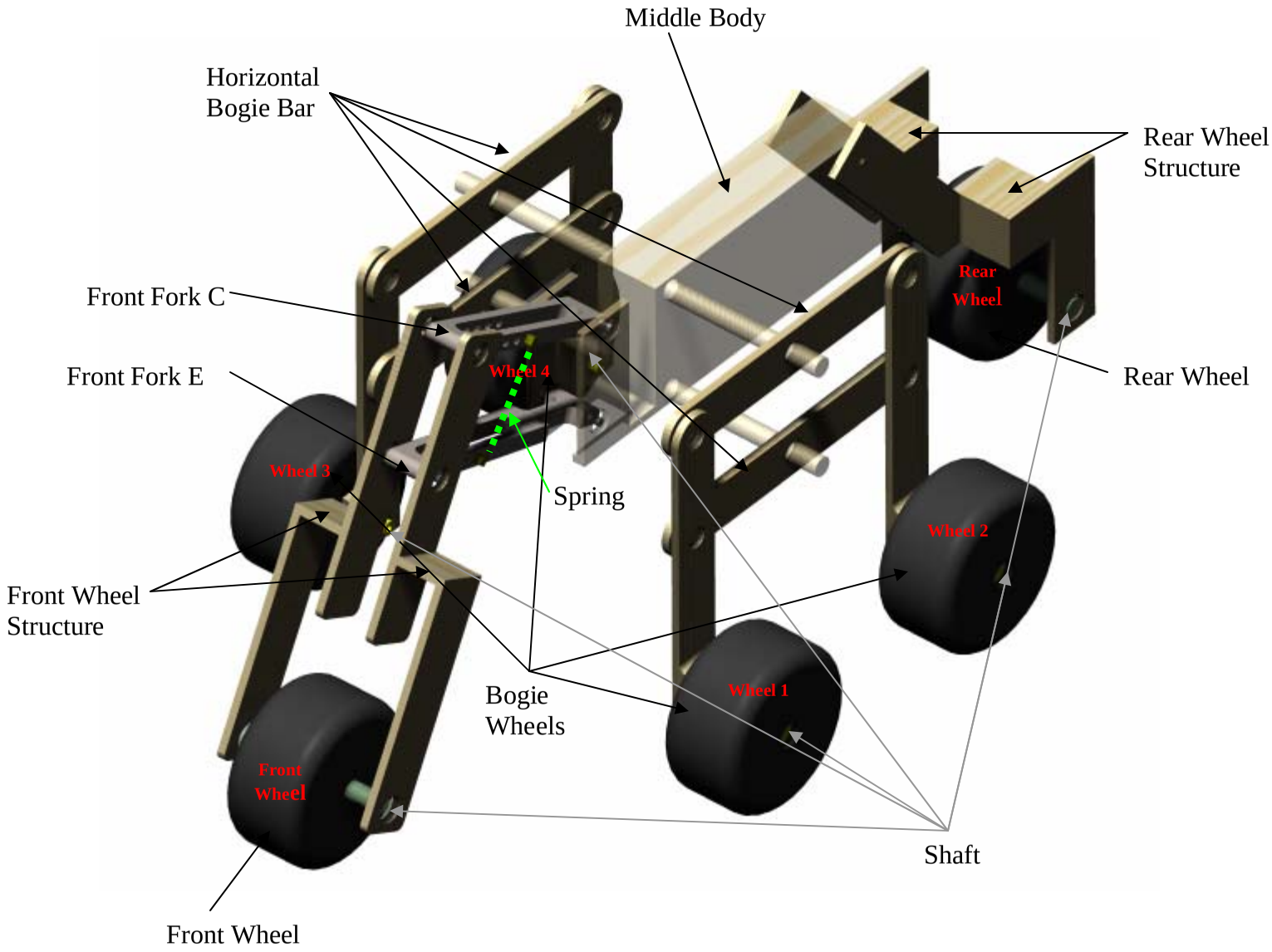

Appendix B

Ground Level																												
Items	Fr Fork C2	Fr Fork E2	Fr Wh shaft	Fr wh struc 1	Fr wh struc 2	Fr Wheel	Hori Bar 1	Hori Bar 2	Hori Bar 3	Hori Bar 4	Mid Bod	Re Wh shaft	Re Wh struc 1	Re Wh struc 2	Re Wheel	shaft 1	shaft 2	shaft 3	shaft 4	Vert Bar 1	Vert Bar 2	Vert Bar 3	Vert Bar 4	Wheels 1	Wheels 2	Wheels 3	Wheels 4
X coors (m)	0.01104	0.01104	-0.04196	0.01804	-0.02196	0.01854	0.108	0.108	-0.107	-0.107	-0.00196	-0.04109	0.01792	-0.0221	0.01841	0.175	0.175	-0.179	-0.179	-0.119	-0.119	0.115	0.115	0.1298	0.1301	-0.175	-0.175
Y coors (m)	-0.5119	-0.4751	-0.5863	-0.4768	-0.4468	-0.5863	-0.4234	-0.4223	-0.4234	-0.4223	-0.3906	-0.06444	-0.1842	-0.155	-0.06429	-0.4056	-0.2276	-0.4056	-0.2276	-0.3936	-0.2156	-0.4236	-0.2456	-0.406	-0.2277	-0.4056	-0.2274
Z coors (m)	0.004618	0.06841	-0.152	0.08882	0.07279	-0.152	0.004185	-0.06381	0.004234	-0.06376	-0.05899	-0.1518	0.01548	0.03292	-0.1518	-0.1518	-0.1518	-0.1518	-0.1518	0.03447	0.03437	0.03394	0.03393	-0.1519	-0.1518	-0.1518	-0.1518
angle x	1.242	1.11	1.9	-2.062	1.08	-1.241	1.571	1.571	1.57	1.57	1.587	-1.029	-1.032	2.11	2.116	1.965	1.965	1.965	1.965	1.587	1.587	-1.555	-1.555	-1.167	-1.174	1.965	1.965
angle y	1.571	1.571	1.571	0	0	-1.571	1.571	1.571	1.571	1.571	1.571	1.57	-0.0005374	0.0005374	-1.563	-1.571	-1.571	1.571	1.571	0	0	0	0	1.571	1.571	1.571	1.571
angle z	0	0	0	0	3.142	0	0	0	0	0	0	2.994	-1.13E-06	-3.142	-2.997	0	0	0	0	-1.571	-1.571	1.571	1.571	0	0	0	0
Step Level																											
X coors (m)	0.01098	0.01093	-0.04194	0.01793	-0.02213	0.01856	0.1078	0.1077	-0.1072	-0.1073	-0.0023	-0.04193	0.01742	-0.02261	0.01756	0.1746	0.1744	-0.1794	-0.1796	-0.1192	-0.1194	0.1149	0.1146	0.1294	0.1294	-0.1754	-0.1756
Y coors (m)	-0.6246	-0.5597	-0.7706	-0.5546	-0.5368	-0.7706	-0.6314	-0.6303	-0.6317	-0.6306	-0.5988	-0.2725	-0.3924	-0.3633	-0.2724	-0.6136	-0.4356	-0.614	-0.436	-0.602	-0.424	-0.6317	-0.4537	-0.6138	-0.4357	-0.614	-0.4359
Z coors (m)	0.09887	0.1362	-0.002619	0.1501	0.1212	-0.00269	0.003948	-0.06404	0.004429	-0.06356	-0.05893	-0.1516	0.01556	0.03305	-0.1518	-0.1521	-0.1518	-0.1515	-0.1516	0.03468	0.03459	0.03371	0.034	-0.1517	-0.1516	-0.1515	-0.1517
angle x	-2.236	-2.293	-2.253	-2.59	0.5515	0.8882	-2.362	-2.362	-2.363	-2.363	-2.363	-2.382	-1.032	2.11	0.5111	0.7481	0.7491	-2.366	-2.366	1.587	1.587	-1.554	-1.554	-2.394	-2.393	-2.366	-2.366
angle y	1.569	1.569	1.569	-0.001726	0.001655	-1.569	1.569	1.569	1.569	1.569	1.569	1.569	-0.0009456	0.0009456	-1.562	-1.569	-1.569	1.569	1.569	0.001188	0.001188	-0.00119	-0.00119	1.569	1.569	1.569	1.569
angle z	2.485	2.099	0.6199	-0.0005985	-3.141	-0.6199	-2.349	-2.349	-2.35	-2.35	-2.333	2.686	0.001669	3.14	-2.942	0.1432	-0.0534	2.843	2.973	-1.572	-1.572	1.572	1.572	-0.1335	0.05641	2.843	2.973
C.G																											
X coors (m)	0.07549	0.06307	0	0.01216	0.01216	0	0.104	0.104	0.104	0.104	0.09	0	0.01668	0.01668	0	0	0	0	0	0.1177	0.1177	0.1177	0.1177	0	0	0	0
Y coors (m)	0.005	0.005	0	0.1408	0.1408	0	0.015	0.015	0.015	0.015	-0.01	0	0.1102	0.1102	0	0	0	0	0	0.000844	0.000844	0.000844	0.000844	0	0	0	0
Z coors (m)	-0.013	-0.013	0.03841	0.017	0.017	0.0205	-0.0025	-0.0025	-0.0025	-0.0025	0	0.03841	0.017	0.017	0.0205	0.02764	0.02764	0.02764	0.02764	0.015	0.015	0.015	0.015	0.0205	0.0205	0.0205	0.0205

Mass W (kg)	0.05	0.05	0.09	0.06	0.06	0.2	0.05	0.05	0.05	0.05	2.4	0.09	0.135	0.135	0.2	0.0847	0.0847	0.0847	0.0847	0.05	0.05	0.05	0.05	0.2	0.2	0.2	0.2
World Position																											
Ground Level																											
x bar	-0.000197538	-0.0019728	-0.00355	0.0302	-0.03406264	-0.00196	0.105479	0.105479	-0.10952	-0.10952	-0.00198	-0.00266001	0.034590987	-0.03881575	-0.0020894	0.14736	0.14736	-0.15136	-0.1514	-0.11818	-0.11818	0.114132	0.114132	0.1503	0.1506	-0.1545	-0.1545
y bar	-0.43884186	-0.4163873	-0.5862926	-0.52822359	-0.52815865	-0.5863	-0.3194	-0.3183	-0.31939	-0.31829	-0.30045	-0.06441379	-0.113056786	-0.113016707	-0.0644267	-0.40559	-0.2276	-0.40559	-0.2276	-0.40669	-0.22869	-0.40674	-0.22874	-0.406	-0.2277	-0.4056	-0.2274
z bar	-0.01502501	0.04484487	-0.1519975	-0.04335131	-0.04338144	-0.152	0.019206	-0.04879	0.019151	-0.04884	-0.06753	-0.15178423	-0.070380257	-0.070372058	-0.1518829	-0.1518	-0.1518	-0.1518	-0.1518	-0.08346	-0.08356	-0.08351	-0.08352	-0.1519	-0.1518	-0.1518	-0.1518
Step Level																											
x bar	-0.00213287	-0.0021348	-0.0035301	0.030144906	-0.0341784	-0.00194	0.105188	0.105088	-0.10981	-0.10991	-0.00243	-0.00352006	0.03389997	-0.039449406	-0.0029392	0.14696	0.14676	-0.15176	-0.152	-0.11848	-0.11868	0.113896	0.113596	0.1499	0.1499	-0.1549	-0.1551
y bar	-0.62959979	-0.5791865	-0.8018633	-0.67445978	-0.6566901	-0.75391	-0.65582	-0.65472	-0.65616	-0.65506	-0.61906	-0.23800786	-0.335834733	-0.306723272	-0.2924922	-0.58624	-0.408	-0.58758	-0.4088	-0.602	-0.424	-0.6317	-0.4537	-0.63412	-0.45617	-0.59441	-0.41569
z bar	0.026954812	0.07336468	-0.0026625	0.061821659	0.06191848	-0.00267	0.019096	-0.04889	0.019369	-0.04862	-0.06745	-0.15165003	-0.070320634	-0.070228546	-0.1516427	-0.15206	-0.1518	-0.15154	-0.1516	-0.08325	-0.08334	-0.08372	-0.08343	-0.15173	-0.15163	-0.15153	-0.15178

Ground Level																											
x bar times W	-9.8769E-05	-9.864E-05	-0.0003195	0.001812	-0.00204376	-0.00039	0.005274	0.005274	-0.00548	-0.00548	-0.00476	-0.0002412	0.004669783	-0.005240126	-0.0004179	0.012481	0.01248	-0.01282	-0.0128	-0.00591	-0.00591	0.005707	0.005707	0.03006	0.03012	-0.0309	-0.0309
y bar times W	-0.02194209	-0.0208194	-0.0527663	-0.03169342	-0.03168952	-0.11726	-0.01597	-0.01592	-0.01597	-0.01591	-0.72108	-0.00579724	-0.015262666	-0.015257255	-0.0128853	-0.03435	-0.0193	-0.03435	-0.0193	-0.02033	-0.01143	-0.02034	-0.01144	-0.0812	-0.04554	-0.08112	-0.04548
z bar times W	-0.00075125	0.00224224	-0.0136798	-0.00260108	-0.00260289	-0.0304	0.00096	-0.00244	0.000958	-0.00244	-0.16207	-0.01366058	-0.009501335	-0.009500228	-0.0303766	-0.01286	-0.0129	-0.01286	-0.0129	-0.00417	-0.00418	-0.00418	-0.00418	-0.03038	-0.03036	-0.03036	-0.03036
Step Level																											
x bar times W	-0.00010664	-0.0001067	-0.0003177	0.001808694	-0.0020507	-0.00039	0.005259	0.005254	-0.00549	-0.0055	-0.00582	-0.00031681	0.004576496	-0.00532567	-0.0005878	0.012448	0.01243	-0.01285	-0.0129	-0.00592	-0.00593	0.005695	0.00568	0.02998	0.02998	-0.03098	-0.03102
y bar times W	-0.03147999	-0.0289593	-0.0721677	-0.04046759	-0.03940141	-0.15078	-0.03279	-0.03274	-0.03281	-0.03275	-1.48575	-0.02142071	-0.045337689	-0.041407642	-0.0584984	-0.04965	-0.0346	-0.04977	-0.0346	-0.0301	-0.0212	-0.03159	-0.02269	-0.12682	-0.09123	-0.11888	-0.08314
z bar times W	0.001347741	0.00366823	-0.0002396	0.0037093	0.003715109	-0.00053	0.000955	-0.00244	0.000968	-0.00243	-0.16189	-0.0136485	-0.009493286	-0.009480854	-0.0303285	-0.01288	-0.0129	-0.01284	-0.0128	-0.00416	-0.00417	-0.00419	-0.00417	-0.03035	-0.03033	-0.03031	-0.03035

	Ground Level	Step Level
∑x bar times W	-0.01023431	-0.0124816
∑y bar times W	-1.5343684	-2.8410117
∑z bar times W	-0.46545967	-0.4055467

Centre of Mass	Ground Level	Step Level
X BAR	-0.00204327	-0.0024919
Y BAR	-0.30633453	-0.5672041
Z BAR	-0.09292838	-0.0809668

Appendix C

Analytical Synthesis Results

C. Analytical Systhesis of Front Fork.

```
> restart;
```

Input all pivot coordinates, and links rotation angles.

```
> x[01]:=s0; x[02]:=s0+0.01; x[03]:=s0+0.01; y[0]:=0.12;
> x[5]:=s0+0.194; y[51]:=0.05; y[52]:=0.125; y[53]:=0.2; y[2]:=y0+0.058;
```

$$x_1 := s0$$

$$x_2 := s0 + 0.01$$

$$x_3 := s0 + 0.01$$

$$y_0 := 0.12$$

$$x_5 := s0 + 0.194$$

$$y_{51} := 0.05$$

$$y_{52} := 0.125$$

$$y_{53} := 0.2$$

$$y_2 := y0 + 0.058$$

```
> phi[21]:=28; phi[22]:=65; phi[23]:=100;  #input angle
> phi[31]:=111; phi[32]:=123; phi[33]:=145;  #input angle
> phi[41]:=20; phi[42]:=51; phi[43]:=75;  #input angle
```

$$\phi_{21} := 28$$

$$\phi_{22} := 65$$

$$\phi_{23} := 100$$

$$\phi_{31} := 111$$

$$\phi_{32} := 123$$

$$\phi_{33} := 145$$

$$\phi_{41} := 20$$

$$\phi_{42} := 51$$

$$\phi_{43} := 75$$

```
> alpha[3]:=(phi[33]-phi[31])*3.14159/180;
  alpha[2]:=(phi[32]-phi[31])*3.14159/180;
```

$$\alpha_3 := 0.593411444$$

$$\alpha_2 := 0.209439333$$

```
> beta[3]:=(phi[23]-phi[21])*3.14159/180;
  beta[2]:=(phi[22]-phi[21])*3.14159/180;
```

$$\beta_3 := 1.256636000$$

$$\beta_2 := 0.6457712782$$

```
> theta[3]:=(phi[43]-phi[41])*3.14159/180;
  theta[2]:=(phi[42]-phi[41])*3.14159/180;
```

$$\theta_3 := 0.9599302784$$

$$\theta_2 := 0.5410516112$$

```
> R[1]:=x[51]-x[01]+I*y[51];
```

$$R_1 := x_{51} - s0 + 0.05\,I$$

```
> R[2]:=x[51]-x[02]+I*y[52];
```

$$R_2 := x_{51} - s0 + (-0.01 + 0.125\,I)$$

```
> R[3]:=x[51]-x[03]+I*y[53];
```

$$R_3 := x_{51} - s0 + (-0.01 + 0.2\,I)$$

```
> delta[2]:=R[2]-R[1];
```

$$\delta_2 := -0.01 + 0.075\,I$$

```
> delta[3]:=R[3]-R[1];
```

$$\delta_3 := -0.01 + 0.15\,I$$

Left hand Dyad (LHD)

```
> a:=delta[2]*(exp(I*alpha[3])-1)-delta[3]*(exp(I*alpha[2])-1);
```

$$a := -0.00926161110 - 0.01305711636\,I$$

```
> b:=(exp(I*beta[2])-1)*((exp(I*alpha[3])-1))-(exp(I*alpha[2])-1)*(exp(I
  *beta[3])-1);
```

$$b := -0.1194686008 - 0.0510429007\,I$$

```
> AD_LHD:=a/b;
```

$$AD\_LHD := 0.1050439482 + 0.06441331440\,I$$

```
>
> pa:=x[01]+y[2]*I;
```

$$pa := s0 + I\,(y0 + 0.058)$$

```
> p2:=pa+AD_LHD;
```

$$p2 := s0 + I\,(y0 + 0.058) + (0.1050439482 + 0.06441331440\,I)$$

```
>
> c:=(exp(I*beta[2])-1)*delta[3]-delta[2]*(exp(I*beta[3])-1);
```

$$c := -0.02383915241 + 0.02511144143\,I$$

```
> d:=(exp(I*alpha[3])-1)*(exp(I*beta[2])-1)-(exp(I*alpha[2])-1)*(exp(I*b
  eta[3])-1);
```

$$d := -0.1194686008 - 0.0510429007\,I$$

```
> DC_LHD:=c/d;
```

$$DC\_LHD := 0.09279878170 - 0.2498410480\,I$$

```
> p3:=p2+DC_LHD;
```

$$p3 := s0 + I\,(y0 + 0.058) + (0.1978427299 - 0.1854277336\,I)$$

Right hand Dyad (RHD)

```
> a1:=delta[2]*(exp(I*alpha[3])-1)-delta[3]*(exp(I*alpha[2])-1);
```

$$a1 := -0.00926161110 - 0.01305711636\, I$$

```
> b1:=(exp(I*theta[2])-1)*((exp(I*alpha[3])-1))-(exp(I*alpha[2])-1)*(exp
  (I*theta[3])-1);
```

$$b1 := -0.1025935584 - 0.0613641595\, I$$

```
> AD_RHD:=a1/b1;
```

$$AD\_RHD := 0.1225541123 + 0.05396719201\, I$$

```
>
```

```
> c1:=(exp(I*theta[2])-1)*delta[3]-delta[2]*(exp(I*theta[3])-1);
```

$$c1 := -0.01865518839 + 0.01359798687\, I$$

```
> d1:=(exp(I*alpha[3])-1)*(exp(I*theta[2])-1)-(exp(I*alpha[2])-1)*(exp(I
  *theta[3])-1);
```

$$d1 := -0.1025935584 - 0.0613641595\, I$$

```
> DC_RHD:=c1/d1;
```

$$DC\_RHD := 0.07553517970 - 0.1777220711\, I$$

```
> p4:=DC_RHD+y[0]*I+AD_RHD;
```

$$p4 := 0.1980892920 - 0.00375487909\, I$$

Synthesis Results

```
> r2:=sqrt(Re(AD_LHD)^2+Im(AD_LHD)^2);
```

$$r2 := 0.1232205588$$

```
> r3:=sqrt(Re(DC_LHD)^2+Im(DC_LHD)^2);
```

$$r3 := 0.2665185982$$

```
> r4:=sqrt(Re(AD_RHD)^2+Im(AD_RHD)^2);
```

$$r4 := 0.1339102993$$

```
> r3b:=sqrt(Re(DC_RHD)^2+Im(DC_RHD)^2);
```

$$r3b := 0.1931079955$$

```
> r3u:=r3-r3b;
```

$$r3u := 0.0734106027$$